

Nanomechanical Resonators Based on Quasi-two-dimensional Materials

DISSERTATION

Zur Erlangung des akademischen Grades eines
Doktor-Ingenieur
an der Fakultät Bauingenieurwesen
der Bauhaus-Universität Weimar

vorgelegt von

M.Eng. Cuixia Wang
Geboren am 10. Dezember 1987 in China

Mentor: Prof. Dr.-Ing. Timon Rabczuk
Gutachter: Prof. Dr.-Ing. habil. Carsten Könke
Prof. Dr.-Ing. Pedro Areias

Tag der Disputation: 21 June 2018

Abstract

Advances in nanotechnology lead to the development of nano-electro-mechanical systems (NEMS) such as nanomechanical resonators with ultra-high resonant frequencies. The ultra-high-frequency resonators have recently received significant attention for wide-ranging applications such as molecular separation, molecular transportation, ultra-high sensitive sensing, high-frequency signal processing, and biological imaging. It is well known that for micrometer length scale, first-principles technique, the most accurate approach, poses serious limitations for comparisons with experimental studies. For such larger size, classical molecular dynamics (MD) simulations are desirable, which require interatomic potentials. Additionally, a mesoscale method such as the coarse-grained (CG) method is another useful method to support simulations for even larger system sizes. Furthermore, quasi-two-dimensional (Q2D) materials have attracted intensive research interest due to their many novel properties over the past decades. However, the energy dissipation mechanisms of nanomechanical resonators based on several Q2D materials are still unknown.

In this work, the addressed main issues include the development of the CG models for molybdenum disulphide (MoS_2), investigation of the mechanism effects on black phosphorus (BP) nanoresonators and the application of graphene nanoresonators. The primary coverage and results of the dissertation are as follows:

Method development. Firstly, a two-dimensional (2D) CG model for single layer MoS_2 (SL MoS_2) is analytically developed. The Stillinger-Weber (SW) potential for this 2D CG model is further parametrized, in which all SW geometrical parameters are determined analytically according to the equilibrium condition for each individual potential term, while the SW energy parameters are derived analytically based on the valence force field model. Next, the 2D CG model is further simplified to one-dimensional (1D) CG model, which describes the 2D SL MoS_2 structure using a 1D chain model. This 1D CG model is applied to investigate the relaxed configuration and the resonant oscillation of the folded SL MoS_2 . Owing to the simplicity nature of the 1D CG model, the relaxed configuration of the folded SL MoS_2 is determined analytically, and the resonant oscillation frequency is derived analytically. Considering the increasing interest

in studying the properties of other 2D layered materials, and in particular those in the semiconducting transition metal dichalcogenide class like MoS₂, the CG models proposed in current work provide valuable simulation approaches.

Mechanism understanding. Two energy dissipation mechanisms of BP nanoresonators are focused exclusively, i.e. mechanical strain effects and defect effects (including vacancy and oxidation). Vacancy defect is intrinsic damping factor for the quality (Q)-factor, while mechanical strain and oxidation are extrinsic damping factors. Intrinsic dissipation (induced by thermal vibrations) in BP resonators (BPRs) is firstly investigated. Specifically, classical MD simulations are performed to examine the temperature dependence for the Q-factor of the single layer BPR (SLBPR) along the armchair and zigzag directions, where two-step fitting procedure is used to extract the frequency and Q-factor from the kinetic energy time history. The Q-factors of BPRs are evaluated through comparison with those of graphene and MoS₂ nanoresonators. Next, effects of mechanical strain, vacancy and oxidation on BP nanoresonators are investigated in turn. Considering the increasing interest in studying the properties of BP, and in particular the lack of theoretical study for the BPRs, the results in current work provide a useful reference.

Application. A novel application for graphene nanoresonators, using them to self-assemble small nanostructures such as water chains, is proposed. All of the underlying physics enabling this phenomenon is elucidated. In particular, by drawing inspiration from macroscale self-assembly using the higher order resonant modes of Chladni plates, classical MD simulations are used to investigate the self-assembly of water molecules using graphene nanoresonators. An analytic formula for the critical resonant frequency based on the interaction between water molecules and graphene is provided. Furthermore, the properties of the water chains assembled by the graphene nanoresonators are studied.

Contents

1	Introduction	1
1.1	Background	1
1.2	Motivation	2
1.3	Objectives of the dissertation	5
1.4	Dissertation organization	5
2	Modeling and Dynamic Characterization of Nanomechanical Resonators	7
2.1	Modeling of nanoresonators	9
2.1.1	Continuum modeling	9
2.1.2	Molecular simulations	10
2.2	Dynamics of NEMS resonators	13
2.2.1	Energy dissipation mechanism in nanoresonators: Q-factors	13
2.2.2	Mechanical modulation of resonance behavior	15
2.3	Carbon nanotube resonators and graphene sheet resonators	17
3	The Fundamental Properties of Quasi-two-dimensional Materials	19
3.1	Introduction	19
3.2	Molybdenum disulphide	20
3.2.1	Structure	20
3.2.2	Interatomic potential	21
3.2.3	Mechanical properties	22
3.2.4	Nanomechanical resonators	24
3.2.5	Electronic band structure	25
3.3	Black phosphorus	25
3.3.1	Structure	25
3.3.2	Interatomic potential	26
3.3.3	Mechanical properties	26
3.3.4	Nanomechanical resonators	28
3.3.5	Electronic band structure	28
3.4	Graphene	29
3.4.1	Structure and interatomic potential	29

CONTENTS

3.4.2	Mechanical properties	30
3.4.3	Nanomechanical resonators	31
3.4.4	Electronic band structure	32
4	Self-actuated Breathing-like Oscillation	33
4.1	Introduction	33
4.2	2D CG model development	35
4.2.1	Parametrization of SW potential of 2D CG model based on VFF model	36
4.2.2	Application	46
4.2.3	Conclusion	48
4.3	1D CG model development	49
4.3.1	Atomic simulation for MoS ₂	50
4.3.2	Parametrization of 1D CG model	53
4.3.3	Application of 1D CG model to folded MoS ₂	59
4.3.4	Conclusion	67
4.4	Comparison	68
5	Mechanical Engineering for Black Phosphorus Nanoresonators	69
5.1	Introduction	69
5.2	Structure and simulation details	71
5.2.1	Structure	71
5.2.2	Interatomic potential	71
5.2.3	Simulation details	73
5.3	Results and discussion	74
5.3.1	Intrinsic energy dissipation of the pristine SLBPRs	74
5.3.2	Mechanical strain effects on SLBPRs	78
5.3.3	Defect effects on SLBPRs	81
5.4	Conclusion	87
6	Self-assembly of Water Molecules Using Graphene Nanoresonators	89
6.1	Introduction	89
6.2	Structure and simulation details	91
6.3	Results and discussions	92
6.3.1	Assembly of water molecules	92
6.3.2	Frequency effects on assembly	93
6.3.3	H-bonds	96
6.4	Conclusion	97

CONTENTS

7	Conclusions	99
7.1	Summary of achievements	99
7.2	Outlook	101
	References	102
	Curriculum Vitae	135

List of Figures

2.1	The vibrational behavior of microcantilevers, typically utilized in atomic force microscopy, with different force constants (spring constants) and/or geometries. ¹¹⁴	11
3.1	Top view of the structure of SLMoS ₂ . The red rhombus encloses the unit cell. The lattice constant is 3.09 Å and the bond length is 2.39 Å.	20
3.2	Optimized configuration of SLBP. ³⁷ (a) Perspective view illustrates the pucker along the y-direction. (b) Top view of top image shows a honeycomb-like structure. The blue box represents the basic unit cell for SLBP.	26
3.3	Top view of the structure of graphene. The red rhombus encloses the unit cell. The lattice constant is $a = 2.46$ Å and the bond length is $b = 1.42$ Å.	29
4.1	The top view of a bottom-up scalable 2D CG simulation scheme of SLMoS ₂ . Mapping from atomic SLMoS ₂ in (a), to 1st and 2nd order 2D CG models in (b) and (c), respectively. The hexagonal lattice symmetry is maintained in all CG structures of any levels, and the positions of Mo _{<i>i</i>} beads and S _{<i>i</i>} beads in the 2D CG model are the same as Mo atoms and S atoms, respectively, in the original atomic SLMoS ₂ . Note that the 2D CG model is applied to “in-plane” (projection of all atoms onto one plane) only, with out-of-plane direction unchanged. . .	36
4.2	Configuration of <i>i</i> th order 2D CG model. There are total four kinds bonds; i.e., one kind real bond (ξ_{0_i}) and three kinds virtual bonds (ξ_{θ_i} , ξ_{ψ_i} and ξ_{ϕ_i}). The x-axis is in the armchair direction, and the y-axis is in the zigzag direction.	37
4.3	Two neighboring CG layers with the side view in (a) and perspective view in (b).	43
4.4	Stress versus strain (The dimension of SLMoS ₂ is 35 * 35 Å).	47
4.5	Strain y - strain x curve.	48
4.6	Fourier transformation.	49

LIST OF FIGURES

4.7	Adsorption effects on the resonant frequency.	50
4.8	Structure for the bilayer MoS ₂ with dimensions of 32 * 32 Å, from the top view in the top panel, and from the side view in the bottom panel.	51
4.9	The relative interlayer potential for the bilayer MoS ₂ with respect to different interlayer spacings dz . For $dz = 0$, the interlayer space is at the equilibrium value of 6.17 Å. The cohesive energy is around 20.2 meV/atom, which is the energy required to depart two coupling MoS ₂ layers.	52
4.10	Stress versus strain. SLMoS ₂ dimensions: 35 * 35 Å.	53
4.11	Strain y - strain x curve.	54
4.12	Atomic and corresponding 1D CG model of SLMoS ₂ . (a) The atomic representation of SLMoS ₂ , which is substituted by (b), a chain of beads interacting with various molecular potentials.	55
4.13	Two neighboring CG chains.	58
4.14	ϵ versus different cut-off series numbers.	59
4.15	Optimized structure of the folded MoS ₂ at 0 K. There are three representative positions in the folded structure; i.e., ‘a’ on the parallel segment, ‘b’ at the junction of left and right parts, and ‘c’ on the curvature part.	60
4.16	Analytic relationship between the geometrical parameters R and α . The points are from CG or MD simulations.	62
4.17	Bending energy of the folded MoS ₂ . $T = 80K$, $N = 52$	63
4.18	Fourier transformation. The red line shows the Fourier transformation result. There are many different oscillations, but the peak magnitude shows the frequency of the most obvious one, i.e. the breathing-like oscillation. The blue line shows the fitting results: $f_c = 9.6GHz$ and $\gamma = 3.153GHz$	65
4.19	Temperature effects on the resonant frequency.	66
4.20	Adsorption effects on the resonant frequency.	67
4.21	Relaxed atomic structure of the folded SLMoS ₂ , with $\alpha = 26.0^\circ$ and $R = 18.2 \text{ \AA}$	68
5.1	(a) Configuration of SLBP with dimensions 50 * 50 Å, containing a SV defect, a DV defect and an oxidized defect. Arrows in the bottom image indicate the direction of actuation. (b) Configuration of SLBP with an oxidized defect. There are two interaction terms associated with the oxygen atom, i.e., the bond-stretching term (bond 1-7) and the angle-bending term ($\angle 712$, $\angle 713$ and $\angle 714$). The x-axis is along the armchair direction, and the y-axis is along the zigzag direction.	72

LIST OF FIGURES

5.2	The kinetic energy per atom for armchair SLBPRs at 4.2 K, 30 K and 50 K from top to bottom. The Q-factors are 1621900, 110000 and 63250, respectively.	75
5.3	Two-step fitting procedure to extract the frequency and Q-factor from the kinetic energy time history for armchair SLBPR at 50 K. (a) The kinetic energy is fitted to the function $E_k(t) = \bar{E}_k + E_k^0 \cos(2\pi 2ft)$ in a small time range, giving a frequency of $f = 0.090874$ THz. (b) The kinetic energy is fitted to the function $E_k^{\text{amp}}(t) = E_k^0(1 - \frac{2\pi}{Q})^{ft}$ in the whole time range, yielding the Q-factor value of 63250.	76
5.4	Temperature dependence for the Q-factors of the armchair and zigzag SLBPRs.	77
5.5	Strain dependence for the Q-factor of SLBPR in four cases at 50K. The Q-factor depends on the strain as the function $Q/Q_0 = a\epsilon^2 + b\epsilon + 1.0$, which gives a maximum Q-factor value at a critical strain.	78
5.6	Stress-strain relation for SLBP under mechanical tension. The stress (σ) is fitted to a function of the strain (ϵ) as $\sigma = E\epsilon + \frac{1}{2}D\epsilon^2$, with E as the Young's modulus and D as the TOEC. The nonlinear effect is estimated by the ratio $\gamma = \frac{1}{2}\frac{D}{E}\epsilon$	79
5.7	Strain dependence for the Q-factor of SLBPR in four cases at 170K.	80
5.8	The kinetic energy per atom for zigzag SLBPRs at 4.2 K with different concentrations of SV defects: 0%, 1% and 2% from top to bottom. The Q-factors are 875950, 320000 and 162000, respectively.	82
5.9	Defect (SV and DV) concentration dependence for the Q-factors of the SLBPRs along the armchair and zigzag directions at (a) 4.2 K and (b) 50 K. The percentage values show the reduction percentage.	83
5.10	The dependence of the Q-factor on the pattern of the vacancy defect. (a) The SLBP containing four SV defects (dashed circle) patterned in a line with a tilt angle α with respect to the oscillation direction. (b) The Q-factors of the SLBPRs along the armchair and zigzag directions at 4.2 K with different α	85
5.11	Oxidized defect concentration dependence for the Q-factors of the armchair and zigzag SLBPRs at (a) 4.2 K and (b) 50 K.	86
6.1	Configuration for the GNMR. Water molecules are randomly distributed on the graphene sheet (red atoms) of dimensions $100 * 30 \text{ \AA}$	90
6.2	Self-assembly of water molecules by GNMRs. The resonant oscillations for mode indices $n = 1$ for panel (a) and $n = 2$ for panel (b). Water molecules are assembled at the positions with maximum amplitude.	92
6.3	(a) Initial configuration for the circular GNMR, with radius 50 \AA . (b) Water molecules are assembled at the center of the CGN.	93

LIST OF FIGURES

6.4	Frequency effects on the self-assembly of water molecules with mode index $n = 1$, with 4 different frequencies ($10f_\pi$, $30f_\pi$, $80f_\pi$ and $100f_\pi$ for panels from (a) to (d)).	94
6.5	Assembly position versus frequency for mode index $n = 1$	95
6.6	The motion of a self-assembled water cluster during one oscillation cycle, with $f_g < f_{wg}$	96
6.7	Frequency effects on H-bonds.	97

List of Tables

4.1	Structure parameters for atomic SLMoS ₂ (i.e. 0th order ²²⁵) and 1st order 2D CG model.	38
4.2	The VFF model parameters ²²⁷ for atomic SLMoS ₂	41
4.3	Tensile parameters for the atomic SLMoS ₂ and the 1st order 2D CG model.	42
4.4	SW potential parameters for the 0th order 2D CG model for SLMoS ₂ (i.e. atomic SLMoS ₂) used by LAMMPS. ²³⁰ The two-body potential expression is $V_2 = \epsilon A (B \sigma^p r_{ij}^p - \sigma^q r_{ij}^q) e^{[\sigma(r_{ij} - \alpha \sigma)^{-1}]}$. The three-body potential in the 2D CG model is equated to two-body potential. Parameters λ and $\cos\theta_0$ are set to 0 due to that they are used only for three-body interactions. The quantity tol in the last column is a controlling parameter in LAMMPS.	45
4.5	SW potential parameters for the 1st order 2D CG model for SLMoS ₂ used by LAMMPS. ²³⁰	45
4.6	Quantities from molecular mechanics simulations using the SW potential.	53
4.7	Parameters in the 1D CG model of the SLMoS ₂	59

Chapter 1

Introduction

1.1 Background

In the past decade, nanotechnology has opened a new area in science and engineering, enabling the development of nanoscale functional devices designed for specific aims such as nanoscale detection, sensing, and actuation.^{1,2} For example, nano-electromechanical system (NEMS) devices have allowed the sensitive detection of physical quantities, such as molecular mass,³ thermal fluctuation,⁴ spin,⁵ quantum state,⁶ biochemical reactions⁷ and coupled resonance.⁸ Among NEMS devices, nanomechanical resonators have shown an exceptional ability for their unprecedented dynamic characteristics, since that they can reach ultra-high frequency and/or very-high-frequency dynamic behavior up to the giga hertz (GHz = 10^9 Hz) range.^{9,10} Nanoresonators with this frequency regime can be directly utilized as electronic devices for radio communications. Such high-frequency dynamic behavior is achieved by scaling down the size scale of the resonator, because the frequency of the resonator is proportional to L^{-2} , with L as the length of a device. That means if the resonator length is decreased by one order of magnitude, the frequency of the resonator should increase by two orders of magnitude. Furthermore, the resonant frequency is closely related to the ability of the resonators to sense or detect physical quantities (i.e. pressure, force or mass). For instance, for the sensing mass that is added onto a resonator, the detection sensitivity is given by the relation $\Delta f_n / f_n \propto \Delta m / m = (1/2m)f_n^{-2} \Delta m$,¹¹ where f_n and m represent the resonant frequency and the effective mass of a device, respectively, while Δf_n and Δm indicate the resonant frequency shift and the added mass, respectively. Obviously, this relationship suggests that as the resonator frequency increases, so does the ability to detect or sense ever smaller masses, which implies that ultra-high frequency and/or very-high-frequency resonators are suitable for ultra sensitive detection, where the eventual limit of a single molecule or atom is experimentally within reach.

1. INTRODUCTION

Recent works by Roukes and coworkers^{3,12} have shown the incredible potential of NEMS resonators, where the possibility of nanoscale mass spectrometers that enable the measurement of the molecular weight of specific molecules is shown. This implies not only that nanomechanical resonators could be a viable alternative to conventional mass spectrometry techniques such as matrix-assisted desorption/ionization time-of-flight, but also that mass spectrometry could be realized in a lab-on-a-chip.¹³ It should be emphasized that NEMS-based sensing is not restricted to small atom or molecular masses; other physical quantities such as spin⁵ and quantum state⁶ can also be detected using NEMS, which suggests nanomechanical resonators may allow the realization of lab-on-a-chip sensing toolkits for detecting other relevant physical quantities.¹

In recent years, nanomechanical resonators have also received much attention for their capability of label-free detection of specific biological molecules^{14,15,16} and/or cells,^{7,17} even at very low concentrations, which are closely relevant to specific diseases such as cancer.¹⁸ However, current biosensing tools such as enzyme-linked immunosorbent assay (ELISA) exhibit a key restriction in that they are unable to accurately detect marker proteins, which are relevant to specific cancers, in the concentration of $\approx 1\text{ ng/ml}$, which is widely known as diagnostic gray zone,¹⁹ in blood serum. On the other hand, nanomechanical resonators are able to easily overcome the diagnostic gray zone limitation because of their unprecedented detection sensitivity even at single-atom resolution,^{14,20} which shows that nanomechanical resonators can serve as lab-on-a-chip biosensors enabling the early diagnostics of important diseases such as cancer.

1.2 Motivation

Recent studies on the development of nanomechanical resonators and their applications in sensing have been briefly introduced. As we know, quasi-two-dimensional (Q2D) materials have many novel properties and have attracted intensive research interest during the past decades. Thus how about the dynamic characteristics of the nanoresonators based on Q2D materials should be a critical issue.

The size of the family of Q2D materials keeps expanding. Currently, the Q2D family contains the following materials: graphene, two-dimensional (2D) honeycomb silicon, layered transition metal dichalcogenides (including MoS_2 and WS_2), hexagonal boron nitride, black phosphorus (BP) and 2D ZnO.²¹ In this work, we focus on MoS_2 , BP and graphene, to investigate the dynamic characteristics of their nanoresonators.

Method development

1.2 Motivation

As we know, for theoretical investigations, first-principles technique is the most accurate approach because of its ability to provide quantum mechanically-based predictions for various properties of Q2D materials. However, it is well-known that first-principles technique cannot simulate more than around a few thousand atoms, which poses serious limitations for comparisons with experimental studies, which typically occur on the micrometer length scale. For such larger size, classical molecular dynamics (MD) simulations are desirable, which require interatomic potentials. For instance, several atomic potentials have been proposed for MoS₂ and single layer MoS₂ (SLMoS₂), including the valence force field (VFF) model,⁷⁸ the Brenner-like atomic potential,⁷⁹ and the Stillinger-Weber (SW) atomic potential.⁸⁰ Besides these atomic potentials, the coarse-grained (CG) model is another useful potential to support simulations for even larger system size. The CG model simplifies the atomic system by introducing CG beads, and the atomic interaction is replaced by CG potential. One-dimensional (1D) CG models have been used to simulate quasi-one-dimensional nanostructures.^{81,82,83} The CG model has also achieved great success in biophysics.^{84,85} Therefore, it is significant to establish the CG potentials for Q2D materials so that theoretical studies can be compared with experimental studies with larger sizes.

Mechanism understanding

Theoretical studies on the underlying mechanism of energy dissipation of the nanomechanical resonators based on Q2D materials are quite finite. Especially, there have been no theoretical studies on the intrinsic dissipation in BP resonators (BPR) to-date.

BP is a new 2D nanomaterial that is comprised of atomic layers of phosphorus stacked via van der Waals forces.²² BP brings a number of unique properties unavailable in other 2D crystal materials. For example, BP has anisotropic properties due to its puckered configuration.^{23,24,25,26} While most existing experiments have been focused on potential electronic applications of BP,^{27,28,29} a recent experiment showed that the resonant vibration response of BPRs can be achieved at a very high frequency.³⁰ Thus, it is urgent to examine the intrinsic energy dissipation in BPRs. In particular, it is interesting and important to characterize the effects of mechanical strain on the quality (Q)-factors of BPRs, and furthermore considering that mechanical strain can act as an efficient tool to manipulate various physical properties in the BP structure.^{31,32,33,34,35,36,37,38} For example, a large uniaxial strain in the direction normal to the single-layer BP (SLBP) plane can even induce a semiconductor-metal transition.^{39,40,41,42} Thus, it is also urgent to investigate the mechanical strain effects on the BPRs of armchair and zigzag directions, at different temperatures.

Very recently, Feng's group has examined the BPR experimentally.⁴³ Currently, SLBP, i.e. phosphorene,²⁴ can be fabricated by mechanical exfoliation from bulk BP

1. INTRODUCTION

and has immediately received considerable attention.^{44,45,46} Atomic vacancies have been demonstrated to exist in bulk BP.^{47,48} Recently, first-principle calculations have demonstrated that these defects can be generated quite easily in SLBP at much higher concentrations compared with silicene and graphene.^{49,50} Cai et al.⁵¹ suggested that intrinsic itinerant behavior of atomic vacancies may result in the low chemical stability of phosphorene. In addition, another invariable issue encountered in the manipulation of SLBP is the control of the oxidation. It has been established by both theoretical calculations and experiments that O_2 can easily dissociate on black phosphorene^{52,53} leading to the formation of the oxidized lattice.⁵⁴ The presence of oxygen is suggested to be the main cause of the degradation process^{52,55} and primarily responsible for changing properties of BP,⁵⁶ e.g., BP is turned progressively hydrophilic by oxidation. Obviously, the experimental BPR samples should have some unavoidable vacancy defects or oxidation.⁴³ Furthermore, these defects can have strong effects on the performance of resonant oscillations of the nanomechanical resonators. For instance, it has been known that various defects can significantly affect the performance of the graphene nanomechanical resonators.^{57,58,59} An important task is thus to examine the effects of the vacancy defect and oxidation on the BPRs.

Application

As another very popular Q2D material, graphene is a monolayer of carbon atoms in the honeycomb lattice structure, and has attracted much attention since its discovery.^{60,61} It is an attractive platform for NEMS^{62,63} due to its atomic thickness, low mass density, high stiffness and high surface area.^{64,65} Several recent works have shown that graphene nanomechanical resonators (GNMR) are a promising candidate for ultrasensitive mass sensing and detection.^{62,66} The Q-factors, and thus sensitivity to external perturbations like mass and pressure, are limited by both extrinsic and intrinsic energy dissipation mechanisms, including attachment induced energy loss,^{67,68} non-linear scattering mechanisms,⁶⁹ edge effects,⁷⁰ the effective strain mechanism⁷¹ and thermalization due to nonlinear mode coupling.⁷² The interplay between graphene and adsorbates has been investigated in many works. It was experimentally shown that pristine graphene sheets are impermeable to standard gases, including helium.^{63,73} The adsorption of Helium atoms on graphene has also been discussed,^{74,75,76} while Jiang et al studied the adsorption effect of metal atoms on the Q-factors of graphene resonators.⁷¹ Very recently, an experiment showed that metal atoms can be used as molecular valves to control the gas flux through pores in monolayer graphene.⁷⁷ However, an important issue that has not been investigated is whether it is possible to self-assemble adsorbates on the graphene surface into different types of nanostructures.

1.3 Objectives of the dissertation

The principal goal of this work is to investigate the dynamic characteristics of nanoresonators based on Q2D materials. The interrelated objectives are included as follows:

- (1) Develop 2D CG model of SLMoS_2 , with SW potential parameterized based on VFF model.
- (2) Investigate the relaxed configuration and the resonant oscillation of the folded MoS_2 using 1D CG simulations.
- (3) Reveal two energy dissipation mechanisms (i.e. mechanical strain effects and defect effects (including vacancy and oxidation)) on SLBP resonators (SLBPR) of arm-chair and zigzag directions via classical MD simulations.
- (4) Propose a new method to obtain water chains via assembling water molecules using graphene nanoresonators.

1.4 Dissertation organization

In the previous sections, some key issues that will be addressed in this research were identified through an introduction to the development of nanomechanical resonators and their applications in sensing, and the objectives of this work were clarified. The rest parts of the dissertation are arranged as follows:

Chapter 2 presents the modeling of nanoresonators, including continuum modeling and molecular simulations. After that, energy dissipation mechanism and mechanical modulation of resonance behavior are introduced.

Chapter 3 introduces the fundamental properties (including structure, interatomic potential, mechanical properties, nanomechanical resonators and electronic band structure) of Q2D materials, mainly focusing on MoS_2 , BP and graphene.

Chapter 4 parametrizes the 2D and 1D CG models of MoS_2 . 2D CG model is parametrized with SW potential, in which all SW geometrical parameters are determined analytically from the equilibrium condition for each potential term, while the SW energy parameters are derived analytically based on the VFF model. Then the adsorption effect on the resonant frequency is studied. Next, the 2D CG model is further simplified to 1D CG model. The folding of SLMoS_2 is examined using 1D CG simulations, in which all the parameters are determined analytically from the SW atomic

1. INTRODUCTION

potential. Owing to its simplicity, the 1D CG model is used to derive analytic predictions for the relaxed configuration of the folded MoS₂ and the resonant frequency for the breathing-like oscillation. Finally, the adsorption effect on the resonant frequency of the breathing-like oscillation is studied.

Chapter 5 performs classical MD simulations to reveal some underlying energy dissipation mechanisms of BPRs, including the effects of mechanical strain, vacancy and oxidation. More specifically, firstly, the temperature dependence for the Q-factor of the SLBPR along the armchair and zigzag directions is examined. In this step, two-step fitting procedure is used to extract the frequency and Q-factor from the kinetic energy time history. Next, the effects of mechanical strain on SLBPR at different temperatures are examined, and then the upper bound for the Q-factor increase due to nonlinear effects at large strains is analyzed. Furthermore, the energy dissipation of the SLBPRs with randomly distributed single vacancy (SV) and double vacancy (DV) defects along the armchair and zigzag directions is studied. After that, the effect of SV defects distributed in a line pattern on the SLBPR is investigated. Finally, to compare with vacancy defects, the effect of oxidation on both armchair and zigzag SLBPRs is examined.

Chapter 6 investigates the self-assembly of water molecules using graphene nanoresonators. An analytic formula for the critical resonant frequency based on the interaction between water molecules and graphene is provided. Finally, the average number of hydrogen bonds per water molecule in the water chains that are assembled by the graphene nanoresonators with different resonant frequencies is calculated.

Chapter 7 summarizes the works that have been presented in this dissertation. The main contributions of this research are outlined. Finally, some recommendations for future work are suggested.

Chapter 2

Modeling and Dynamic Characterization of Nanomechanical Resonators

Nanomechanical resonators made of graphene sheets,⁸⁶ carbon nanotubes (CNTs),⁸⁷ and nanowires⁸⁸ have attracted much attention owing to their remarkable electrical and mechanical properties that enable them to reach the ultra-high resonant frequency up to the order of giga hertz.^{9,10} Reaching this high frequency range makes nanoresonators as ideal candidates for applications in nano-sensors for detection of molecules/atoms,^{12,89} nanopumping devices for molecular transportation,⁹⁰ and membranes for separating molecules and atoms without any phase changes.⁹¹

In the past decade, extensive efforts have been dedicated to design new classes of sensors with high sensitivity, high consistency and fast response. In order to fulfill all these requirements, reduction in the sizes of sensors is of great significance, because it improves the robustness of sensors, enhances the sensitivity performance, and allows integration of much more functions in small lab-on-a-chip device. The requirement for miniaturized sensors motivated scientists to develop the sensors with higher efficiencies in nanoscale size, so-called nano-sensors.^{92,93} Nano-sensors are promising in a wide variety of applications such as detection of gene mutations, DNA sequencing, early disease detection, and gas detection.^{94,95}

Regarding parameters that are detected by nano-sensors,⁹⁶ the sensors are categorized into six main groups:⁹⁷ chemical, mechanical, electrical, magnetic, optical, and thermal. For instance, mechanical nano-sensors detect mechanical variables such as wave velocity, frequency, strain, and pressure. Among these different types of nano-

2. MODELING AND DYNAMIC CHARACTERIZATION OF NANOMECHANICAL RESONATORS

sensors, nanomechanical resonator sensors have shown an exceptional ability to design the mass spectrometers with ultra-high mass sensitivity, which enables to detect molecules or atoms at quite low concentrations,^{3,98,99,100} while the existing sensors may be not able to fulfill this accurate detection. For instance, present bio-sensing devices cannot accurately detect the marker proteins, which are relevant to specific cancers, in the concentration of 1 ng/ml in a blood sample.¹⁹ Conversely, nanoresonator sensors can easily overcome this limitation due to their exceptional detection sensitivity even at single-molecule resolution,^{20,101} which enables them to be applied in the lab-on-a-chip sensors. Different techniques that have been proposed in the literature for designing nanoresonator sensors can be generally categorized into two major groups: wave propagation-based,^{102,103,104} and vibration-based methods.^{95,102} The principle of the resonator sensors is to recognize shifts in wave velocities or resonant frequencies, induced in the sensors by surrounding molecules or atoms on their surfaces.

Apart from the application of nanoresonators in sensors, the morphology of nanomaterials provides an excellent opportunity to develop a new generation of nanodevices for molecular transportation and separating molecules and atoms,^{105,106} which significantly reduces the energy consumption compared with the traditional approaches. The molecular separation has great potential in many areas such as clean energy and chemical industries, including water purification, nitrogen generation, and hydrogen recovery.^{107,108}

The performance of nanoresonators for transportation and sensing applications strongly depends on the dynamic characteristics such as the Q-factor.^{11,93} The Q-factors reflect the energy dissipation for each vibrational cycle of the nanoresonators, which can be affected by the edge effects,⁷⁰ external attachment energy loss,⁶⁸ the effective strain mechanism,⁷¹ intrinsic nonlinear scattering mechanisms,⁶⁹ temperature scaling phenomenon,¹⁰⁹ and grain-boundary-mediated scattering losses.⁵⁷ Moreover, the structure of nanoresonators has been found to have a large surface-to-volume ratio, which results in a difference of the nature of chemical bonds on the surface.¹¹⁰ Surface atoms have fewer bonds compared with bulk atoms, thus, their equilibrium requirements are different from the atoms within the bulk. This difference induces surface stresses,¹¹¹ which in turn affect the properties of the nanoresonators. Thus, it is indispensable to characterize the dynamic behavior of nanoresonators for novel designs of resonator-based devices.

In this chapter, we mainly focus on the brief introduction of the modeling and dynamics of nanoresonators. In addition, we also summarize the most recent achievements on carbon nanotube resonators and graphene resonators.

2.1 Modeling of nanoresonators

Besides experiments, which are formidable but expensive at nanoscale, there are two main approaches for modeling the nanostructures: continuum mechanics and MD simulations. Continuum mechanics models are considered as low computational cost approaches with relatively simple formulations compared with MD method. However, continuum models are unable to provide detailed information about the molecular interactions, which hinder the achievement of in-depth insights into the underlying mechanisms of phenomena at the atomic level. MD simulations, in contrast, enable to investigate the characteristics of nanoresonators including detailed molecular interactions.

2.1.1 Continuum modeling

Here we first introduce the well-known Bernoulli-Euler beam theory,^{112,113} which is able to capture the vibrational motion of micro-/nano-electro-mechanical systems (MEMS/NEMS) devices, with characteristic sizes ranging from micro- to nano-meters. These devices (e.g. nanotube, nanowire, microcantilever) generally have a geometry such that the longitudinal dimension (i.e. length) is much larger than the transverse dimensions (i.e. width and thickness). This indicates that this kind of devices can be modeled as a 1D elastic beam, which assumes that the vibrational motion of NEMS devices is governed by the flexural motion. The vibrational motion of NEMS can be consequently described by the following equation of motion:

$$EI \frac{\partial^4 w(x,t)}{\partial x^4} + c \frac{\partial w(x,t)}{\partial t} + \rho A \frac{\partial^2 w(x,t)}{\partial t^2} = 0, \quad (2.1)$$

where $w(x,t)$ is the flexural deflection as a function of the coordinate x and time t , c is a damping coefficient due to the viscous damping effect, and E , I , ρ , and A are the elastic modulus, the cross-sectional moment of inertia, the mass density, and the cross-sectional area of the device, respectively.¹¹⁴ Here, it is assumed that the device experiences vibrational motion with very small deflection amplitude, which means that it follows the harmonic approximation. In other words, in the theoretical model, as given in Eq. (2.1), the effect of geometric nonlinearity has been neglected, while the mathematical method to account for the geometric nonlinearity is demonstrated in Eq. (2.6), where $f(x,t)$ is the actuating force per unit length induced by an external field such as an electric field,^{115,116,117} magnetic field,¹¹⁸ and/or optical drive.¹¹⁹ Furthermore, for the cases, where the devices vibrate in air or vacuum, the damping effects on the resonant frequency can be ignored. By writing the flexural deflection in the following

2. MODELING AND DYNAMIC CHARACTERIZATION OF NANOMECHANICAL RESONATORS

form

$$w(x,t) = u(x) * \exp[j\omega t], \quad (2.2)$$

where ω and $u(x)$ indicate the resonant frequency and its corresponding deflection eigenmode, respectively, and j is a unit of complex number, i.e., $j = (-1)^{1/2}$. We can transform the equation of motion into the following eigenvalue problem:

$$\wp u = \lambda u, \quad (2.3)$$

where

$$\wp = EI \frac{\partial^4}{\partial x^4} \quad (2.4)$$

and

$$\lambda = \omega^2 \rho A. \quad (2.5)$$

When a specific boundary condition is prescribed, the resonant frequency and its corresponding deflection eigenmode can be straightforwardly obtained from the eigenvalue problem given in Eq. (2.3), Eq. (2.4) and Eq. (2.5). As shown in Fig.2.1, the vibrational behavior of microcantilevers is typically utilized in atomic force microscopy, with different force constants (spring constants) and/or geometries. It shows that the theoretical model in Eq. (2.1) has well described the fundamental deflection eigenmode, while due to the coupling between torsional motion and flexural motion, the high-frequency deflection eigenmode is less accurately captured.¹²⁰ In order to capture accurately the mode coupling in the high-frequency behavior in an atomic force microscopy cantilever, it is important to include the terms related to the torsional motion in the equation of motion. Generally, it is very difficult to analytically solve the equation of motion for such a case, while this equation of motion can be computationally tractable using the finite element approach.¹²¹ The topic of mode-coupling in the vibrational dynamics of micro/nanocantilevers has been recently received special attention because the mode-coupling has been found to improve the atomic force microscopy imaging quality.^{122,123,124}

$$EI \frac{\partial^4 w(x,t)}{\partial x^4} - \left[\frac{EA}{2L} \int_0^L \left\{ \frac{\partial w(x,t)}{\partial x} \right\}^2 dx \right] \frac{\partial^2 w(x,t)}{\partial x^2} + \mu \frac{\partial^2 w(x,t)}{\partial t^2} = f(x,t) \quad (2.6)$$

2.1.2 Molecular simulations

Nanoresonators have various potential applications in the nanotechnology industry owing to their excellent features. Then it is crucial to have a very good understanding of

2.1 Modeling of nanoresonators

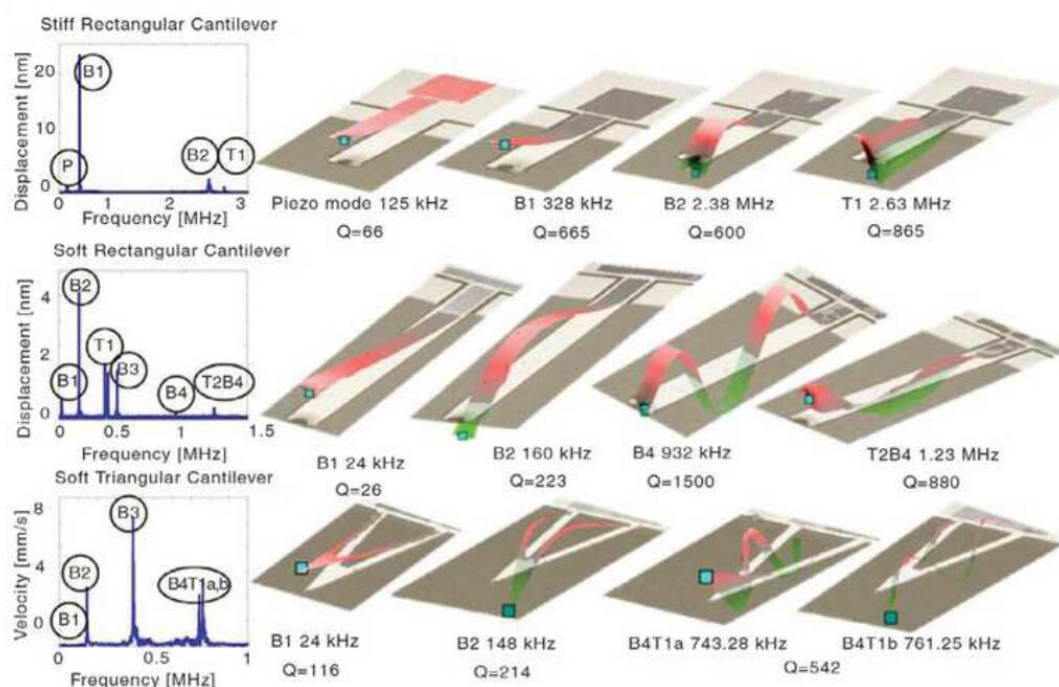


Figure 2.1: The vibrational behavior of microcantilevers, typically utilized in atomic force microscopy, with different force constants (spring constants) and/or geometries. 114

mechanical behaviors of the resonators. While the continuum mechanics methods enable a good understanding of the dynamic behavior of nanoresonators, they are unable to provide detailed mechanisms of molecular/atomic interactions between the nanoresonators and adsorbed molecules, which can induce the resonant frequency shifts. Furthermore, it is difficult for continuum models to reveal fundamental insights into the underlying mechanisms of some phenomena at the atomic level such as energy dissipation mechanisms in nanoresonators. These limitations impact the ability of continuum mechanics to predict the dynamic behavior of nanoresonators. Molecular simulations, in contrast, provide a pathway to investigate the characteristics of nanoresonators, including the detailed atomic interactions.

MD simulation^{125,126} is a powerful tool to simulate atomistic systems governed by interatomic interactions by solving Newtonian equations of motion.¹²⁵ A molecular simulation contains the following three parts. (1) A model that describes interactions between atoms called force fields. Normally it is prescribed using an empirical

2. MODELING AND DYNAMIC CHARACTERIZATION OF NANOMECHANICAL RESONATORS

potential field. An empirical potential field prescribed to atoms generally consists of covalent bond stretch energy, bending energy of bond angle, energy for twist of dihedral angle, and non-bonded interactions such as van der Waal's interaction and electrostatic interaction. (2) A numerical time integrator algorithm that determines the trajectories of atoms during the time. A related, and more commonly used, algorithm is the velocity Verlet algorithm. Eliminating the half-step velocity, this algorithm may be shortened to: (a) Calculate $\bar{x}(t + \Delta t) = \bar{x}(t) + \bar{v}(t)\Delta t + \frac{1}{2}\bar{a}(t)\Delta t^2$; (b) Derive $\bar{a}(t + \Delta t)$ from the interaction potential using $\bar{x}(t + \Delta t)$; (c) Calculate $\bar{v}(t + \Delta t) = \bar{v}(t) + \frac{1}{2}(\bar{a}(t) + \bar{a}(t + \Delta t))\Delta t$. (3) Extracting data from atomic trajectory information.⁹⁶

For instance, for the interatomic interactions between carbon atoms in CNTs and graphene sheets, the second-generation reactive empirical bond order (REBO) potential energy developed by Brenner et al.¹²⁷ is widely used as an underlying force field for hydrocarbons. In the second-generation REBO force field, the total potential energy of a system is given by

$$E_{rebo} = \sum_i \sum_{j=i+1} [E_R(r_{ij}) - \bar{b}_{ij}E_A(r_{ij})], \quad (2.7)$$

where E_R and E_A are repulsive and attractive interactions, respectively; r_{ij} is the distance between the pairs of adjacent atoms i and j ; and \bar{b}_{ij} is a many-bond empirical bond-order term. The Buckingham-type potential has also been utilized to describe the interatomic interactions of nanowires

$$E_{buck} = \sum_{i \neq j}^N A e^{\frac{r_{ij}}{\rho}} - \frac{C}{r_{ij}^6} + V_{long}(r_{ij}), \quad (2.8)$$

where N is the total number of ions. Short-range parameters A , C and ρ have been developed by Catlow¹²⁸ and Catlow and Lewis.¹²⁹ $V_{long}(r_{ij}) = q_i q_j / r_{ij}$ is the long-ranged Coulombic interaction, where q_i and q_j are the atomic charges.

Further to force fields, auxiliary algorithms are also necessary to impose initial boundary conditions and to control system states during the simulations, such as pressure and temperature. Among varied approaches proposed in the literature, Nosé-Hoover,^{130,131} Andersen,¹³² and Berendsen,¹³³ thermostats has been commonly used as the most accurate and efficient method to re-scale velocities of atoms in MD simulations for constant-temperature simulations. Molecular simulations have been widely used to investigate the dynamics of nano-materials.

Jiang et al.¹³⁴ performed MD simulations to study the effect of polar surfaces on the Q-factors of zinc oxide (ZnO) nanowire-based nanoresonators. In these simulations, the Buckingham-type force field^{128,129} is utilized to describe the interatomic

2.2 Dynamics of NEMS resonators

interactions. The Nosé-Hoover thermostat^{130,131} is employed to equilibrate the system at a constant temperature. Then the transverse vibrational motion is induced by adding a velocity distribution to the ZnO nanowire, which follows the morphology of the first bending mode of the wire. The system is then allowed to vibrate freely within the NVE (i.e., the particles number N , the volume V , and the energy E of the system are constant) ensemble. The decay of the oscillation amplitude of the kinetic/potential energy is then used to measure the Q-factor. Different approaches have been used in the literature to calculate the Q-factor.^{134,135,136} The maximum potential energy (E) is reduced to $E - \Delta E$ at the end of each oscillation cycle due to energy loss or damping, where ΔE represents the energy loss in each oscillation cycle. The Q-factor is thus defined as $Q = 2\pi E / \Delta E$. At the end of n cycles, the maximum potential energy E_n is related to the initial maximum potential energy (E) by $E_n = E(1 - 2\pi/Q)^n$.¹³⁶ Jiang et al.¹³⁴ proposed a method to measure the Q-factor by fitting the kinetic/potential energy of a resonator to a function $E(t) = a + b(1 - 2\pi/Q)^t \cos(\omega t)$, where ω is the resonator frequency, a and b are two fitting parameters, and Q is the resulting Q-factor.

Note that the choice of the correct potential is one of the most important factors in MD simulations. This choice depends on the various conditions such as the nature of simulations, the material being simulated, and the trade-off between accuracy and computational efficiency.⁹⁶

2.2 Dynamics of NEMS resonators

2.2.1 Energy dissipation mechanism in nanoresonators: Q-factors

Nanoresonators are promising in detection of forces, masses, and pressure due to their extremely low mass. However, the key issue limiting the sensitivity of the nanoresonators in practical applications is the Q-factor.^{137,138} The Q-factor is one of the characteristic performance measures for NEMS resonator, and can be described either as the full-width at half maximum of the experimentally measured resonance peak, or the rate at which the NEMS resonator loses energy per vibrational period due to the interactions with its environment or due to intrinsic defects or flaws in the NEMS resonator. Q-factors are critical for the sensing performance of NEMS resonator, because the ability of the NEMS resonator to sense changes in its environment, i.e. adsorbed masses, changes in force or pressure, is strongly-dependent on its Q-factor. More specifically, for the sensing applications, it is critical for the NEMS resonator to exhibit high Q-factor or low energy dissipation, since the sensitivity of the NEMS resonator is inversely proportional to its Q-factor.¹³⁹ The mass sensitivity of a NEMS resonator

2. MODELING AND DYNAMIC CHARACTERIZATION OF NANOMECHANICAL RESONATORS

can be written in the following form¹⁴⁰

$$\Delta m \approx 2m_0 \left(\frac{b}{Q\omega_0} \right)^{1/2} 10^{-DR/20}, \quad (2.9)$$

where Δm is the change in mass that is to be detected, m_0 is the mass of the resonator, b is the bandwidth, or the available frequency range of detection, ω_0 is the resonant frequency of the resonator with no attached mass, Q is the Q-factor and DR is the dynamic range of the resonator. Eq. (2.9) clearly demonstrates that a higher Q-factor is necessary to detect ever smaller masses Δm , which means the sensitivity of the NEMS is inversely proportional to its Q-factor. We note that similar inverse relationships between the sensitivity of the NEMS and the Q-factor can also be found in detecting other physical quantities.¹⁴¹

The factors that degrade the Q-factor can be categorized as extrinsic and intrinsic. Extrinsic damping mechanisms occur due to interactions of the NEMS resonator with its surrounding environment, e.g. the substrate on which it lies, or the air or gas molecules surrounding it. Intrinsic damping mechanisms occur due to defects or flaws inherent in the NEMS, for instance, atomic vacancies, grain boundaries, the dislocations, crystalline impurities, etc. Essentially, there are four major loss mechanisms for NEMS resonator; these are surface losses,^{2,142,143,144,145} thermoelastic damping losses,^{2,142,143,144,145,146,147} support or clamping losses,^{148,149,150} and gas damping losses.¹⁵¹ Support or clamping and gas damping losses are extrinsic factors, while thermoelastic damping and surface losses are intrinsic.

Surface losses exist in NEMS due to the fact that the atoms that lie at the surfaces of the NEMS have fewer bonding neighbors than atoms that lie within the bulk.¹¹⁴ Because of this, the surface atoms have a different vibrational frequency with the atoms that lie within the bulk. The importance of this on the Q-factor is that the resonant frequency of the surface atoms is also different from that of the overall NEMS; therefore, the NEMS resonance loses coherency due to the different vibrational frequency of the surface atoms, which leads to a decreased Q-factor with an increase in surface area to volume ratio. We have noted that research has shown that passivating surface atoms to make their bonding environments more bulk-like has resulted experimentally in higher Q-factors.^{152,153}

Support or clamping losses arise due to the fact that NEMS are generally fabricated on top of and clamped or fixed to substrates that are much larger than the operational NEMS device. The various analytical models that have been developed^{148,149,150} for Q-factor degradation due to clamping losses account for the fact that during the flexural motion that occurs during resonance, the waves that are generated in the NEMS device carry energy and leave the NEMS device by propagating into the substrate through the supports that fix the NEMS to the substrate. Judge et al.¹⁴⁸ developed

2.2 Dynamics of NEMS resonators

analytical models that accounted for both infinite and finite thickness substrates on Q-factor degradation, while Cross and Lifshitz¹⁵⁰ also considered energy dissipation due to wave propagation into surrounding substrate. Wilson-Rae¹⁴⁹ used a different approach, that of phonon tunneling between beams and supports, and also support-induced modification of the density of states, to develop estimates for support-induced Q-factor degradation for a variety of geometries.

Gas damping losses are also significant for NEMS, and exist due to the perpetual interaction (collisions) between the NEMS resonator and surrounding gas molecules or atoms. Gas damping effects tend to be more significant for NEMS than MEMS due to the fact that as the NEMS becomes smaller, the ratio of the mass between the NEMS and the surrounding gas molecules becomes non-negligible.¹¹⁴ In other words, while more massive MEMS can easily brush aside surrounding gas molecules during oscillation, NEMS can lose a significant amount of their energy via the collisions with the surrounding gas atoms or molecules.

Finally, NEMS can lose energy through so-called thermoelastic dissipation (TED).¹¹⁴ TED works via a mechanism in which a flexurally oscillating NEMS, due to being bent, has one surface that is in tension while the opposite surface is in compression. Due to thermomechanical coupling, the surface that is in compression becomes slightly warmer, while the surface that is in tension becomes slightly cooler; the resulting heat flow between the hotter and cooler surfaces is the source of TED as a non-recoverable loss of energy. Mathematically, TED has been accounted for by adding a thermal term to the classical Bernoulli-Euler beam equation of motion, i.e.:

$$\rho A \frac{\partial^2 u}{\partial t^2} + \frac{\partial^2}{\partial x^2} (EI \frac{\partial^2 u}{\partial x^2} + E\alpha I_T) = 0, \quad (2.10)$$

where α is the coefficient of thermal expansion and I_T is the thermal contribution to the beam's moment of inertia. It is likely that TED will be altered in NEMS due to the presence of surface stresses, which may enhance the tensile and compressive stresses that result at the surfaces of the NEMS due to the flexural mode of deformation.¹⁵⁴

2.2.2 Mechanical modulation of resonance behavior

2.2.2.1 Resonant frequency

Resonant frequency is fundamentally important, because it not only characterizes the NEMS devices, but also plays a critical role in detection sensitivity. This indicates that manipulation of the resonant frequency will enable the development of the high-frequency devices and mass sensors with increased detection sensitivity. One possible

2. MODELING AND DYNAMIC CHARACTERIZATION OF NANOMECHANICAL RESONATORS

method to tune the resonant frequency is to manipulate the actuation force driven via bias voltage as described in previous reference.^{116,117,155} Another possible approach is to apply the mechanical strain (or stress) to the beam, which leads to changes in the resonance behavior.^{156,157} The vibrational motion of a nanobeam, which is operated in air or vacuum under the application of mechanical stress σ_0 , can be described as

$$EI \frac{\partial^4 w(x,t)}{\partial x^4} - \sigma_0 A \frac{\partial^2 w(x,t)}{\partial x^2} + \rho A \frac{\partial^2 w(x,t)}{\partial t^2} = 0, \quad (2.11)$$

where the effects of gas damping are ignored for convenience, and E , I , A , and ρ represent the Young's (elastic) modulus, cross-sectional moment of inertia, cross-sectional area, and the mass density of a nanobeam, respectively. The mathematical solution to the eigenvalue problem resulting from Eq. (2.11) provides the resonant frequency in the form of $f_n = f_n^0 \sqrt{1 + \Gamma_n}$, where f_n^0 is the resonant frequency without any application of mechanical strain or stress, and Γ is the normalized mechanical tension, which is defined as $\Gamma_n = \sigma_0 L^2 / \alpha_n E t^2$, where L and t indicate the length and thickness of a nanobeam, respectively, and α_n is a constant that depends on the mode index n , e.g. $\alpha_1 = 3.4$ for fundamental flexural resonance for a doubly-clamped beam. It should be noted that, for the sign convention, a positive value indicates a tensile stress applied to the nanobeam, while a compressive stress is represented by a negative value. Here, the dimensionless parameter Γ_n provides the ratio of mechanical tension, i.e. $\sigma_0 A$, induced by applied stress to a critical load, i.e. $P_{cr} = \beta EI / L^2$, that induces the buckling of a nanobeam. If the mechanical tension induced by applied tensile stress is comparable to a critical load P_{cr} , then the resonance is significantly amplified. On the other hand, when a compressive stress is applied that is comparable to the critical load, the resonant frequency can be reduced considerably, which indicates that mechanical stress (or strain) is an important control parameter to modulate the resonance of NEMS. This hypothesis has been validated by recent experimental works,^{155,156} which show that resonant frequency of a doubly-clamped nanobeam can be increased by application of mechanical tension that affects the bending behavior.

2.2.2.2 Q-factors

Due to the importance of enhanced Q-factors for NEMS-based sensing applications, and due to the reduction in NEMS Q-factors due to surface damping, gas damping, clamping losses and thermoelastic damping, researchers have actively been looking for methods in which the Q-factors of NEMS can be enhanced. For instance, researchers at Cornell have had significant success in using mechanical stress to tune and enhance the Q-factors of NEMS made of various nano-materials. In these experiments, tensile stress was applied to both silicon nitride and single crystal silicon NEMS resonators by placing the NEMS resonators on a silicon wafer substrate.^{156,158} By bending and

2.3 Carbon nanotube resonators and graphene sheet resonators

flexing the substrate, the researchers were able to induce controllable tensile stress in the NEMS resonators. The effect of the tensile stress is that the Q-factor was able to be tuned and increased by several hundred percent, while eliminating a significant amount of the inherent clamping losses. Similarly, other researchers¹⁵⁹ fabricated AlN and SiC NEMS resonators on silicon substrates, then induced tensile strain in the NEMS by utilizing the thermal expansion mismatch between the NEMS and substrate. Q-factor enhancements of about one order of magnitude were reported for 50-250 nm thick NEMS with strains of about 0.0026 %.

In addition to experiments, other researchers have performed MD simulations to investigate the effects of the application of mechanical strain on the Q-factors of NEMS resonators. For example, Park and Kim have used classical MD simulations to study how the Q-factors of metal nanowires could be tuned using tensile strain¹⁶⁰. In doing so, they found that the Q-factors of 2 nm cross section copper nanowires could be increased by nearly an order of magnitude through the application of tension. To demonstrate that tensile strain could be utilized for various nanomaterials, they also examined the effects of strain on the Q-factors of monolayer graphene NEMS resonators.⁷⁰ Similar effects resulting in order of magnitude enhancements in the Q-factors of graphene were also found as a result of the tension application.

2.3 Carbon nanotube resonators and graphene sheet resonators

Atomistic simulations have been broadly employed to investigate the dynamics of molecular structures ranging from nanomaterials¹⁶¹ to biological structures at atomistic scales.^{162,163} Here we focus on the atomistic simulations of nanoscale resonators; of these, CNT and graphene-based nanoresonators have attracted the most attention.

Energy dissipation in oscillating CNTs has been investigated using classical MD simulations for both single-walled (SW) CNTs¹³⁶ and multi-walled (MW) CNTs.^{136,164,165} Of these, Jiang et al.¹³⁶ investigated the temperature dependence of Q-factor degradation in both free/fixed MWCNTs and SWCNTs, while other researchers^{164,165} mainly focused on frictional effects on energy dissipation in MWCNTs.

It should be noted that these works^{136,164,165} have focused exclusively on the effects of intrinsic mechanisms, i.e. interlayer friction and temperature, while the extrinsic mechanisms such as clamping and gas damping losses have been neglected. However, insights into the Q-degrading intrinsic mechanisms have been found. Specifically, Jiang et al.¹³⁶ found that the Q-factors of cantilevered CNTs degrade with increasing

2. MODELING AND DYNAMIC CHARACTERIZATION OF NANOMECHANICAL RESONATORS

temperatures according to a $1/T^{0.36}$ relationship. It is also found that the Q-factors of MWCNTs at a given temperature can be nearly one order of magnitude lower than the corresponding SWCNTs. Similar results regarding the deleterious effects of internal friction between CNTs on the Q-factor were found by Guo et al.¹⁶⁴ and Zhao et al.¹⁶⁵ Interestingly, a recent experimental study by Huttel et al.¹⁶⁶ on SWCNT resonators found the same relationship between Q-factor and temperature as did Jiang et al.,¹³⁶ though it is worth noting that the experimental study was performed across a very small range of low temperatures (20 mK to 1 K), while the boundary condition of the experiment differed from the cantilever boundary condition used in the MD simulation. It is also interesting that similar Q-factor dependence on temperature has been found for non-CNT systems, i.e. GaAs/InGaP/GaAs¹⁶⁷ and also single crystal silicon.¹⁶⁸

Classical atomistic modeling has also been employed to investigate the Q-factors of both mono- and multi-layer graphene NEMS resonators by Kim and Park.⁷⁰ Kim and Park have demonstrated that a key factor underlying the low Q-factors arises from so-called edge effects in graphene, where because graphene is a purely 2D material, the edge effects are analogous to surface effects on 3D nanostructures such as nanowires.^{169,170} Specifically, the edge atoms of the graphene NEMS were found to oscillate at different vibrational frequencies with the remainder of the graphene NEMS.⁷⁰ Due of this, the spurious edge modes were found in the simulations to quickly propagate into the graphene NEMS, thereby leading to vibrational incoherency, mode mixing, and a rapid loss in the Q-factors of graphene. Therefore, it has been determined that experimentally synthesized free-standing graphene NEMS, which thus have two free edges, are not optimal for high-Q graphene NEMS.

Kim et al.⁶⁸ also examined the Q-factors of multilayer graphene NEMS resonators, including both extrinsic effects and intrinsic effects (friction between the graphene monolayers). Interestingly, it has been found that the quality of the attachment between the graphene NEMS and the substrate had a strong effect on the Q-factor, where weaker attachment forces between the graphene NEMS and the substrate led to lower Q-factors. Similarly, it was determined that effective friction between graphene layers increased with a decrease in the relatively weak non-bonded van der Waal's interactions that govern the interactions between adjacent graphene layers; this friction between graphene layers also led to a significant loss in energy, and thus a lower Q-factor.

Chapter 3

The Fundamental Properties of Quasi-two-dimensional Materials

3.1 Introduction

Q2D materials have attracted intensive research interest due to their many novel properties over the past decades. The size of the family of Q2D materials keeps expanding. Currently the Q2D family contains the following materials: graphene, 2D honeycomb silicon, layered transition metal dichalcogenides (MoS_2 , WS_2 , ...), hexagonal boron nitride, BP and 2D ZnO.²¹ Graphene is the most well-known material among the Q2D family of materials. Novoselov and Geim were awarded the Nobel prize in physics for graphene in 2010.¹⁷¹

The investigations on graphene are extensive but not exhaustive.¹⁷² They are very helpful to the whole Q2D family, because many experimental set ups (initially for graphene) could be utilized to perform measurements for other materials in this family. For instance, the mechanical properties of SLMoS_2 have been successfully measured using the same nanoindentation platform as graphene.¹⁷³ In the theoretical community, many methods or theorems, initially developed to research graphene, are also applicable to other Q2D materials. Some of the extensions may turn out to be trivial due to the common 2D nature of these materials. However, the extensions may also bring about new findings as these Q2D materials exist different microscopic structures. For instance, the bending modulus of SLMoS_2 could be derived using the similar analytic method as that used for graphene even though the bending modulus of SLMoS_2 is around seven times larger than that of graphene, owing to its trilayer structure.^{174,175,176} Another example is BP, with the puckered microstructure, which leads

3. THE FUNDAMENTAL PROPERTIES OF QUASI-TWO-DIMENSIONAL MATERIALS

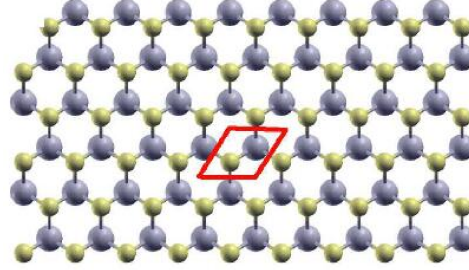


Figure 3.1: Top view of the structure of SLMoS₂. The red rhombus encloses the unit cell. The lattice constant is 3.09 Å and the bond length is 2.39 Å.

to a negative Poisson's ratio in the out-of-plane direction.¹⁷⁷

Thus, graphene attracted ongoing research interest from academic and applied communities. Many review articles have been dedicated to graphene.^{171,178,179,180,181,182} In addition, more and more researchers have begun using the knowledge gained from graphene to investigate possible applications of other Q2D materials. In particular, MoS₂ and BP have attracted considerable research interest. Many review articles have been published on MoS₂.^{183,184,185} BP also has a number of unique properties unavailable in other 2D crystal materials.^{23,24,25,26}

In this chapter, we focus on the introduction and comparison of the following properties for MoS₂, BP and graphene: the structure, interatomic potential, mechanical properties, nanomechanical resonator and electronic band structure.

3.2 Molybdenum disulphide

3.2.1 Structure

Fig. 3.1 shows the top view of the SLMoS₂ structure. SLMoS₂ has a trilayer structure with one Mo atomic layer sandwiched by two outer S atomic layers. The small yellow balls represent the projection of the two outer S atomic layers onto the Mo atomic layer. The point group for SLMoS₂ is D_{3h}. There are one Mo atom and two S atoms in the unit cell. Using the SW potential,²²⁵ the lattice constant for the in-plane unit cell can be obtained as 3.09 Å and the length of Mo-S bond is 2.39 Å. They agree quite well with the first-principles calculations²²⁶ and the experiments.²²⁷

3.2 Molybdenum disulphide

3.2.2 Interatomic potential

The atomic interaction is an important fundamental ingredient for numerical investigation of almost all physical or mechanical processes. For example, the atomic interaction in MD simulations provides the retracting force for each atom in the Newton's equation. There are large number of available potential models for interatomic potential within different materials. For covalent materials, there have been some representative potential models, e.g. SW potential, Brenner potential, Tersoff potential, VFF model and ab initio approaches.²⁶³ In the order of simulation cost, they should be VFF model, SW potential, Tersoff potential, Brenner potential, and ab initio approaches. All of these potentials (or approaches) can describe two dominant motion styles in covalent materials, i.e., bond stretching and angle bending motions.²⁶³

VFF model is a linear model. It is suitable for analytic derivation of lots elastic quantities, thus only limited computation cost is required for this model. As an important advantage, the parameters of the VFF model can be determined with high accuracy via fitting directly to some observable elastic quantities. As a result, this model was very popular for covalent materials, especially before 1980s, when the CPU speed was quite low. Consequently, VFF model has been well developed for most covalent materials. For example, the VFF model was proposed in 1975 for MoS₂,²²⁷ 1982 for BP,²⁶⁴ and 1990 for graphene by Aizawa et al.¹⁹² These VFF models are useful to study many elastic properties in these Q2D nanomaterials in recent years, especially during the gold rush of graphene in the past decade.

Although VFF model is beneficial for the fastest numerical simulation, it has a strong limitation, i.e., the absence of nonlinear effect. Owing to this limitation, VFF model is not applicable for nonlinear phenomena, for which other potential models (including SW potential, Tersoff potential, Brenner potential, and ab initio approaches) with nonlinear components are required. Ab initio approach is quite accurate and applicable for nonlinear phenomena, however, it requires the most expensive simulation cost, due to that the interatomic potential is treated as the summation of the Columb interaction among all electrons. As a result, this approach desires the most expensive simulation resources. Thus, ab initio approach normally cannot simulate more than a few thousand atoms, which exists serious limitations to compare with experimental studies.²⁶³

We have been aware that VFF model is the cheapest model in computation cost, but it can only work for linear elastic properties. On the other hand, ab initio approach can simulate almost all physical processes with high accuracy, but the most expensive computation cost is required. Thus, the bridging between (VFF model and ab initio approach) these two extreme cases is of practical significance, since lots of stud-

3. THE FUNDAMENTAL PROPERTIES OF QUASI-TWO-DIMENSIONAL MATERIALS

ies prefer efficient simulations with reasonable accuracy for the nonlinear phenomena. Until now, there have been several potential forms to fill this bridging domain, including Tersoff potential,^{265,266,267,268,269,270} SW potential,^{225,271,272} and Brenner potential.^{127,273} All these potential forms are particularly suitable for MD simulations and also comprise reasonable accurate nonlinear effects.

Among these potentials, SW potential, originally proposed by Stillinger and Weber to describe the interaction in solid and liquid forms of silicon, is one of the simplest potential models, with nonlinear effects included.²⁷¹ An advanced feature of SW potential is that it keeps the numerical simulation at a quite fast level, and simultaneously includes the nonlinear effects. Thus, SW potential has been widely used in the numerical simulation community.

For MoS₂, the potentials of five computation levels discussed above can also be used. First-principles calculations can be used for SLMoS₂. In 2009, Liang et al. parameterized a bond-order potential for SLMoS₂,⁷⁹ which was based on the bond order concept underlying the Brenner potential.¹²⁷ This Brenner-like potential was further modified to investigate the nanoindentations in SLMoS₂ thin films using a molecular statics method.²²⁸ Recently, Jiang²²⁵ has parameterized the SW potential for SLMoS₂, where potential parameters were fitted to the phonon spectrum. This potential could be easily used in some of the popular simulation packages, such as the General Utility Lattice Program (GULP)²²⁹ and the Large-Scale Atomic/Molecular Massively Parallel Simulator (LAMMPS).²³⁰ In 1975, Wakabayashi et al.²²⁷ developed a VFF model to calculate the phonon spectrum in bulk MoS₂. This linear model has been utilized to examine the lattice dynamical properties of some MoS₂ based materials.^{231,232}

3.2.3 Mechanical properties

The mechanical properties for SLMoS₂ have been extensively investigated.²³³ Here, several of the basic mechanical properties, including the Young's modulus, bending modulus, yield stress and buckling phenomenon, will be discussed. These mechanical properties are fundamental for the applications of the Q2D family materials in nanodevices. Good mechanical stability is essential in nanoscale devices, since they are sensitive to external perturbations because of their high surface to volume ratio.²¹

Young's modulus. The Young's modulus is given by $E = E^{2D}/h$, where E^{2D} is the thickness independent effective Young's modulus and h is the film thickness. The effective Young's modulus is discussed here. The thickness was chosen to be 6.09 Å for SLMoS₂. This value is half of the lattice constant in the bulk MoS₂. For SLMoS₂, nanoindentation experiments obtained an average value for the effective Young's mod-

3.2 Molybdenum disulphide

ulus E^{2D} of $120 \circ 30 \text{ N } \mu\text{m}^{-1}$, measured by Cooper et al.,²³⁴ and $180 \circ 60 \text{ N } \mu\text{m}^{-1}$ in the experiment by Bertolazzi et al..²³⁵ Recently, Liu et al. have performed similar nanoindentation experiments on chemical vapor deposited SLMoS₂, and obtained the effective Young's modulus of around $170 \text{ N } \mu\text{m}^{-1}$.²³⁶ The nanoindentation set up has also been used to investigate the Young's modulus of thicker MoS₂ films.²³⁷ The effective Young's modulus is theoretically predicted to be about $139.5 \text{ N } \mu\text{m}^{-1}$ for SLMoS₂, based on the SW potential.²²⁵

Yield stress. Yield stress (σ_{int} , the maximum of the stress-strain curve) can also be determined by the nanoindentation measurements. For SLMoS₂, nanoindentation experiments found that the yield stress was about $15 \circ 3 \text{ N } \mu\text{m}^{-1}$, determined by Bertolazzi et al.,²³⁵ and $16.5 \text{ N } \mu\text{m}^{-1}$, determined by Cooper et al.^{234,234} First-principles calculations have predicted the yield stress to be $17.5 \text{ N } \mu\text{m}^{-1}$ under a biaxial strain.²³⁸ While the work on yield stress is limited at the present stage, considerable attention has been paid to the novel structure transition in SLMoS₂.^{239,240} In this structure transition, the outer two S atomic layers are shifted relative to each other, leading to abrupt changes in the electronic and phonon properties in SLMoS₂. This structure transition is the result of the trilayer configuration of SLMoS₂ and is not observed in graphene.

Bending modulus. The bending modulus of SLMoS₂ was derived using the analytic approach, i.e., geometric approach with interactions described by the VFF model, or the exponential Cauchy Born rule using the Brenner potential. The bending modulus was found to be about 9.61 eV, which is larger than that of graphene by a factor of seven. Such larger bending modulus is mainly due to its trilayer atomic structure, which leads to more interaction terms inhibiting the bending motion. The bending modulus can be obtained in the following way:

$$D = \frac{\partial^2 W}{\partial k^2}, \quad (3.1)$$

with W as the bending energy density and k as the bending curvature. For SLMoS₂, the bending energy can be written as:²⁴¹

$$D = \sum_q \frac{\partial^2 W}{\partial r_q^2} \left(\frac{\partial r_q}{\partial k} \right)^2 + \sum_q \frac{\partial^2 W}{\partial \theta_q^2} \left(\frac{\partial \theta_q}{\partial k} \right)^2, \quad (3.2)$$

where θ_q and r_q are the geometrical parameters in the empirical potential expressions. This formula is substantially different from the bending modulus formula of graphene.²⁴² Specifically, the first derivatives, $\frac{\partial r_q}{\partial k}$ and $\frac{\partial \theta_q}{\partial k}$, are nonzero due to the trilayer structure of SLMoS₂. As a result, the bending motion in SLMoS₂ will be counteracted by an increasing number of cross-plane interactions.

Buckling phenomenon. The buckling phenomenon can be a disaster for the electronic devices, but it can also be useful in some situations.^{204,205,206} Euler buckling

3. THE FUNDAMENTAL PROPERTIES OF QUASI-TWO-DIMENSIONAL MATERIALS

theorem states that buckling critical strain can be obtained from the bending modulus and the effective Young's modulus through the following formula:

$$\varepsilon_c = \frac{4\pi^2 D}{E^{2D} L^2}, \quad (3.3)$$

with L as the buckling length, depending on the length and boundary condition. For SLMoS₂, using $E^{2D} = 139.5 \text{ N m}^{-1}$ and $D = 9.61 \text{ eV}$, described above, we can obtain the explicit formula for the buckling critical strain as:

$$\varepsilon_c = \frac{43.52}{L^2}, \quad (3.4)$$

with the units of length (L) as Å

3.2.4 Nanomechanical resonators

Nanoresonators based on Q2D materials are promising candidates for ultra-sensitive mass detection and sensing due to their small masses and large surface areas.^{207,208,209,210} For sensing applications, it is important for the nanoresonator to exhibit a high Q-factor due to that the sensitivity of a nanoresonator is inversely proportional to its Q-factor.¹ The Q-factor is a quantity that records the total number of oscillation cycles of the resonator before its resonant oscillation decays considerably. As a result, a weaker energy dissipation leads to a higher Q-factor.

For SLMoS₂, the nanomechanical resonant behavior in SLMoS₂²⁴⁵ and few-layer MoS₂²⁴⁶ has been demonstrated by two recent experiments. Castellanos-Gomez et al. have found that the figure of merit, i.e., the frequency-Q-factor product is $f_0 * Q \approx 2 * 10^9 \text{ Hz}$ for SLMoS₂.²⁴⁵ Lee et al. have found that few-layer MoS₂ resonators exhibit a high figure of merit of $f_0 * Q \approx 2 * 10^{10} \text{ Hz}$.²⁴⁶ Such high Q-factor of SLMoS₂ can be attributed to the energy band gap in the phonon dispersion of SLMoS₂, which protects the resonant oscillations from being scattered by thermal vibrations.²⁴⁷ As a result, it has been predicted that the Q-factor of SLMoS₂ nanoresonators will be higher than that of the graphene nanoresonators by at least a factor of four.

Although it has been theoretically predicted that MoS₂ should have better mechanical resonance behavior than graphene, experiments on MoS₂ nanoresonators are very limited. More measurements are necessary to examine their properties, such as mass sensitivity. Furthermore, the sensor application of the nanoresonators depends on the level of low frequency $1/f$ noise, which is a limiting factor for the sensor sensitivity, selectivity and communication applications for MoS₂ nanoresonators.^{248,249,250,251,252,253}

3.3 Black phosphorus

3.2.5 Electronic band structure

Electronic band structure is fundamental for the electronic processes, such as the transistor performance.²¹ In particular, the value of the electronic band gap determines whether the material is an insulator (with large band gap), semiconductor (with moderate band gap), or conductor (with zero band gap).

Electrons in SLMoS₂ are normal fermions with parabolic energy dispersion, and SLMoS₂ is a semiconductor with a direct band gap above 1.8 eV.^{254,255,256} This finite band gap endorses SLMoS₂ to work as a transistor.²⁵⁷ The band gap in SLMoS₂ can be modulated by strain engineering. First-principles calculations have predicted a semiconductor-to-metal transition in SLMoS₂ using tension or biaxial compression.²⁵⁸ The experiment by Eknapakul et al. has shown that a uniaxial tensile mechanical strain of 1.5% can produce a direct-to-indirect band gap transition.²⁵⁹ With the increasing number of layers, the electronic band gap for few-layer MoS₂ undergoes a direct-to-indirect transition, and decreases to a value of 1.2 eV for bulk MoS₂.²⁶⁰

3.3 Black phosphorus

3.3.1 Structure

BP, a new 2D nanomaterial, is comprised of atomic layers of phosphorus stacked via van der Waals forces.²² BP brings a number of unique properties unavailable in other 2D crystal materials. Fig. 3.2³⁷ shows the relaxed structure of SLBP with a dimension of 17.69 * 16.74 Å via plotting with XCRYSDEN.²⁶¹ Fig. 3.2 (a) shows the perspective view that displays the puckered configuration of SLBP. In this puckered structure, each P atom is connected to three neighboring P atoms. There are two inequivalent P-P bonds in the relaxed structure, i.e. $r_{14} = 2.3827$ Å and $r_{12} = r_{13} = 2.4244$ Å, and also two inequivalent bond angles $\theta_{214} = \theta_{314} = 97.640^\circ$ and $\theta_{213} = 98.213^\circ$. The blue box in Fig. 3.2 (b) shows the unit cell with four P atoms. These two lattice constants are $a_1 = 4.1319$ Å and $a_2 = 3.6616$ Å. These structural parameters agree well with the experimental values.²⁶² The top view displayed in Fig. 3.2 (b) shows a honeycomb-like lattice structure for SLBP. Note that two edges in the honeycomb are much shorter than the other four edges. The Cartesian coordinates are set with the x-direction perpendicular to the pucker and y-direction parallel with the pucker.

3. THE FUNDAMENTAL PROPERTIES OF QUASI-TWO-DIMENSIONAL MATERIALS

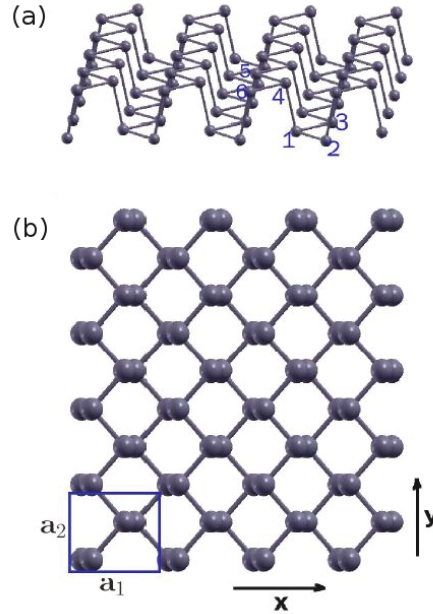


Figure 3.2: Optimized configuration of SLBP.³⁷ (a) Perspective view illustrates the pucker along the y-direction. (b) Top view of top image shows a honeycomb-like structure. The blue box represents the basic unit cell for SLBP.

3.3.2 Interatomic potential

SW potential is one of the simplest potential models, with nonlinear effects included.²⁷¹ An advanced feature of SW potential is that it keeps the numerical simulation at a quite fast level, and simultaneously includes the nonlinear effects. Thus, SW potential has been widely used in the numerical simulation community. SW potential was originally proposed by Stillinger and Weber to describe the interaction in solid and liquid forms of silicon, and it has also been used in other covalent materials such as SLMoS_2 ²²⁵ and SLBP.²⁷² As a result, in the following work about SLBP, SW potential is chosen to describe the interatomic potential.

3.3.3 Mechanical properties

Young's modulus. Previous first-principles calculations have shown that Young's modulus of SLBP is highly anisotropic and nonlinear owing to its Q2D puckered structure. More specifically, the in-plane Young's modulus is 41.3 GPa ($E^{2D} = 21.9 \text{ N } \mu\text{m}^{-1}$)

3.3 Black phosphorus

in the direction perpendicular to the pucker (i.e., in the x direction in Fig. 3.2³⁷), while 106.4 GPa ($E^{2D} = 56.3 \text{ N } \mu\text{m}^{-1}$) in the parallel direction (i.e., in the y direction Fig. 3.2³⁷), where E^{2D} is the thickness independent effective Young's modulus. It is calculated by $E^{2D} = Eh$, where the thickness of SLBP $h = 5.29 \text{ \AA}$. Other ab initio calculations have also shown that the effective Young's modulus values for the armchair and zigzag directions are $28.9 \text{ N } \mu\text{m}^{-1}$ and $101.6 \text{ N } \mu\text{m}^{-1}$ by Qiao et al,²⁷⁴ or $19.5 \text{ N } \mu\text{m}^{-1}$ and $78.0 \text{ N } \mu\text{m}^{-1}$ by Jiang et al.²⁷² The ideal ultimate strains are 0.48 and 0.11 in the perpendicular and parallel directions, respectively.

The effective Young's modulus E^{2D} is thickness independent, as a result, it is a proper quantity to compare SLBP with other layered Q2D materials. The effective Young's modulus $21.9 \text{ N } \mu\text{m}^{-1}$ in the x direction and $56.3 \text{ N } \mu\text{m}^{-1}$ in the y direction are considerably smaller than that of SLMoS₂, which is above $120.0 \text{ N } \mu\text{m}^{-1}$.^{225,234,235} The values are also one order of magnitude smaller than that of single-layer graphene, around $335.0 \text{ N } \mu\text{m}^{-1}$.^{65,173,196}

It should be note that Jiang²⁷⁵ has derived an analytic expression for the directional-dependent Young's modulus of SLBP. The Young's modulus has the minimum value in the armchair direction, but the maximum Young's modulus is not in the zigzag direction. Instead, there is a third principal (TP) direction in SLBP, with a direction angle $\phi_{tp} = 0.268\pi$, along which the Young's modulus is maximum.

Poisson's ratio. The Poisson's ratio, which is defined as $\nu_{xy} = \frac{\epsilon_y}{\epsilon_x}$, characterizes the resultant transverse strain in the y-direction for a material under longitudinal deformation in the x-direction. Typically, the Poisson's ratio is a positive number, and has a value of about 0.3 for many engineering materials (e.g. steels). In uniconstant elasticity theory,²⁷⁶ atoms are treated as point particles in a centrosymmetric lattice with only longitudinal interactions.²⁷⁷ The tensorial elastic constants of anisotropic solids are related to Cauchy relations, while Cauchy relations yield a constant value of 1/4 for the Poisson's ratio in isotropic solids.

However, uniconstant elasticity theory has not been used for many decades, and the main reason is that it was subsequently found that Poisson's ratio is not a constant value of 1/4 for all materials. Instead, in classical elasticity theory, which was found to better represent the Poisson effect and Poisson's ratio in solids, atoms are accounted for both longitudinal and transverse interactions. The Poisson's ratio in classical elasticity theory depends on the ratio between the bulk modulus K and the shear modulus μ , e.g. $\nu = \frac{1}{2}(1 - 1/(\frac{K}{\mu} + \frac{1}{3}))$ for three-dimensional isotropic materials, and it is limited to the range $0 < \nu < 0.5$ for three-dimensional isotropic materials within classical elasticity theory.

First-principles calculations have investigated the Poisson's ration of SLBP.¹⁷⁷ It

3. THE FUNDAMENTAL PROPERTIES OF QUASI-TWO-DIMENSIONAL MATERIALS

is found that the linear Poisson's ratio is highly anisotropic in SLBP. More specifically, the linear Poisson's ratios are 0.93 and 0.40, in the y direction and x direction, respectively. It means that SLBP will contract (expand) in the other two lateral directions, when it is stretched (compressed) in the x or y direction. As a direct result of the anisotropic puckered structure of SLBP, the linear Poisson's ratio is negative, i.e. $\nu = -0.027$, in the out-of-plane direction (the z-direction) during its deformation in the y direction. That means SLBP expands (contracts) in the z-direction when it is stretched (compressed) in the y-direction. This occurs because that when the structure is stretched in the y direction, it undergoes a large contraction along the x direction due to the large value of ν_{yx} , leading to the decrease of inter-group angles such as \angle_{146} (as shown in Fig. 3.2³⁷). That is, the inter-group bond 1-4 will be aligned closer to the z-axis, as a result, there is the expansion of the thickness in the z direction. Interestingly, the pucker can also be regarded as two coupling hinges formed by the \angle_{546} and \angle_{214} , which leads to a nanoscale version of the coupling hinge mechanism. The negative Poisson's ratio is thus closely related to the condition of $\angle_{146} > 90^\circ$ in BP.¹⁷⁷

While the negative Poisson's ratio of BP in the z direction was discussed in detail in previous study,¹⁷⁷ this effect has been mentioned in other works, which applied mechanical strains to BP. For instance, the negative Poisson's ratio has also been observed during the investigation of strain effects on the electronic properties of SLBP²⁷⁸ or the thermoelectric properties for bulk BP.²⁷⁹

3.3.4 Nanomechanical resonators

While most existing experiments have been focused on potential electronic applications of BP,^{27,28,29} a recent experiment showed that the resonant vibration response of BPR can be achieved at a very high frequency.³⁰ However, there have been no theoretical studies on the intrinsic dissipation in BPRs to-date. Very recently, Feng's group has examined the BPR experimentally.⁴³ However, the experimental BPR samples should have some unavoidable vacancy defects or oxidation.⁴³ Furthermore, these defects can have strong effects on the performance of resonant oscillation of the nanomechanical resonators. An important task is thus to examine the effects of the vacancy defect and oxidation on BPRs.

3.3.5 Electronic band structure

Recently, few-layer BP has been explored as an alternative electronic material to boron nitride, graphene and the transition metal dichalcogenides for transistor applications.

3.4 Graphene

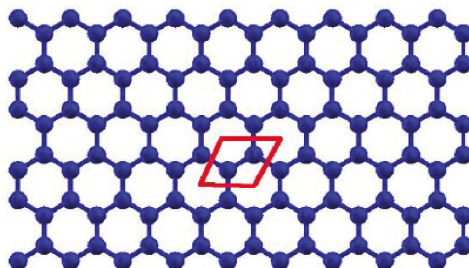


Figure 3.3: Top view of the structure of graphene. The red rhombus encloses the unit cell. The lattice constant is $a = 2.46 \text{ \AA}$ and the bond length is $b = 1.42 \text{ \AA}$.

^{45,280,281} This is because BP has a direct bandgap that can be manipulated via mechanical strain and thickness,^{39,45,282,283} and exhibits a large optical conductivity and a high carrier mobility.⁴⁵ Specifically, first-principles calculations have shown that SLBP has a band gap about 0.8 eV, and the band gap decreases with increasing thickness.^{23,45} It has been shown that, comparing with the band gap of SLBP (0.75 eV), the small band gap of bulk BP (0.19 eV) is partly because of the interlayer Van der Waals interaction in BP. It should be note that, the band gap for SLBP can be manipulated by mechanical strain in the direction normal to the BP plane, where a semiconductor-metal transition was observed.²⁴

3.4 Graphene

3.4.1 Structure and interatomic potential

As shown in Fig. 3.3, graphene has a honeycomb lattice structure with a D_{6h} point group. There are two inequivalent carbon atoms in the unit cell. These two carbon atoms are reflected onto each other by the inverse symmetry operation from the D_{6h} point group. The lattice constant is $a = 2.46 \text{ \AA}$ and the C-C bond length is $b = a/\sqrt{3} = 1.42 \text{ \AA}$.¹⁸⁶

The interactions among the carbon atoms in graphene can be calculated using four different computation cost levels. The first-principles technique is the most expensive approach to compute the interatomic potential. Many existing simulation packages can be used for these calculations, including the freely available Spanish Initiative for Electronic Simulations with Thousands of Atoms (SIESTA) package¹⁸⁷ and the commercial Vienna Ab-initio Simulation Package (VASP).¹⁸⁸ To save computation cost,

3. THE FUNDAMENTAL PROPERTIES OF QUASI-TWO-DIMENSIONAL MATERIALS

Brenner et al. have developed an empirical potential for carbon-based materials, including graphene.¹²⁷ The Brenner potential takes the form of the bond-order Tersoff potential¹⁸⁹ and is able to capture most of the linear properties and many of the non-linear properties of graphene. For example, the Brenner potential can describe the formation and breakage of the C-C bonds in graphene, providing a good description for its structural, thermal and mechanical properties. The SW potential^{190,191} or the Tersoff potential¹⁸⁹ provides reasonable predictions for some of the linear and nonlinear properties of graphene. These two empirical potentials are computationally faster than Brenner potential since they have fewer parameters than Brenner potential. Finally, the linear part of the C-C bond interactions can be captured using VFF models,¹⁹² which have the most inexpensive computation costs.

3.4.2 Mechanical properties

Young's modulus. The mechanical properties for graphene have been extensively investigated.^{193,194,195} For Young's modulus, the thickness was chosen to be 3.35 Å, which is half of the lattice constant in the bulk graphite. Nanoindentation experiments measured the effective Young's modulus of graphene to be around $335.0 \text{ N } \mu\text{m}^{-1}$.¹⁷³ This value could be reproduced using a simple method, in which the nonlinear interactions are estimated from the Tersoff-Brenner potential.¹⁹⁶

Yield stress. Lee et al. measured the yield stress to be $420.4 \text{ N } \mu\text{m}^{-1}$.¹⁷³ Moreover, the yield stresses obtained with the continuum elasticity theory were $44.4 \text{ N } \mu\text{m}^{-1}$ using the Brenner potential,¹⁹⁷ and $42.4 \text{ N } \mu\text{m}^{-1}$ using a tight-binding atomistic model.¹⁹⁸ While the elasticity continuum simulation gave an isotropic value for the yield stress in graphene, microscopic atomic models have predicted the yield stress to be chirality dependent in graphene. First-principles calculations have predicted the yield stress to be $36.9 \text{ N } \mu\text{m}^{-1}$ in the armchair direction and $40.5 \text{ N } \mu\text{m}^{-1}$ in the zigzag direction.¹⁹³ Molecular mechanics simulations provided a yield stress of $30.2 \text{ N } \mu\text{m}^{-1}$ in the armchair direction and $36.9 \text{ N } \mu\text{m}^{-1}$ in the zigzag direction in graphene.¹⁹⁹ Both of the two atomic models have shown that graphene has a smaller yield stress in the armchair direction than in the zigzag direction. Note that here we retain the definition from the previous reference,¹⁹⁹ where the armchair direction is along the direction of the carbon-carbon bonds.¹⁹³

Bending modulus. Graphene is extremely soft in the out-of-plane direction, owing to its one-atom-thick structure.^{200,201,202,203} Graphene is so soft that it has an extremely small bending modulus, which can be explained by the well-known relationship in the shell theorem, $D = E^{2D}h^2/(12(1 - \nu^2))$, with h as the thickness and ν as Poisson's ratio. The bending modulus has been derived analytically from two equivalent ap-

3.4 Graphene

proaches; it was 1.4 eV from the exponential Cauchy-Born rule using the Brenner potential,^{175,176} and 1.17 eV using the geometric approach with the interactions described by the VFF models.¹⁷⁴ Note that these two approaches are equivalent to each other and the difference in the bending modulus mainly comes from the different potentials used in these two studies.²¹

Buckling phenomenon. For graphene, the values of $E^{2D} = 335.0 \text{ N m}^{-1}$ and $D = 1.4 \text{ eV}$, described above, give the explicit formula for the buckling critical strain as:

$$\epsilon_c = \frac{2.64}{L^2}, \quad (3.5)$$

with the units of length (L) as Å. For samples with the same lengths, the buckling critical strain for SLMoS₂ is about twenty times larger than that for graphene. That means, it is difficult to buckle SLMoS₂ under external compression. This phenomenon has been investigated with both phonon analysis and MD simulations.^{243,244}

We have discussed the basic mechanical properties of graphene and SLMoS₂. Graphene has a larger Young's modulus and yield stress, and is more flexible than SLMoS₂. However, SLMoS₂ has a higher bending modulus and does not buckle as readily under external compression as graphene. Hence, in terms of the mechanical properties, it should be more advantageous for SLMoS₂ and graphene to be used together in a heterostructure to mitigate the negative mechanical properties of each constituent.

3.4.3 Nanomechanical resonators

For graphene nanoresonators, the Q-factor increases exponentially with decreasing temperatures,^{211,212} $T^{-\alpha}$. Zande et al.²¹¹ have found that the exponent $\alpha = 2.3 \pm 0.1$ for temperatures above 40 K, and $\alpha = 0.35 \pm 0.05$ for temperatures below 40 K. Chen et al.²¹² have also observed a similar transition in the Q-factor. This continuous transition for the temperature dependence of the Q-factor is attributed to the diffusion of adsorbs in the out-of-plane direction on the surface of the graphene layer.^{213,214} MD simulations have also predicted a discontinuous transition in the Q-factor at the low temperature of 7.0 K, which is caused by the in-plane diffusion of adsorbs on the graphene surface.²¹³ Graphene nanoresonators with very high Q-factors have been obtained in the laboratory at very low temperatures. Bunch et al. observed a Q-factor of 9000 for a graphene nanoresonator at 10 K.²¹¹ Chen et al. also found that the Q-factor increased with the decreasing temperature, reaching 10^4 at 5 K.²¹² Eichler et al. found that the Q-factor reached 10^5 at 90 mK.²¹⁵

3. THE FUNDAMENTAL PROPERTIES OF QUASI-TWO-DIMENSIONAL MATERIALS

3.4.4 Electronic band structure

Graphene exists nice electronic properties.²¹⁶ The electronic energy dispersion is linear near the Brillouin zone corner. The velocity of this Dirac fermion is at $1/300$ the speed of light.^{217,218} The Dirac fermion was found to be closely related to the mirror plane symmetry in the AB-stacked few-layer graphene; i.e. Dirac fermions exist in AB-stacked few-layer graphene with an odd number of layers, and the electronic spectrum becomes parabolic in AB-stacked few-layer graphene with an even number of layers.²¹⁹ Interestingly, Dirac fermions are present again in twisted bilayer graphene²²⁰ due to the effective decoupling of the two graphene layers by the twisting defect; i.e., the mirror plane symmetry is effectively recovered in the twisted bilayer graphene. The Dirac cone at the Brillouin zone corner has a zero band gap in graphene, which is mainly contributed by free π electrons.²²¹ For electronic devices, like transistors, a finite band gap is desirable, and various techniques have been invented to open an electronic band gap in graphene.²¹ The strain engineering has been used to generate a finite band gap of 0.1 eV with a 24% uniaxial strain.²²² Guinea et al. have applied triangular symmetric strains to generate a band gap over 0.1 eV, which is observable at room temperature.²²³ A finite band gap can also be opened by confining the graphene structure in a nanoribbon form, where the band gap increases with decreasing ribbon width.²²⁴ Comparing with graphene, SLMoS₂ possesses a finite band gap prior to any gap-opening engineering. As a result, SLMoS₂ may be more competitive than graphene for applications in transistors, energy harvesting, optoelectronics, and other nano-material fields.

Chapter 4

Self-actuated Breathing-like Oscillation

4.1 Introduction

2D crystal materials have attracted lots of attention due to that, comparing with 1D crystal materials, they are relatively easier for fabricating complex configurations. Graphene is one of the most widely known and studied 2D crystal materials³⁴⁰ because of its exceptional electronic, mechanical, and chemical properties.^{173,341,342} However, pristine graphene is well-known without bandgap,²¹⁷ a property that is essential for many applications, including transistors. In contrast, MoS₂ is a semiconductor with a bulk bandgap above 1.2 eV,³²⁰ which can be further manipulated by reducing its thickness to monolayer, 2D form, with a band gap of 1.8 eV.³²¹ This finite bandgap is a key reason for the excitement surrounding MoS₂ as compared with graphene.³²² Because of its direct bandgap and also its well-known properties as a lubricant, MoS₂ has attracted considerable attention in recent years.^{323,324} For example, Radisavljevic et al.³²⁵ demonstrated the application of SLMoS₂ as a transistor, which has a large mobility above 200 cm²V⁻¹s⁻¹. Several recent works have addressed the thermal transport properties of SLMoS₂ in both the ballistic and diffusive transport regimes.^{80,326,327,328} For example, the thermal conductivity for the MoS₂ nanoribbon is found to be about 673.6 Wm⁻¹K⁻¹ in the armchair nanoribbon, and 841.1 Wm⁻¹K⁻¹ in the zigzag nanoribbon at room temperature.³⁴⁷ Meanwhile, the mechanical properties of the SLMoS₂ recently have also been investigated experimentally.^{234,235,350}

For theoretical investigations of SLMoS₂, first-principles technique is the most accurate approach, due to its ability to provide quantum mechanically-based predictions

4. SELF-ACTUATED BREATHING-LIKE OSCILLATION

for various properties of SLMoS₂. However, it is well-known that first principles techniques cannot simulate more than around a few thousand atoms, which poses serious limitations for comparisons with experimental studies, which typically occur on the micrometer length scale. For such larger sizes, classical MD simulations are desirable, which require interatomic potentials. Several atomic potentials have been proposed for MoS₂ and SLMoS₂, including the VFF model,⁷⁸ the Brenner-like atomic potential,⁷⁹ and the SW atomic potential.⁸⁰

Besides these atomic potentials, the CG model is another useful potential to support simulations for even larger system sizes. The CG model simplifies the atomic system by introducing CG beads, and the atomic interaction is replaced by CG potentials. CG models have been used to simulate quasi-one-dimensional nanostructures.^{81,82,83} The CG model has also achieved great success in biophysics.^{84,85} We will present the parametrization of the CG potential for SLMoS₂ in this chapter.

Another topic of this chapter is about a particular type of resonant oscillation in the folded MoS₂. Very recently, two experimental groups have demonstrated the nanomechanical resonant behavior for SLMoS₂³³² or few-layer MoS₂.³³³ A recent work³³⁴ has also examined the intrinsic energy dissipation in MoS₂ nanoresonators. While all of these works on MoS₂ nanoresonators are for planar MoS₂ sheets, the folded MoS₂ is an interesting structure with important van der Waals effects coming from the folding configuration.

In this chapter, we parametrize two kinds of CG models to describe the properties of SLMoS₂, i.e. 2D CG model and 1D CG model.

2D CG model. For the 2D CG model, SW potential is used to describe the interbead potentials. All SW geometrical parameters are determined according to the equilibrium condition for each potential term, while the SW energy parameters are derived analytically based on the VFF model. As an application sample, we investigate the adsorption effects on the resonant frequency of the nanoresonator. We find that the resonant frequency is insensitive to the adsorbed mass.

The uniqueness of our 2D CG model of SLMoS₂ is twofold. First, it is a bottom-up method, starting from the atomic structure of SLMoS₂, and scalable to any orders of CG levels. Therefore, such 2D CG model can be tailored to be suitable to simulate SLMoS₂ systems of a wide range of length scales. Second, the hexagonal lattice symmetry is maintained in all orders of CG levels. This feature maximizes the intrinsic similarity between the 2D CG model and atomic structure of SLMoS₂, the key to fidelity and precision of the CG simulations.

1D CG model. We further simplify SLMoS₂ to 1D CG model, where all potential parameters for the 1D CG model are determined analytically from the SW potential for

4.2 2D CG model development

the SLMoS₂ atomic structure. As an application sample, we apply the 1D CG model to investigate the breathing-like resonant oscillation in the folded SLMoS₂. We find that such resonant oscillation is self-actuated, as this breathing-like oscillation can be actuated by intrinsic thermal vibrations without external actuation. Furthermore, we disclose an interesting phenomenon that the resonant frequency for the breathing-like oscillation is insensitive to adsorption effect, owing to the peculiar structure of the folded SLMoS₂.

The uniqueness of our 1D CG simulation is twofold. First, it can support simulations for even larger system sizes to compare with the experimental studies. Second, it is able to provide some nice analytic predictions for MoS₂, though we ignore some effects, such as Poisson's ratio.

The outline of this chapter is as follows. In Sec. 4.2, the 2D CG model is parametrized. Sec. 4.3 is dedicated to the development of 1D CG model. This chapter ends with brief comparison of 2D CG model with 1D CG model in Sec. 4.4.

4.2 2D CG model development

Previous work³⁵³ has performed MD simulations for SLMoS₂ using the SW potential to investigate the mechanical properties. The atomic potential model is accurate, and should can be used to simulate properties on macroscopic level. However, for SLMoS₂ with such larger size, the atomic potential model should be computationally expensive. To this aim, a 2D CG model is proposed. In our 2D CG model, the structure of SLMoS₂ is simplified by CG beads, with the hexagonal lattice symmetry maintained, and the parametrization of SW potential is based on VFF model.

This section is recognized as follows. In Sec. 4.2.1, the 2D CG model is parametrized analytically from the atomic structure and the SW potential is parametrized based on the VFF model. In Sec. 4.2.2, we use the 2D CG model to investigate the mechanical properties and the adsorption effects on the resonant frequency. Sec. 4.2.3 presents a simple conclusion.

4. SELF-ACTUATED BREATHING-LIKE OSCILLATION

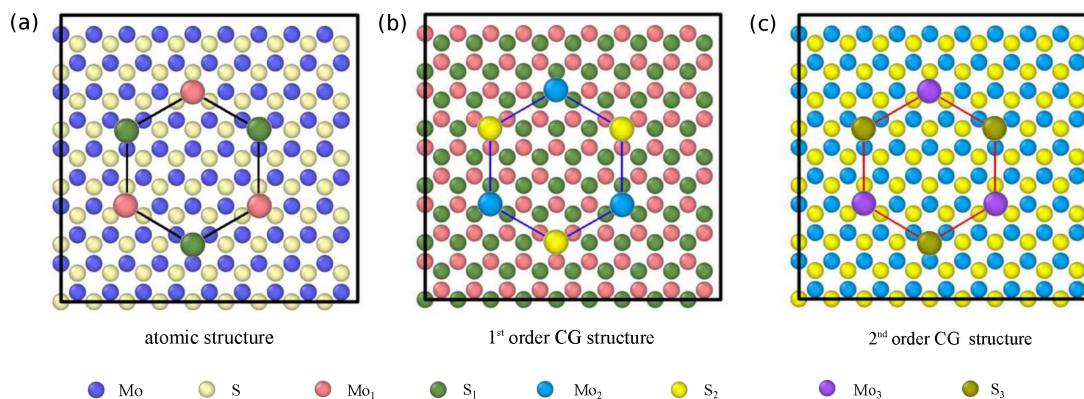


Figure 4.1: The top view of a bottom-up scalable 2D CG simulation scheme of SLMoS₂. Mapping from atomic SLMoS₂ in (a), to 1st and 2nd order 2D CG models in (b) and (c), respectively. The hexagonal lattice symmetry is maintained in all CG structures of any levels, and the positions of Mo_{*i*} beads and S_{*i*} beads in the 2D CG model are the same as Mo atoms and S atoms, respectively, in the original atomic SLMoS₂. Note that the 2D CG model is applied to “in-plane” (projection of all atoms onto one plane) only, with out-of-plane direction unchanged.

4.2.1 Parametrization of SW potential of 2D CG model based on VFF model

4.2.1.1 2D CG model

There are three major ingredients in the 2D CG model; i.e., bead structure, bead mass and inter-bead potential.

Bead structure

Fig. 4.1 shows the representations of the first two orders CG structures. As shown in Fig. 4.1 (a), three Mo₁ beads and three S₁ beads, as the apexes of the hexagonal lattice (black lines), represent all the atoms (Mo and S) within the hexagonal lattice in the atomic structure. More specifically, three Mo₁ beads represent all Mo atoms within the hexagonal lattice and three S₁ beads represent all S atoms. It means that one Mo₁ bead and one S₁ bead represent 16 Mo atoms and 16 S atoms, respectively. The side length of the hexagonal e₁ corresponds to the projection length of Mo₁-S₁ bond, i.e. 7.2 Å, 4 times as the projection length of the original Mo-S bond e₀ (1.8 Å). Similarly, Fig. 4.1 (b) shows one Mo₂ bead represents 16 Mo₁ beads and one S₂ bead represents

4.2 2D CG model development

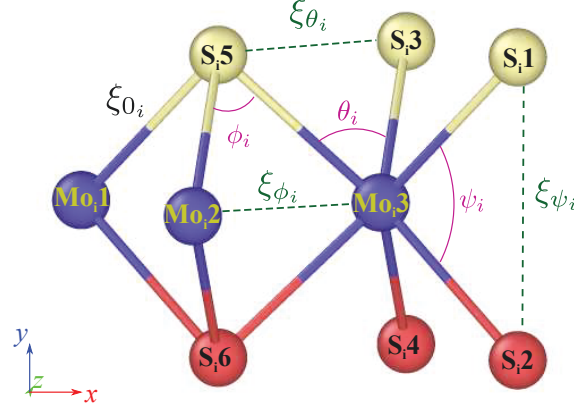


Figure 4.2: Configuration of i th order 2D CG model. There are total four kinds of bonds; i.e., one kind of real bond (ξ_{0i}) and three kinds of virtual bonds (ξ_{θ_i} , ξ_{ψ_i} and ξ_{ϕ_i}). The x -axis is in the armchair direction, and the y -axis is in the zigzag direction.

16 S_1 beads, with $e_2 = 4^2 e_0$. Such a CG procedure can be scaled up recursively (i.e., Fig. 4.1 (c)) to any higher order, while the hexagonal lattice symmetry is maintained in all the CG structures of any level, with

$$e_i = 4^i e_0. \quad (4.1)$$

According to the geometric relationship between the 2D CG structure and the SLMoS_2 atomic structure, we can get some geometric parameters for the 2D CG model. As shown in Fig. 4.2, all Mo_i beads are on the same plane. Beads S_{i1} , S_{i3} , and S_{i5} are on the same layer, and the other three S_i beads are on the other layer. We denote S_i beads sitting in the two planes as S_i° . The Mo_i layer is sandwiched by two S_i layers. The space between the two S_i layers is

$$2d_i = 2d_0 = 2 * 1.558 \text{ \AA}, \quad (4.2)$$

as a constant for all orders of 2D CG model. The distance between two first-nearest-neighbor Mo_i and S_i beads is

$$b_i = \sqrt{e_i^2 + d_i^2}. \quad (4.3)$$

There are three types of bond angles, i.e., $\theta_i = \angle S_{i3} \text{Mo}_i S_{i5}$, $\psi_i = \angle S_{i1} \text{Mo}_i S_{i2}$ and

4. SELF-ACTUATED BREATHING-LIKE OSCILLATION

Table 4.1: Structure parameters for atomic SLMoS₂ (i.e. 0th order²²⁵) and 1st order 2D CG model.

order	$d_i(\text{\AA})$	$b_i(\text{\AA})$	$e_i(\text{\AA})$	$\theta_i(^{\circ})$	$\psi_i(^{\circ})$	$\phi_i(^{\circ})$
0	1.558	2.38	1.80	81.787	81.787	81.787
1st	1.558	7.367	7.20	115.652	24.4198	115.652

$\phi_i = \angle Mo_i 3S_i 5Mo_i 2$. According to the geometric relationship, we have

$$\theta_i = \phi_i = 2 * \arcsin\left(\frac{\frac{\sqrt{3}}{2}e_i}{\sqrt{e_i^2 + d_i^2}}\right), \quad (4.4)$$

and

$$\psi_i = 2 * \arctan\left(\frac{d_i}{e_i}\right). \quad (4.5)$$

Table. 4.1 lists the structure parameters for atomic SLMoS₂ and the 1st order 2D CG model.

Mass of beads

As shown in Fig. 4.1, one Mo_{*i*} bead in the *i*th order 2D CG model represents 16^{*i*} Mo atoms in the SLMoS₂ atomic structure, and similarly, one S_{*i*} bead represents 16^{*i*} S atoms in the atomic MoS₂. As a result, the masses of Mo_{*i*} bead and S_{*i*} bead in the *i*th order 2D CG model are $m_{Mo_i} = 16^i * m_{Mo_0}$ and $m_{S_i} = 16^i * m_{S_0}$, respectively, with m_{Mo_0} and m_{S_0} as the masses of Mo and S atoms, respectively.

Inter-bead potential

In the 2D CG model, the bending energy with respect to the variation of angles is equivalent to the stretching energy corresponding to the variation of virtual bonds. More specifically, as shown in Fig. 4.2, the bending energy associating with the variation of angles θ_i , ψ_i and ϕ_i is equivalent to the stretching energy with respect to the variation of virtual bonds ξ_{θ_i} , ξ_{ψ_i} and ξ_{ϕ_i} , respectively. As a result, there are two major interactions among beads,

$$V = V_L + V_{weak}, \quad (4.6)$$

4.2 2D CG model development

where V_L is the potential that captures a variation in the inter-bead distance ξ and V_{weak} is the non-bonded van der Walls interaction. The detailed expressions for these two potentials are demonstrated in the following.

(1). The stretching energy is,

$$V_L = \frac{1}{2}K_\xi (\Delta \xi)^2, \quad (4.7)$$

where K_ξ is the 2D CG parameter corresponding to bond stretching, which will be determined in the next subsection. $\Delta \xi$ is the variation in the inter-bead distance. In the 2D CG model, there are one kind real bond (ξ_{0_i}) and three kinds virtual bonds (ξ_{θ_i} , ξ_{ψ_i} and ξ_{ϕ_i}), as shown in Fig. 4.2. The total stretching energy in the 2D CG model is the collection of the stretching energy of the four kinds bonds.

(2). The weak non-bonding van der Walls interaction between two beads is described by the following LJ potential,

$$V_{LJ} = 4\varepsilon \left[\left(\frac{\sigma}{r} \right)^{12} - \left(\frac{\sigma}{r} \right)^6 \right], \quad (4.8)$$

where ε is the energy parameter describing the well depth of the potential, and σ is a length parameter corresponding to the zero potential distance. The total weak non-bonding energy in the CG bead model can be calculated by summarizing LJ potential between all bead pairs in the 2D CG model.

4.2.1.2 Parametrization of SW potential

We have presented some general potential information for our 2D CG model in the previous subsection and will determine all the potential parameters in the following.

Tensile parameter

There are total four tensile parameters, i.e., $K_{\xi_0}^i$, associated with the real bond ξ_{0_i} ; $K_{\xi_\theta}^i$, with respect to virtual bond ξ_{θ_i} ; $K_{\xi_\psi}^i$ and $K_{\xi_\phi}^i$ are corresponding to virtual bonds ξ_{ψ_i} and ξ_{ϕ_i} , respectively, as shown in Fig. 4.2.

As an important requirement of the 2D CG model development, the 2D CG model should have the same tensile properties as the original atomic SLMoS₂ structure. That means the stretching energy in both systems should be the same if these two systems are deformed by the same amount of strain (ε) (expand, with no change for the angle energy). We will derive all 2D CG tensile parameters in the following.

4. SELF-ACTUATED BREATHING-LIKE OSCILLATION

We consider $K_{\xi_0}^i$ firstly. We assume the number of bonds ξ_{0i} in the i th order 2D CG model is NN . One bond ξ_{0i} represents $16^i \xi_{00}$ in the atomic SLMoS₂.

The total strain energy stored in the deformed original atomic SLMoS₂ by strain ε is

$$V_{\xi_0}^0 = 16^i * NN * \frac{1}{2} K_{\xi_0}^0 (\varepsilon * b_0)^2. \quad (4.9)$$

The strain energy in the deformed i th order 2D CG model by strain ε is

$$V_{\xi_0}^i = NN * \frac{1}{2} K_{\xi_0}^i (\varepsilon * b_i)^2. \quad (4.10)$$

By equating the stretching energy in the atomic SLMoS₂ and the i th order 2D CG model, we have the analytic expression for the stretching parameter in the i th order 2D CG model,

$$K_{\xi_0}^i = \frac{16^i K_{\xi_0}^0 (b_0)^2}{b_i^2}. \quad (4.11)$$

Similarly, we can obtain

$$K_{\xi_\theta}^i = K_{\xi_\theta}^0, \quad (4.12)$$

$$K_{\xi_\phi}^i = K_{\xi_\phi}^0 \quad (4.13)$$

and

$$K_{\xi_\psi}^i = 16^i * K_{\xi_\psi}^0. \quad (4.14)$$

However, $K_{\xi_0}^0$, $K_{\xi_\theta}^0$, $K_{\xi_\phi}^0$ and $K_{\xi_\psi}^0$ are all unknown. Following we will determine all these values based on VFF model.

The VFF model²²⁷ for atomic SLMoS₂ is able to describe the phonon spectrum and the sound velocity accurately. Table. 4.2 lists the first four leading force constants for SLMoS₂, neglecting other weak interaction terms. The bond stretching term is $V_{\xi_0}^0 = \frac{1}{2} K_{\xi_0}^0 (\Delta \xi_{00})^2$, with $\Delta \xi_{00}$ as the length variation of Mo-S bond (eg. Mo₀₃-S₀₁). The angle bending terms are $V_\theta^0 = \frac{1}{2} K_\theta^0 b_0^2 (\Delta \theta_0)^2$ for the variation $\Delta \theta_0$ of angle θ_0 (i.e. $\angle S_0^+ Mo_0 S_0^+$ or $\angle S_0 Mo_0 S_0$), $V_\psi^0 = \frac{1}{2} K_\psi^0 b_0^2 (\Delta \psi_0)^2$ for the variation $\Delta \psi_0$ of angle

4.2 2D CG model development

Table 4.2: The VFF model parameters²²⁷ for atomic SLMoS₂.

$K_{\xi_0}^0 \left(\frac{eV}{A^2} \right)$	$K_{\theta}^0 \left(\frac{eV}{A^2} \right)$	$K_{\psi}^0 \left(\frac{eV}{A^2} \right)$	$K_{\phi}^0 \left(\frac{eV}{A^2} \right)$
8.640	0.937	0.862	1.18

ψ_0 (i.e. $\angle S_0^+ Mo_0 S_0$) and $V_{\phi}^0 = \frac{1}{2} K_{\phi}^0 b_0^2 (\phi)^2$ for the variation ϕ of angle ϕ_0 (i.e. $Mo_0 S_0 Mo_0$).

The tensile parameters ($K_{\xi_{\theta}}^0$, $K_{\xi_{\phi}}^0$ and $K_{\xi_{\psi}}^0$), associated with the virtual bonds (ξ_{θ_0} , ξ_{ψ_0} and ξ_{ϕ_0}), are determined by equating the bending potential to the tensile potential.

Take $K_{\xi_{\theta}}^0$ for example, the bending energy with respect to the angle variation of angle θ_0 is,

$$V_{\theta}^0 = \frac{1}{2} K_{\theta}^0 b_0^2 (\theta)^2. \quad (4.15)$$

This bending behavior can be equated to the tensile behavior, associated with virtual bond ξ_{θ_0} , and the equivalent tensile potential is,

$$V_{\xi_{\theta}}^0 = \frac{1}{2} K_{\xi_{\theta}}^0 (\xi_{\theta_0})^2. \quad (4.16)$$

By equating the bending potential and the equivalent tensile potential, we obtain the analytic expression for the tensile parameter $K_{\xi_{\theta}}^0$ in the atomic SLMoS₂,

$$K_{\xi_{\theta}}^0 = \frac{K_{\theta}^0 3e_0^2}{b_0^2 (\sin(\theta_0))^2}. \quad (4.17)$$

Similarly, we have

$$K_{\xi_{\psi}}^0 = \frac{K_{\psi}^0 * 4d_0^2}{b_0^2 (\sin(\psi_0))^2}, \quad (4.18)$$

and

$$K_{\xi_{\phi}}^0 = \frac{K_{\phi}^0 3e_0^2}{b_0^2 (\sin(\phi_0))^2}. \quad (4.19)$$

Now, all the tensile parameters are known already. Table. 4.3 lists tensile parameters for the atomic SLMoS₂ and the 1st order 2D CG model.

4. SELF-ACTUATED BREATHING-LIKE OSCILLATION

Table 4.3: Tensile parameters for the atomic SLMoS₂ and the 1st order 2D CG model.

order	$K_{\xi_0}^i (\frac{eV}{\text{\AA}^2})$	$K_{\xi_\theta}^i (\frac{eV}{\text{\AA}^2})$	$K_{\xi_\psi}^i (\frac{eV}{\text{\AA}^2})$	$K_{\xi_\phi}^i (\frac{eV}{\text{\AA}^2})$
0	8.640	1.641	1.508	2.067
1st	14.43	1.641	24.134	2.067

LJ parameters

In the 2D CG model for SLMoS₂, the van der Walls interaction exists between all bead pairs. For two CG beads from the same 2D CG model layer, the interaction is dominated by the stretching energy, so the weak van der Walls interaction can be ignored. For two beads from two different 2D CG model layers, the van der Walls potential is the only interaction, and dominates the inter-layer coupling between two layers for the 2D CG model. We thus determine the LJ parameters in the 2D CG model by considering the van der Walls interaction between two neighboring CG layers.

As shown in Fig.4.3 (a), the most stable configuration for two neighboring CG layers is analogous to atomic bilayer MoS₂, in which one type (S or Mo) of atom in the top layer is on top of another type of atom in the bottom layer. The length parameter σ in the LJ potential is determined by keeping the equilibrium distance $/D$ between two CG layers the same as the interlayer equilibrium space between two atomic MoS₂ layers. The LJ interaction is the dominant inter-layer potential, so the distance between two inter-layer first-nearest-neighboring beads actually corresponds to the minimum energy distance, $2^{\frac{1}{6}}\sigma$. Specifically, as shown in Fig. 4.3 (b), every S_i^+ bead in the bottom CG layer interacts with 3 first-nearest-neighboring S_i^- beads in the top CG layer via van der Walls, and the distance should be $2^{\frac{1}{6}}\sigma$.

According to geometric relationship, we have

$$\sigma = 2^{\frac{1}{6}} \sqrt{(\frac{/D}{2} - d_0)^2 + (\frac{e_i}{2})^2 + (-\frac{\sqrt{3}e_i}{2})^2}, \quad (4.20)$$

with $/D = 6.17\text{\AA}$.³⁵³

The other parameter in the LJ potential in the 2D CG model is the energy parameter ϵ . The energy parameter is determined by equating the cohesive energy between two neighboring CG layers and the cohesive energy between two atomic MoS₂ layers. In our previous work,³⁵³ we have obtained the cohesive energy for two atomic MoS₂ layers as $A * E_c$, where $A = 27.0\text{\AA} * 28.0\text{\AA}$ is the area of the MoS₂ layer and $E_c = 14.44 \frac{meV}{\text{\AA}^2}$ is the cohesive energy density for the atomic MoS₂.

4.2 2D CG model development

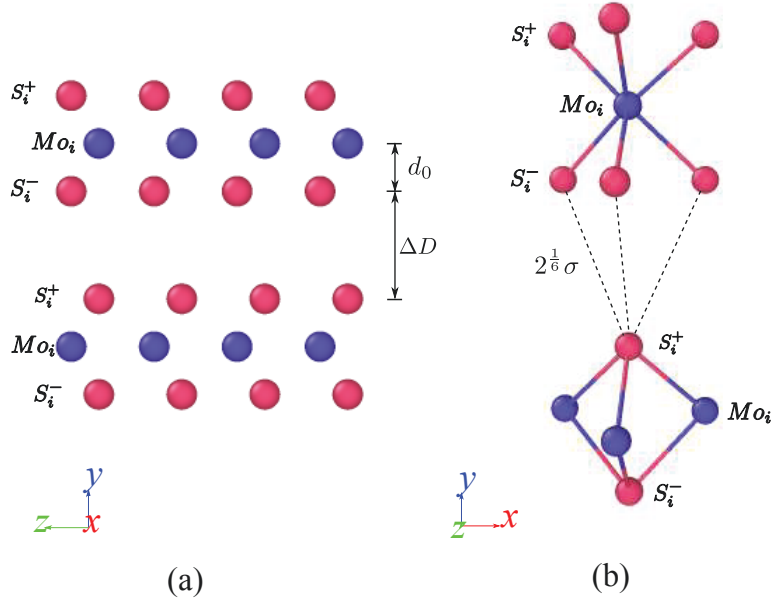


Figure 4.3: Two neighboring CG layers with the side view in (a) and perspective view in (b).

Two neighboring CG layers are interacted by S_i beads in two different CG layers. It is assumed that the inter-layer coupling in the 2D CG model is contributed by LJ potential between two first-nearest-neighboring S_i beads. That means every S_i bead in the top CG layer interacts with 3 S_i^+ beads in the bottom layer. Under this approximation, the cohesive energy between the two neighboring CG layers is $3M\varepsilon$, where M is the number of S_i beads in the top CG layer.

As a result, the energy parameter ε for i th 2D CG model can be obtained as

$$\varepsilon = \frac{A^* E_c}{3M} = 40.43 * 16^i, \quad (4.21)$$

with $M = \frac{90}{16^i}$, where 90 is the number of S atoms in the top layer of atomic bilayer MoS_2 with area A .

Parametrization of SW potential based on VFF model

The SW potential form keeps unchanged for different materials, but all parameters

4. SELF-ACTUATED BREATHING-LIKE OSCILLATION

need to be determined properly. Jiang²⁶³ has proposed to parametrize the SW potential for covalent materials starting from the VFF model, and applied the parametrization procedure to develop the SW potential for atomic SLMoS₂ and BP. We will use this procedure to develop the SW potential for the 2D CG model in the following.

The two-body potential expression is

$$V_2 = \varepsilon A (B\sigma^p r_{ij}^p - \sigma^q r_{ij}^q) e^{[\sigma(r_{ij} - \alpha\sigma)^{-1}]} \quad (4.22)$$

The cut-offs $\alpha\sigma = 1.327b_i$ is geometrically determined by the CG structure. There are two unknown geometrical parameters, i.e. σ and B , and one energy parameter A .

First of all, it is reasonable to require that all bonds are at their equilibrium lengths in the equilibrium configuration. That is, we have the equilibrium condition, $\frac{\partial V_2}{\partial r_{ij}} \big|_{r_{ij}=b_i} = 0$ for each bond. Thus we obtain the following constraint for parameters σ and B in V_2 ,

$$B = \frac{b_i^5}{\sigma^4 b_i + 4\sigma^3 (b_i - \alpha\sigma)^2} \quad (4.23)$$

where b_i is the equilibrium bond length. In other words, Eq. (4.23) ensures that, in the equilibrium configuration, the bond has an equilibrium length of b_i and the interaction V_2 for this bond is at the energy minimum state.

The energy parameter A in the SW potential can be derived from the VFF model, by equating the force constants from SW potential and the force constants in the VFF model. More specifically, we have $\frac{\partial^2 V_2}{\partial r_{ij}^2} \big|_{r_{ij}=b_i} = K_\xi$ at the equilibrium structure, leading to,

$$A = \frac{K_\xi}{\beta e^{[\sigma/(b_i - \alpha\sigma)]}} \quad (4.24)$$

where the coefficient β in Eq. (4.24) is,

$$\begin{aligned} \beta = & \left[\frac{\sigma}{(b_i - \alpha\sigma)^2} \right]^2 (B\sigma^4/b_i^4 - 1) \\ & + \left[\frac{2\sigma}{(b_i - \alpha\sigma)^3} \right] (B\sigma^4/b_i^4 - 1) \\ & + \left[\frac{\sigma}{(b_i - \alpha\sigma)^2} \right] (8B\sigma^4/b_i^5) \\ & + (20B\sigma^4/b_i^6). \end{aligned} \quad (4.25)$$

As a result, the energy parameter A in the SW potential is analytically related to the energy parameters in the VFF model.

4.2 2D CG model development

Table 4.4: SW potential parameters for the 0th order 2D CG model for SLMoS₂ (i.e. atomic SLMoS₂) used by LAMMPS.²³⁰ The two-body potential expression is $V_2 = \varepsilon A (B \sigma^p r_{ij}^{-p} - \sigma^q r_{ij}^{-q}) e^{[\sigma(r_{ij} - \alpha\sigma)^{-1}]}$. The three-body potential in the 2D CG model is equated to two-body potential. Parameters λ and $\cos\theta_0$ are set to 0 due to that they are used only for three-body interactions. The quantity *tol* in the last column is a controlling parameter in LAMMPS.

			$\varepsilon(\text{eV})$	$\sigma(\text{\AA})$	α	λ	γ	$\cos\theta_0$	A	B	p	q	<i>tol</i>
S_0^+	Mo_0	Mo_0	1.000	1.255	2.518	0.000	1.000	0.000	6.922	7.156	4	0	0.0
S_0	S_0^+	S_0^+	1.000	1.642	2.518	0.000	1.000	0.000	2.252	7.156	4	0	0.0
S_0^+	S_0^+	S_0^+	1.000	1.643	2.518	0.000	1.000	0.000	2.257	7.156	4	0	0.0
Mo_0	Mo_0	Mo_0	1.000	1.643	2.518	0.000	1.000	0.000	2.076	7.156	4	0	0.0

Table 4.5: SW potential parameters for the 1st order 2D CG model for SLMoS₂ used by LAMMPS.²³⁰

			$\varepsilon(\text{eV})$	$\sigma(\text{\AA})$	α	λ	γ	$\cos\theta_0$	A	B	p	q	<i>tol</i>
S_1^+	Mo_1	Mo_1	1.000	3.882	2.518	0.000	1.000	0.000	110.760	7.156	4	0	0.0
S_1	S_1^+	S_1^+	1.000	1.642	2.518	0.000	1.000	0.000	36.028	7.156	4	0	0.0
S_1^+	S_1^+	S_1^+	1.000	6.572	2.518	0.000	1.000	0.000	36.107	7.156	4	0	0.0
Mo_1	Mo_1	Mo_1	1.000	6.572	2.518	0.000	1.000	0.000	33.217	7.156	4	0	0.0

Previous research²⁶³ has shown that parameter B can not be determined by the linear VFF model, while B corresponds to the nonlinear mechanical behavior. In other words, parameter B has no effect on linear properties. Parameter B is then fixed using the nonlinear quantity as $B = 0.552b_i^4$.²⁶³ In this way, we have analytically determined all the SW potential parameters uniquely. Table. 4.4 and 4.5 list the SW potential parameters for 0th and 1st order 2D CG models for SLMoS₂. Note that the three-body potential in the 2D CG model is equated to two-body potential as discussed previous.

Note that there are three advantages for the SW potential development in this method. First, such SW potential fully inherits the accuracy of the VFF model, and then it can provide accurate description for the linear properties, which can be accurately described by the VFF model. Second, as shown by Eq.4.23, the equilibrium structure has been prebuilt-in during the derivation, thus such SW potential provides accurate relaxed configuration intrinsically. Third, this SW potential includes nonlinear effects through the nonlinear form of two-body term as shown in Eq.4.22, so the SW potential is able to provide the nonlinear properties.

4. SELF-ACTUATED BREATHING-LIKE OSCILLATION

4.2.2 Application

We have presented the development of our 2D CG model for SLMoS₂ in the previous subsection. The rest of this section is devoted to the application of this 2D CG model. We firstly investigate the mechanical properties of SLMoS₂ to verify the accuracy of the SW potential, especially equating the three-body bending potential to two-body tensile potential via virtual bonds, and then study the adsorption effects on the resonant frequency. The publicly available LAMMPS package²³⁰ is used to perform the following simulations. Note that the choice of a proper order of 2D CG model is global-size dependent in the sense that, on one hand, the CG beads should be small enough to capture the fine features, and on the other hand, large enough to reduce the computational cost.

4.2.2.1 Elastic properties for SLMoS₂

To calculate the elastic properties of SLMoS₂, including the in-plane Young's modulus and the Poisson's ratio, we perform MD simulations to stretch a SLMoS₂ with a dimension of 35.0 * 35.0 Å. The interaction is described by the SW potential for 0th order 2D CG model (i.e. atomic SLMoS₂), as shown in Table. 4.4. The relaxed SLMoS₂ is deformed in the armchair direction, while the structure is allowed to relax to keep a free stress in the zigzag direction.

The stress-strain curve is shown in Fig. 4.4. We note some phase transitions at strain about 0.2, which has been discussed in previous studies.⁸⁰ Through the definition, the Young's modulus of the SLMoS₂ is extracted using the stress-strain curve in the linear deformation regime with strain less than 0.07. We obtain the Young's modulus $E = 150$ GPa, which agree well with previous result,³⁵³ where the original SW potential developed by Jiang is applied to describe the atomic interaction.²⁶³

Fig. 4.5 shows the stretching in the armchair direction versus the contraction in the zigzag direction. The Poisson's ratio can be obtained through its definition, $\nu = \frac{\partial \epsilon_{zig}}{\partial \epsilon_{arm}}$. The obtained Poisson's ratio is $\nu = 0.36$, which is very close to the value 0.35 in the previous work,³⁵³ where the original SW potential²⁶³ is used.

4.2.2.2 Adsorption effects on resonant frequency.

For SLMoS₂ with large size, some external molecules or atoms are unavoidable to adsorb on the surface. Adsorption can induce considerably effects on the frequency of

4.2 2D CG model development

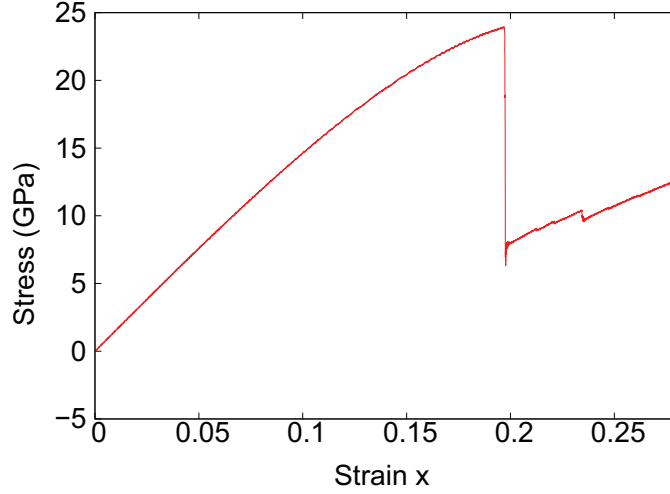


Figure 4.4: Stress versus strain (The dimension of SLMoS₂ is 35 * 35 Å).

the nanoresonators. Previous research⁷¹ has shown that adsorption can significantly reduce the resonant frequency of the graphene nanoresonators.

To investigate the adsorption effects on the resonant frequency of the nanoresonator, an external bead is randomly attached to the 2D CG model of SLMoS₂. The 1st order 2D CG model sample in the following simulations has dimensions $(L_x, L_y) = (120, 120)$ Å, with 270 beads composed. The beads at the $+x$ and $-x$ end of the CG sample are fixed, and the periodic boundary conditions are applied in the y direction. The interactions between S_i and Mo_i beads are described by SW potential, as shown in Table. 4.5. The adsorption of this attached bead is described by the stretching interaction with three nearest-neighboring beads in the 2D CG model. The stretching strength is captured by the stretching parameter K_L^a . The standard Newton equations of motion are integrated in time using the velocity Verlet algorithm with a time step of 1 fs.

The simulations are performed as follows. First, the Nosé-Hoover^{284,285} thermostat is applied to thermalize the entire system to a constant temperature within the NPT (i.e., the particles number N , the pressure P and the temperature T of the system are constant) ensemble, which is run for 200 ps. The resonant oscillation is then actuated by adding a sine-shaped velocity distribution, $v_0 \sin(\pi x_j/L)$, to the system. In all simulations, the velocity amplitude $v_0 = 2.5$ Å/ps is applied. After the actuation, the system is allowed to oscillate freely within the NVE (i.e., the particles number N , the volume V and the energy E of the system are constant) ensemble for 2^{19} MD steps, and the oscillation energy from the NVE ensemble is recorded to analyze the resonant frequency of the nanomechanical resonator.

4. SELF-ACTUATED BREATHING-LIKE OSCILLATION

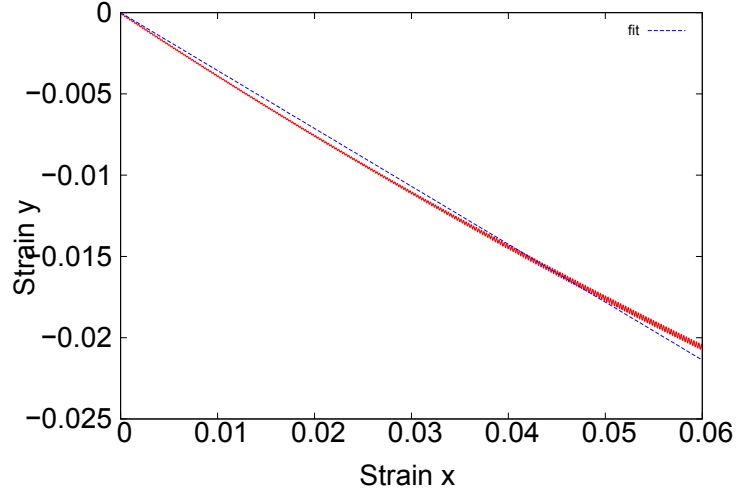


Figure 4.5: Strain y - strain x curve.

During the free vibration periods, the energy in the resonator switches between potential energy and kinetic energy. The frequency of resonant oscillation is f , so the frequency of the switching is $2f$. Fig. 4.6 shows the resonant peak that is obtained by taking a Fourier transformation of the time history of the kinetic energy; the resonant peak is used to extract the resonant frequency $f = 108.8$ GHz of the pure CG nanoresonator at 300 K. Fig. 4.7 illustrates the adsorption effects on the resonant frequency of the oscillation in the 2D CG model. We consider three adsorption strengths, i.e. $K_L^a = 1.0K_{\xi_0}^0$, $0.1K_{\xi_0}^0$ and $0.01K_{\xi_0}^0$. We find that there is no significant frequency shift induced by the adsorption, and the frequency is insensitive to the adsorbed mass.

The stable resonant frequency may be due to the fact that the mass of the external bead is negligible comparing with the whole large oscillation system, and then it is difficult for the adsorbed mass to have an overall effect on the oscillation, which is essentially a kind of global motion. That means the symmetry of the actuated oscillation is not affected obviously, which has been found to strongly affect the characteristic parameters of graphene nanomechanical resonators.⁵⁷

4.2.3 Conclusion

We parametrize a 2D CG model of SLMoS₂ with SW potential. All SW geometrical parameters are determined analytically from the equilibrium condition for each potential term, while the SW energy parameters are derived analytically based on the VFF

4.3 1D CG model development

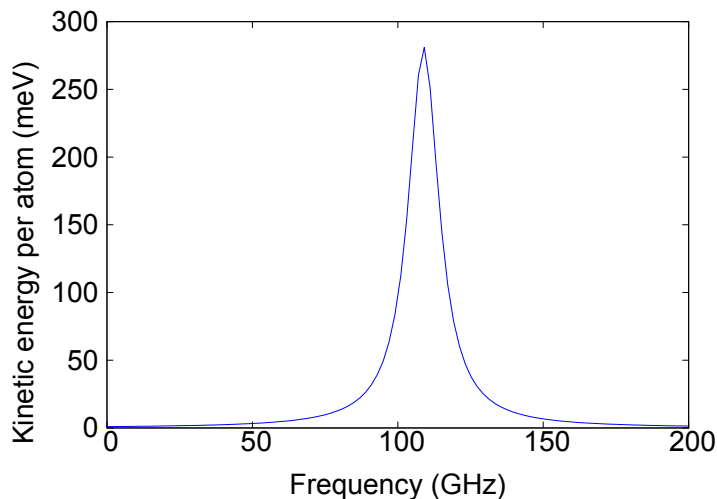


Figure 4.6: Fourier transformation.

model. We verify the accuracy of 2D CG model via mechanical properties of SLMoS₂. Furthermore, we investigate the adsorption effects on the resonant frequency. We find that the resonant frequency of the 2D CG nanoresonator is insensitive to the adsorbed mass.

4.3 1D CG model development

We have presented the 2D CG model of SLMoS₂ in the previous section. In order to further simplify the SLMoS₂, we will propose the 1D CG model in the following section. More specifically, in Sec. 4.3.1, we perform two kinds of MD simulations for MoS₂ to compute fundamental mechanical parameters of MoS₂ based on the SW atomic potential, including adhesion and elastic properties. In Sec. 4.3.2, a simple 1D CG model is parametrized analytically from the atomic structure. Sec. 4.3.3 is dedicated to the application of the 1D CG model to investigate the breathing-like resonant oscillation in the folded SLMoS₂. This section ends with a brief conclusion in Sec. 4.3.4.

4. SELF-ACTUATED BREATHING-LIKE OSCILLATION

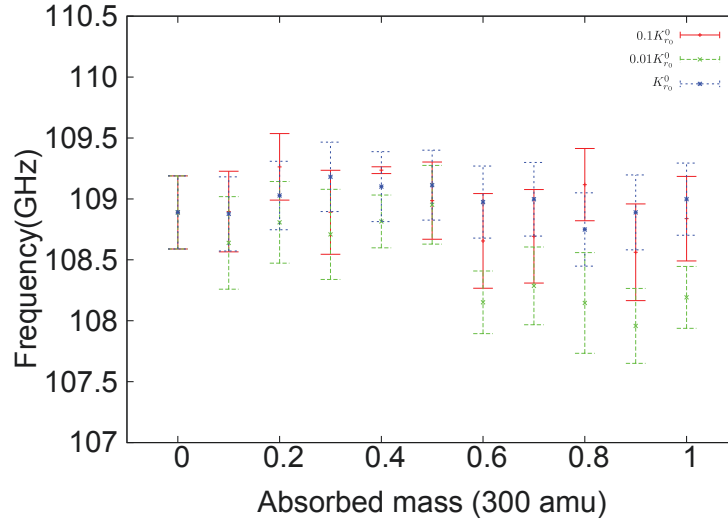


Figure 4.7: Adsorption effects on the resonant frequency.

4.3.1 Atomic simulation for MoS₂

Atoms in SLMoS₂ are mainly covalently bonded, with a Mo atomic layer sandwiched by two S atomic layers. Each Mo atom is surrounded by six S atoms, while each S atom is bonded to three Mo atoms. These covalent interactions can be described by the SW potential with five potential terms.⁸⁰

We first perform MD simulations for the MoS₂, where the SW potential is used to describe the atomic interaction. The SW potential is a microscopic model, and is generally more accurate than the 1D CG model. We thus use the SW potential to compute mechanical properties for MoS₂, which will be used to determine the 1D CG potential parameters. More specifically, we calculate the interlayer space, the cohesive energy, the Young's modulus, and the Poisson's ratio for MoS₂.

4.3.1.1 Coherent energy for bilayer MoS₂

We calculate the cohesive energy for the MoS₂, i.e., the potential energy that is required to separate two coupling MoS₂ layers. Fig. 4.8 shows the configuration of two interacting MoS₂ layers with the dimensions 32 * 32 Å. Two MoS₂ layers interact through the van der Waals interaction between neighboring S atoms from different MoS₂ layers. The van der Waals interaction is described by the Lennard-Jones potential with $\epsilon_{sw} = 0.00693$ eV, $\sigma_{sw} = 3.13$ Å.³³⁵

4.3 1D CG model development

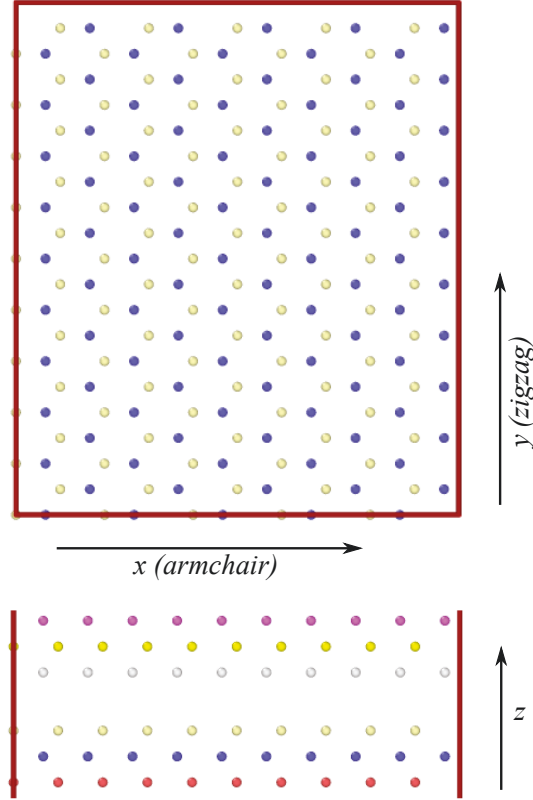


Figure 4.8: Structure for the bilayer MoS₂ with dimensions of 32 * 32 Å, from the top view in the top panel, and from the side view in the bottom panel.

Two AB-stacking MoS₂ layers are relaxed to energy minimum configuration by the conjugate gradient method using LAMMPS.²³⁰ The equilibrium interlayer space is $\Delta D = 6.17$ Å. The minimum interlayer potential energy is V_0 . We then calculate the interlayer potential for the bilayer MoS₂ at different interlayer space values. Fig. 4.9 shows the obtained interlayer potential with respect to the minimum interlayer potential V_0 . The x-axis in the figure is the space variation with reference to the equilibrium interlayer space ΔD . In the limit of $dz \in \infty$, we get the cohesive energy of 20.2 meV/atom, which is the work to be done if one separates the two interacting MoS₂ layers. This quantity can be used to extract the cohesive energy density for the MoS₂ as 14.44 meV/Å².

4. SELF-ACTUATED BREATHING-LIKE OSCILLATION

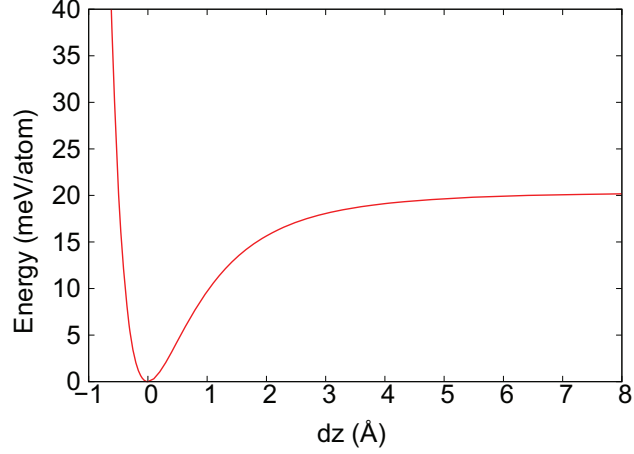


Figure 4.9: The relative interlayer potential for the bilayer MoS₂ with respect to different interlayer spacings dz . For $dz = 0$, the interlayer space is at the equilibrium value of 6.17 Å. The cohesive energy is around 20.2 meV/atom, which is the energy required to depart two coupling MoS₂ layers.

4.3.1.2 Elastic properties for SLMoS₂

To calculate the in-plane Young's modulus and the Poisson's ratio for the SLMoS₂, we perform molecular mechanics simulations to stretch a SLMoS₂ with the dimensions 35.0 * 35.0 Å. The SLMoS₂ is relaxed to its energy minimum configuration. The relaxed SLMoS₂ is deformed in the armchair direction, while the structure is allowed to relax to keep a free stress in the zigzag direction.

Fig. 4.10 shows the stress-strain curve for the deformation process. The calculated stress is actually a volume density quantity. The SLMoS₂ is a Q2D structure, with some arbitrariness in its thickness definition. We have used the equilibrium interlayer space $\Delta D = 6.17$ Å as the thickness of the SLMoS₂. We note some phase transitions at strain around 0.2 in Fig. 4.10, which has been discussed in previous studies.⁸⁰ The stress-strain curve in the linear deformation regime with strain less than 0.08 is used to extract the Young's modulus of the SLMoS₂ through its definition. The obtained Young's modulus is $E = 124.58$ GPa. This Young's modulus value is comparable with existing experimental values, which are actually quite divergent.^{329,330,331}

During the stretching of the SLMoS₂ in the armchair direction, the structure contracts in the lateral zigzag direction due to Poisson's effect. Fig. 4.11 shows the contraction in the zigzag direction versus the stretching in the armchair direction. The Poisson's ratio can be obtained through its definition, $\nu = \frac{\partial \epsilon_{\text{zig}}}{\partial \epsilon_{\text{arm}}}$. The obtained Pois-

4.3 1D CG model development

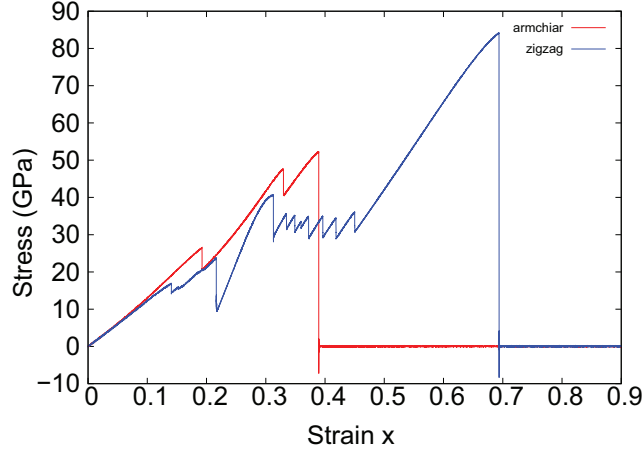


Figure 4.10: Stress versus strain. SLMoS₂ dimensions: 35 * 35 Å.

Table 4.6: Quantities from molecular mechanics simulations using the SW potential.

E (GPa)	ν	E_c ($\frac{meV}{\text{Å}^2}$)	ΔD (Å)
124.58	0.35	14.44	6.17

son's ratio is $\nu = 0.35$.

Table 4.6 summarizes all quantities that have been obtained from the above molecular mechanics simulations based on the SW atomic potential. These quantities will be used to determine the 1D CG model in the following.

4.3.2 Parametrization of 1D CG model

In the above, we have illustrated molecular mechanics simulations for MoS₂ using the SW potential to describe the interaction between microscopic atoms. The atomic potential model is accurate, in the sense that it provides microscopic interaction information, which can be used to simulate mechanical properties on macroscopic level. However, the atomic potential model will be computationally expensive for very large pieces of MoS₂, or hybrid MoS₂ materials. Furthermore, the atomic configuration of MoS₂ is too complicated for some analytic studies. To address this, a 1D CG model can be helpful. In the 1D CG model, the structure of SLMoS₂ is simplified by some CG beads, and the inter-bead potential is quite suitable for analytic derivations. We note

4. SELF-ACTUATED BREATHING-LIKE OSCILLATION

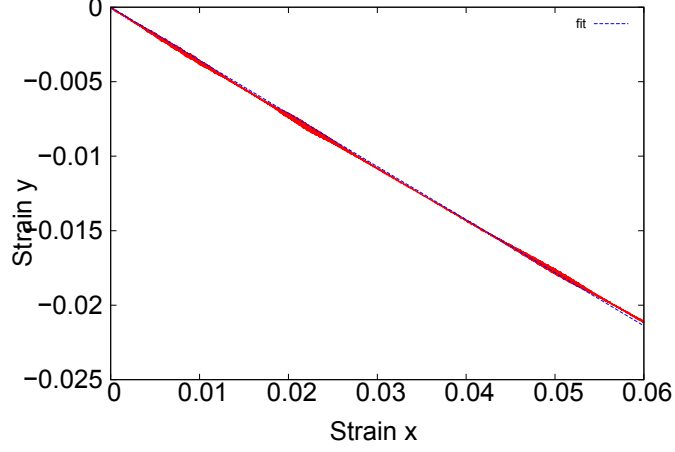


Figure 4.11: Strain y - strain x curve.

that the Poisson's effect is ignored in this 1D CG model, which will result in some small systematic errors for the mechanical properties of SLMoS₂.

4.3.2.1 1D CG model

There are two major ingredients in the 1D CG model; i.e., the bead structure and the inter-bead potential. Fig. 4.12 illustrates how to simplify the 2D atomic structure of SLMoS₂ using a 1D CG bead chain. This type of substitution ignores the Poisson's effect in the other dimension. Hence this 1D CG model is applicable for physical phenomena where the Poisson's effect is not important, such as the folding of MoS₂. The mass of each bead is m_{CG} , and the distance between two neighboring beads is ξ_0 . The total length of the bead chain is $L_x = N\xi_0$, where N is the total bead number.

For the 1D bead chain structure, there are three major interactions among beads,

$$V = V_L + V_B + V_{weak}, \quad (4.26)$$

where V_L is the stretching energy associated with the variation in the inter-bead distance ξ . The second term V_B is the bending energy, and V_{weak} is the non-bonded van der Waals interaction. The detailed expressions for these three potentials are demonstrated in the following for a specific bead.

(1). The stretching energy between two neighboring beads is,

$$V_L = \frac{1}{2}k_L(\xi - \xi_0)^2, \quad (4.27)$$

4.3 1D CG model development

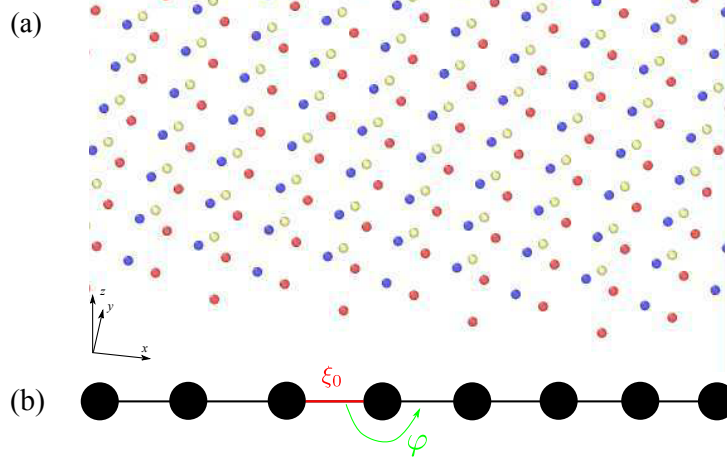


Figure 4.12: Atomic and corresponding 1D CG model of SLMoS₂. (a) The atomic representation of SLMoS₂, which is substituted by (b), a chain of beads interacting with various molecular potentials.

where K_L is the corresponding 1D CG potential parameter, which will be determined in the next subsection. The distance ξ_0 is the initial inter-bead distance. The total stretching energy in the CG bead model is a summation over the stretching energy between all neighboring beads.

(2). The bending energy corresponding to three neighboring beads is,

$$V_B = \frac{1}{2}k_B(\varphi - \varphi_0)^2, \quad (4.28)$$

where k_B is the 1D CG bending parameter. Initially, the CG bead chain is a linear chain, so we have the initial bending angle $\varphi_0 = 180^\circ$. The total bending energy is the collection of bending energy in all neighboring beads.

(3). The weak non-bonding van der Waals interaction between two beads is described by the following LJ potential,

$$V_{LJ} = 4\varepsilon\left[\left(\frac{\sigma}{r}\right)^{12} - \left(\frac{\sigma}{r}\right)^6\right], \quad (4.29)$$

where ε is the energy parameter describing the well depth of the potential, and σ is a length parameter corresponding to the zero potential distance. The total weak non-bonding energy in the 1D CG bead model can be calculated by summarizing the LJ potential between all bead pairs in the bead chain.

4. SELF-ACTUATED BREATHING-LIKE OSCILLATION

4.3.2.2 Potential parameters for the 1D CG model

We have presented some general information for the 1D CG model in the previous subsection and will now determine all 1D CG model parameters in the following.

Equilibrium distance and mass of beads

The equilibrium distance between two neighboring beads in Fig. 4.12 is ξ_0 , and the total bead number is N . There is only one restriction between these two quantities, i.e., $N\xi_0 = L_x$, with L_x as the total length of the SLMoS₂. We choose ξ_0 as 10 Å and 20 Å, respectively. The bead number is $N = L_x/\xi_0$.

The bead mass is chosen to affirm that the total mass of the bead chain equals to the total mass of the SLMoS₂; i.e., $m_{CG} * N = \rho L_x L_y$, where $\rho = 19.1 \text{ amu}/\text{Å}^2$ is the mass surface density for SLMoS₂. As a result, we get $\frac{m_{CG}}{L_y} = \rho \xi_0$ as the bead mass.

Tensile parameter

As an important requirement of the 1D CG model development, the CG bead chain should have the same tensile properties as the original SLMoS₂ structure. That is the stretching energy in both systems should be the same if these two systems are deformed by the same amount of mechanical strain. The SLMoS₂ is regarded as a thin plate with Young's modulus E , so the strain energy in a deformed system by strain ε is

$$V_{MoS2} = \frac{1}{2} E (A_c L_x) \varepsilon^2, \quad (4.30)$$

where $A_c = L_y h$ is the cross section area.

The total strain energy stored in the deformed CG bead chain by strain ε is,

$$V_{CG} = N * \frac{1}{2} k_L * (\xi_0 \varepsilon)^2. \quad (4.31)$$

By equating the stretching energy in the SLMoS₂ and the CG bead chain, we obtain the analytic expression for the stretching parameter in the 1D CG model,

$$\frac{k_L}{L_y} = \frac{E h}{\xi_0}, \quad (4.32)$$

where all quantities on the right side are known already.

4.3 1D CG model development

Bending spring parameter

The bending parameters in the 1D CG model are determined by equating the bending potential in the SLMoS₂ and the bending potential in the bead chain. It is assumed that both systems are uniformly bent. The 2D SLMoS₂ is regarded as a thin plate, which is bent from its initial planar structure into a cylinder with radius R . The corresponding bending potential is described by the famous formula,³³⁶

$$V_B = \frac{Eh^3}{24(1-\nu^2)} \frac{2\pi L_y}{R}, \quad (4.33)$$

where h is the finite thickness. This formula displays that the bending energy for a thin plate essentially originates from strain energy; i.e., the stretching energy in the outer regime and the compressing energy stored in the inner regime of the cylinder. In doing so, we have used the elastic bending modulus derived previously²⁴¹ to determine the bending parameter in the present work.

Similarly, the CG bead chain is uniformly bent into a circle with radius R . Using the bending potential model in Eq. (4.28), the corresponding bending energy is

$$V_B = \frac{\pi K_B \xi_0}{R}. \quad (4.34)$$

The 1D CG model is developed with the requirement that the CG bead model has the same bending properties as the original SLMoS₂ atomic system. As a result, by equating Eq. (4.33) to Eq. (4.34), we obtain the bending parameter in the 1D CG model,

$$\frac{K_B}{L_y} = \frac{Eh^3}{12(1-\nu^2)\xi_0}, \quad (4.35)$$

where the value of the Young's modulus E and the Poisson's ratio ν have been obtained from the molecular mechanics simulations based on the SW atomic model.

LJ parameters

In the CG bead chain model, the van der Waals interaction exists between all bead pairs. For two beads from the same CG chain, the interaction is dominated by the stretching or bending energy, so the weak van der Waals interaction can be ignored. For two beads from two different CG chains, the van der Waals potential is the only interaction, which dominates the inter-chain coupling between two chains for the 1D CG model. We thus determine the LJ parameters in the 1D CG model by considering the van der Waals interaction between two neighboring CG chains.

4. SELF-ACTUATED BREATHING-LIKE OSCILLATION

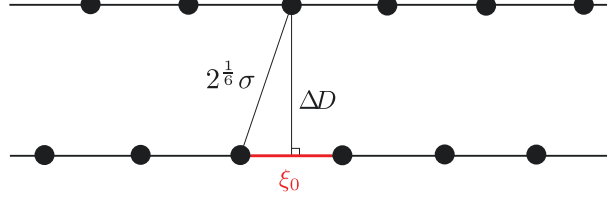


Figure 4.13: Two neighboring CG chains.

The most stable configuration for two neighboring CG chains is the zigzag-like structure shown in Fig. 4.13, where two parallel chains are relatively shifted by a distance of $\frac{\xi_0}{2}$. The length parameter σ in the LJ potential is determined by keeping the equilibrium distance between two CG chains the same as the interlayer equilibrium space between two MoS₂ layers. The LJ interaction between two inter-chain first-nearest-neighboring beads is the dominant inter-chain potential, so the distance between two inter-chain first-nearest-neighboring beads actually corresponds to the minimum energy distance, $2^{\frac{1}{6}}\sigma$. As a result, we have $(2^{\frac{1}{6}}\sigma)^2 = (\Delta D)^2 + (\frac{\xi_0}{2})^2$, which leads to

$$\sigma = 2^{\frac{1}{6}} \times D \times \sqrt{1 + (\frac{\xi_0}{2D})^2}. \quad (4.36)$$

The other parameter in the LJ potential in the 1D CG model is the energy parameter ε . The energy parameter is determined by equating the cohesive energy between two CG chains and the cohesive energy between two MoS₂ layers. Previously, we have obtained the cohesive energy for two MoS₂ layers as $L_x L_y * E_c$. It is assumed that the inter-chain coupling in the 1D CG model is contributed by the LJ potential between two first-nearest-neighboring inter-chain beads. Under this approximation, we get the cohesive energy between two parallel neighboring bead chains as $2N\varepsilon$. As a result, the energy parameter ε can be obtained from the equality of the cohesive energy between two MoS₂ layers and the cohesive energy between two CG chains,

$$\frac{\varepsilon}{L_y} = \frac{E_c \xi_0}{2}. \quad (4.37)$$

It should be noted that the first-nearest-neighboring approximation will introduce some errors in the above analytic formula. Fig. 4.14 shows the energy parameter determined using different cut-offs in the LJ potential. The error is about 3% when cutting the inter-bead LJ potential to the first-nearest-neighboring beads.

4.3 1D CG model development

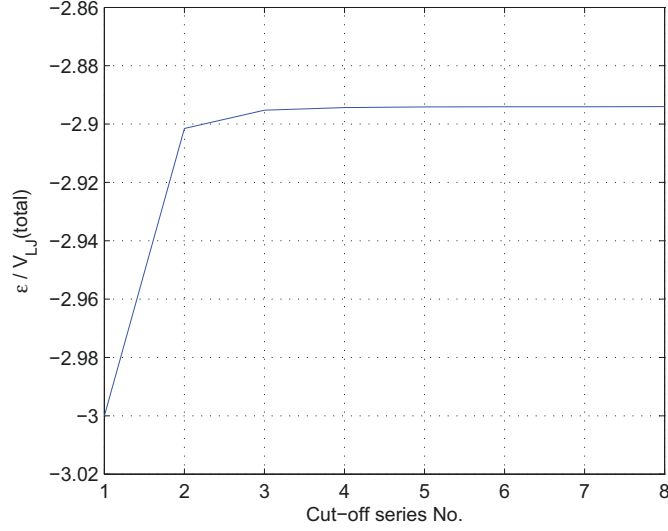


Figure 4.14: ϵ versus different cut-off series numbers.

Table 4.7: Parameters in the 1D CG model of the SLMoS₂.

ξ_0 (Å)	$\frac{m_{CG}}{L_y}$ ($\frac{amu}{\text{Å}}$)	$\frac{K_L}{L_y}$ ($\frac{eV}{\text{Å}^3}$)	$\frac{K_B}{L_y}$ ($\frac{eV}{\text{Å}}$)	$\frac{\epsilon}{L_y}$ ($\frac{eV}{\text{Å}}$)	σ (Å)
10.0	191	0.48	1.73	0.0722	7.08
20.0	382	0.24	0.865	0.1444	10.47

4.3.2.3 Summary of the 1D CG model

Table 4.7 summarizes all parameters in the 1D CG model. All energy parameters and the mass parameter associate with the lateral dimension L_y of the SLMoS₂. Without losing generality, we will set $L_y = 1$ Å in the following calculations, as this factor has no effect in any of the CG simulations. This treatment is reasonable, because it does not affect the competition between different potentials.

4.3.3 Application of 1D CG model to folded MoS₂

We have presented the 1D CG model for the SLMoS₂ in the previous subsection. The rest of this section is devoted to using the 1D CG model to simulate the folded MoS₂ nanoresonators. We will illustrate the advantages of the 1D CG model, which is par-

4. SELF-ACTUATED BREATHING-LIKE OSCILLATION

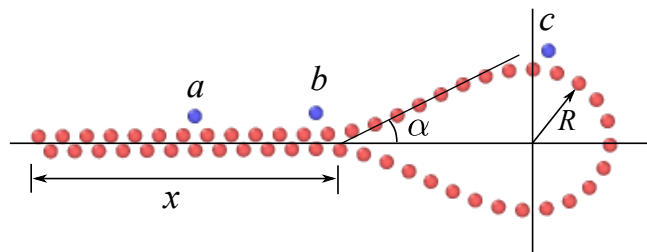


Figure 4.15: Optimized structure of the folded MoS_2 at 0 K. There are three representative positions in the folded structure; i.e., ‘a’ on the parallel segment, ‘b’ at the junction of left and right parts, and ‘c’ on the curvature part.

ticularly useful in deriving some analytic expressions. We firstly study the structure of the folded SLMoS_2 , and then investigate one self-actuated resonant oscillation of the folded SLMoS_2 .

4.3.3.1 Related structure for folded MoS_2

We simulate the CG chain with total length $L_x = N\xi_0 = 520 \text{ \AA}$, so the bead numbers are $N = 52$ with respect to $\xi_0 = 10 \text{ \AA}$ and $N = 26$ with reference to $\xi_0 = 20 \text{ \AA}$. Numerical results show that the relaxed structures are similar for different ξ_0 (10 \AA and 20 \AA). Fig. 4.15 shows the relaxed structure of the folded SLMoS_2 using the 1D CG model with $\xi_0 = 10 \text{ \AA}$. There are mainly three regimes in the folded structure; i.e., two parallel CG chains on the left side, a half CG chain circle on the right side, and two tilted CG chains in the middle regime. There are two characteristic geometrical parameters in the folded MoS_2 , i.e., the tilted angle α in the middle regime and the radius R in the right regime. The numerical CG simulation gives $\alpha = 26.5^\circ$ and $R = 27.5 \text{ \AA}$ as measured from Fig. 4.15. For the CG chain with $\xi_0 = 20 \text{ \AA}$, α and R are measured as 26.5° and 28.7 \AA . We can see that α is a constant and R is basically the same. We note that the structure will become softer if it is described by the 1D CG model with a larger bead bond,³³⁷ so there is actually no convergence in the choice of the bead bond length. We have thus chosen the bead bond length as 10 \AA , in accordance with that used in carbon nanotubes.⁸¹

Due to the simplicity of the 1D CG model, we can actually derive an analytic relationship between these two geometrical parameters α and R . As shown in Fig. 4.15, the

4.3 1D CG model development

left regime contains two parallel straight CG chains, and both CG chains are straight and not stretched, so the other two CG potential terms, stretching energy and bending energy, are zero. As a result, the potential is mainly contributed by the LJ potential between these two interacting CG chains in the left regime,

$$V_{\text{left}} = \frac{2\varepsilon}{\xi_0}x. \quad (4.38)$$

In the right regime, the CG chain is uniformly bent, so the bending energy dominates the CG potential in the right regime. The stretching energy in the right regime is almost zero, as all beads can manipulate their positions to relax the stretching stress between beads, which has been confirmed by CG simulation results. As a result, we get the CG potential within the right regime,

$$V_{\text{right}} = \frac{1}{2} \frac{\pi K_B \xi_0}{R}. \quad (4.39)$$

In the middle regime, the CG potential is almost zero, as the tilted CG chains are neither stretched nor bent. It can also be understood from the comparison between the middle regime and other two regimes, i.e., the middle region is very small as compared with the left or right region, so the CG potential is much smaller than the potential of the left and right regions. Hence, we get the total CG potential in the folded SLMoS₂ structure,

$$V_{\text{fold}} \rightarrow V_{\text{left}} + V_{\text{right}} = \frac{2\varepsilon}{\xi_0}x + \frac{1}{2} \frac{\pi K_B \xi_0}{R}, \quad (4.40)$$

which can be regarded as the folding potential of the SLMoS₂. There is a geometrical constraint to ensure that the total length of the SLMoS₂ is a constant L_0 . We thus get the following relationship between the length x of the left parallel chains, and the radius R of the bent CG chain in the right regime,

$$L_0 = 2x + 2 * \frac{R \frac{\Delta D}{2}}{\sin \alpha} + \pi R. \quad (4.41)$$

Inserting this geometrical constraint into the folding potential equation, we expand the folding potential as a function of variables R , assuming α as a constant,

$$V_{\text{fold}} = \frac{1}{2} \frac{\pi K_B \xi_0}{R} \frac{\varepsilon(L_0 - \pi R - 2 * \frac{R \frac{\Delta D}{2}}{\sin \alpha})}{\xi_0}. \quad (4.42)$$

4. SELF-ACTUATED BREATHING-LIKE OSCILLATION

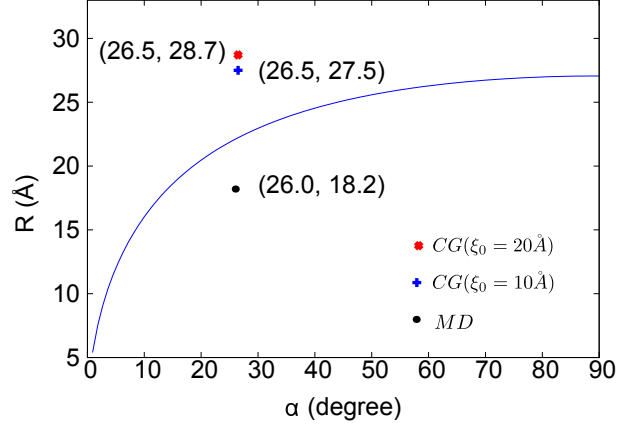


Figure 4.16: Analytic relationship between the geometrical parameters R and α . The points are from CG or MD simulations.

The relaxed folded configuration is determined by minimizing the total folding potential according to $\frac{\partial V_{\text{fold}}}{\partial R} = 0$, resulting in the following equation,

$$\frac{1}{2} \frac{\pi K_B \xi_0}{R^2} + \frac{\varepsilon}{\xi_0} \left(\pi + \frac{2}{\sin \alpha} \right) = 0. \quad (4.43)$$

As a result, we obtain an analytic expression for geometrical variable R ,

$$R = \xi_0 \sqrt{\frac{\pi K_B}{2\varepsilon \left(\pi + \frac{2}{\sin \alpha} \right)}}. \quad (4.44)$$

Inserting all CG potential parameters, we obtain the relationship between R and α , as shown in Fig. 4.16. The dots (26.5, 27.5) and (26.5, 28.7) in the figure represent the structure parameters from the above CG numerical simulations. The numerical data deviate slightly from the analytic prediction, due to the simplicity of the above analytic structure model. From Eq. (4.44), we can see that R will be a constant while the change of ξ_0 , and the angle is also keep the same, which can be verified by the CG simulations.

4.3.3.2 Self-actuated breathing-like oscillation

We have used the 1D CG model to determine the relaxed configuration of the folded SLMoS₂, which was achieved by minimizing the folding potential energy at $T = 0$ K in the previous subsection. We now consider the structure evolution of the folded SLMoS₂ at finite temperature.

Simulation details

4.3 1D CG model development

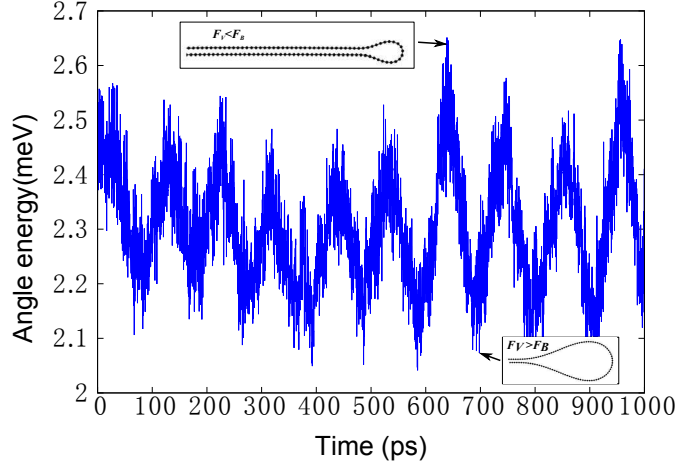


Figure 4.17: Bending energy of the folded MoS₂. $T = 80K$, $N = 52$.

We perform MD simulations to study the motion of the folded SLMoS₂ at finite temperature using the 1D CG model. The relaxed folded SLMoS₂ structure is thermalized to a constant temperature using the NPT (i.e., constant particle number N , constant pressure P , and constant temperature T) ensemble for 500 ps. The targeted pressure is set to be zero. The N ose-Hoover thermostat^{284,285} is used to control the constant pressure and temperature, and Newton equations are integrated by the velocity Verlet method.

Resonant frequency and Quality factor

After thermalization, we continue to observe the thermal vibration of the folded SLMoS₂ with $\xi_0 = 10 \text{ \AA}$. More specifically, we monitor the time history for each CG potential component, and find that there is an obvious frequent exchange between the bending potential and the LJ potential. This energy exchange occurs at a finite frequency. Fig. 4.17 shows the oscillation between the bending potential and the LJ potential at $T = 80 \text{ K}$, while the total folding potential is almost a constant during the oscillation. The insets in Fig. 4.17 clearly demonstrate the structure evolution during the energy oscillation. The folded SLMoS₂ oscillates like a breather, so this is a type of breathing-like nanoresonator. We point out that this breathing-like oscillation is self-actuated, i.e., it is actuated by thermal vibration without any external actuation. This self-actuation is an interesting advantage over other nanoresonators that have been discussed in existing works, which require an external actuation of the resonant oscillation.

The resonant frequency and the Q factor are two characteristic parameters for

4. SELF-ACTUATED BREATHING-LIKE OSCILLATION

nanoresonators. To compute these two quantities, we perform the fast Fourier transformation for the time history of the bending potential. Fig. 4.18 shows the Fourier transformation results for the bending potential of the folded SLMoS₂ at $T = 80$ K. The position of the resonant peak gives the resonant frequency (f_c) of the breathing-like oscillation, and the width of the resonant peak is related to the life time (τ) of the oscillation. The resonant peak in Fig. 4.18 can be fitted by the Lorentzian function, $E = \frac{E_m}{1+[(f-f_c)/\gamma]^2}$, with three fitting parameters, i.e. E_m as the peak magnitude at $f = f_c$, $f_c = 9.6$ GHz, and $\gamma = 3.153$ GHz as the half-width at half-maximum. The resonant frequency of the breathing-like oscillation is f_c , while the life time of this oscillation is $\tau = \frac{1}{\gamma}$. The Q-factor can be obtained as $2\pi f_c * \tau = 19.1$. The Q-factor is not very high. However, the low Q-factor will be not a problem for the practical applications of the breathing-like oscillation of the folded SLMoS₂, because this oscillation is self-actuated, i.e., the breathing-like oscillation will not decay. The self-actuation intrinsity will enable a practical application of the breathing-like resonator.

Similarly, we test the thermal vibration of the folded SLMoS₂ with $\xi_0 = 20$ Å. The frequency is found to be 9.33 GHz, which is nearly the same with the folded SLMoS₂ with $\xi_0 = 10$ Å.

Using the 1D CG model, we are able to determine the resonant frequency analytically. As shown in Eq. (4.42), the folding potential depends on the radius R of the bent CG chain in the right regime. During the breathing-like oscillation, there is variation in the radius R , i.e., $R \in R + \Delta R$. The corresponding retracting force constant can be obtained as

$$K = \frac{\partial^2 V_{\text{fold}}}{\partial R^2} = \frac{\pi K_B \xi_0}{R^3}. \quad (4.45)$$

The resonant frequency for the breathing-like oscillation is

$$f = \frac{1}{2\pi} \sqrt{\frac{K}{m}} = \frac{1}{2\pi} \sqrt{\frac{\pi^4 K_B}{2N_0^4 \xi_0^2 m_{CG}}} \rightarrow 10.0 \text{ GHz}, \quad (4.46)$$

where geometrical relations, $N_0 \xi_0 = \pi R$ and $m = 2N_0 m_{CG}$, have been applied. The bead number in the half circle chain in the right regime is $N_0 = 10$ in Fig. 4.15. This analytic result is very close to the CG numerical simulation frequency of 9.6 GHz for $\xi_0 = 10$ Å and 9.33 GHz for $\xi_0 = 20$ Å. From Eq. (4.46), we can see that the frequency will keep the same with changing ξ_0 , which has been verified by the CG simulation. In addition, these analytic results confirm that the resonant frequency is indeed the result of the breathing-like oscillation for the folded MoS₂.

Temperature and adsorption effects on resonant frequency

4.3 1D CG model development

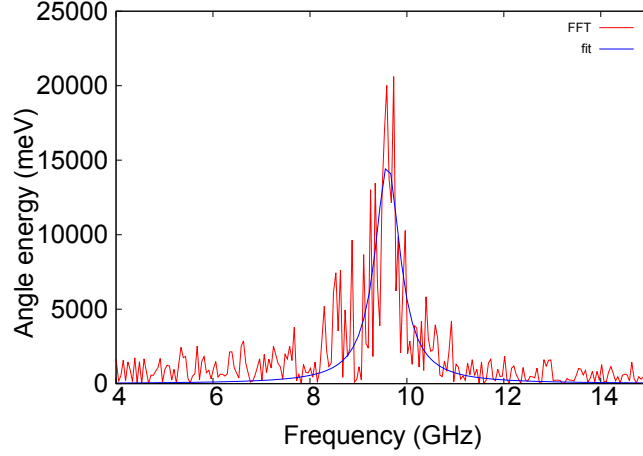


Figure 4.18: Fourier transformation. The red line shows the Fourier transformation result. There are many different oscillations, but the peak magnitude shows the frequency of the most obvious one, i.e. the breathing-like oscillation. The blue line shows the fitting results: $f_c = 9.6GHz$ and $\gamma = 3.153GHz$.

As the resonant frequency of the breathing-like oscillation is constant, here we will only examine the temperature and adsorption effects for the folded SLMoS₂ with $\xi_0 = 10 \text{ \AA}$. Figure. 4.19 shows the temperature dependence for the resonant frequency of the breathing-like oscillation for the folded SLMoS₂. The resonant frequency increases with increasing temperature, except some small variations at low temperatures due to the weak thermalization control at low temperatures. The resonant frequency will be saturated at around 9.6 GHz for temperatures above 150 K. According to the analytic expression in Eq. (4.46), the frequency is proportional to the square of the CG bending parameter. Hence, the increase of the frequency indicates that the CG bending parameter increases with increasing temperature; i.e., the CG chain becomes more difficult to bent at higher temperatures. This temperature induced stiffing effect is similar to the in-plane mechanical strength of graphene, which also increases with increasing temperature.³³⁸

The folded SLMoS₂ has a large surface area, so some external atoms or molecules will unavoidably adsorb on the surface. The adsorption effects can induce strong effects on the resonant frequency of nanomechanical resonators. For instance, it has been shown that the adsorption can considerably reduce the resonant frequency for graphene nanomechanical resonators.³³⁹

To examine the adsorption effects on the resonant frequency of the breathing-like oscillation for the folded SLMoS₂, an external bead is attached to the folded SLMoS₂

4. SELF-ACTUATED BREATHING-LIKE OSCILLATION

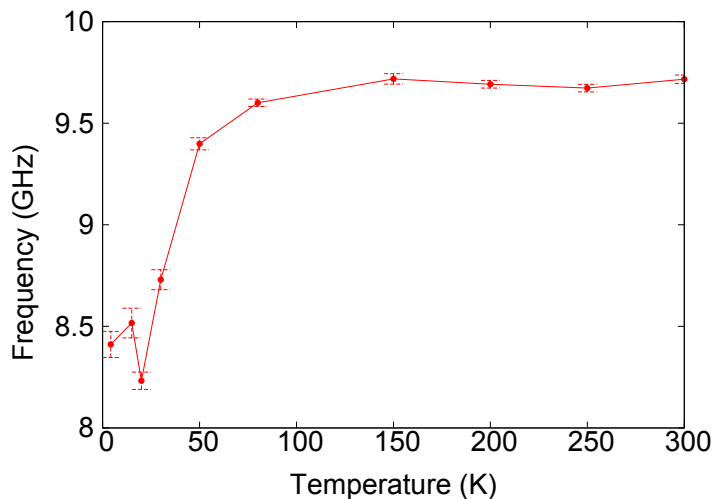


Figure 4.19: Temperature effects on the resonant frequency.

as shown in Fig. 4.15. We have investigated three different possible positions for the attaching process. The adsorption of this external bead is described by stretching interactions with two nearest-neighboring beads in the original 1D CG model. The stretching strength between the adsorbate and the SLMoS₂ is captured by the stretching parameter K_L^a . Fig. 4.20 illustrates the adsorption effects on the resonant frequency of the breathing-like oscillation in the folded SLMoS₂. For each adsorption position, we consider three adsorption strengths, i.e., $K_L^a = 1.0K_L$, $0.1K_L$, and $0.01K_L$. We find that the resonant frequency is insensitive to the adsorbed mass, and there is no obvious frequency shift induced by adsorption.

The stable resonant frequency may be due to the fact that such breathing-like oscillation actually depends on energy exchange between the weak LJ potential and the bending potential. The adsorption effect does not affect such energy exchange phenomenon. On the other hand, the folded SLMoS₂ is very soft, so it is difficult for the adsorbed mass to have an overall effect on the breathing-like oscillation, which is essentially a kind of global motion. Such a stable resonant frequency may be useful for some practical applications, where the adsorption is unavoidable.

Before conclusion, we make a comparison between the CG simulation and the atomic MD simulation for the folded SLMoS₂. We perform atomic MD simulations for the SLMoS₂ with a length of 520 Å and a width of 15.6 Å. Fig. 4.21 shows the relaxed configuration of the folded SLMoS₂, where the interaction is described by the SW potential.⁸⁰ The obtained geometrical parameters α and R are 26.0° and 18.2 Å, respectively. These results are also plotted in Fig. 4.16. It shows that the CG result

4.3 1D CG model development

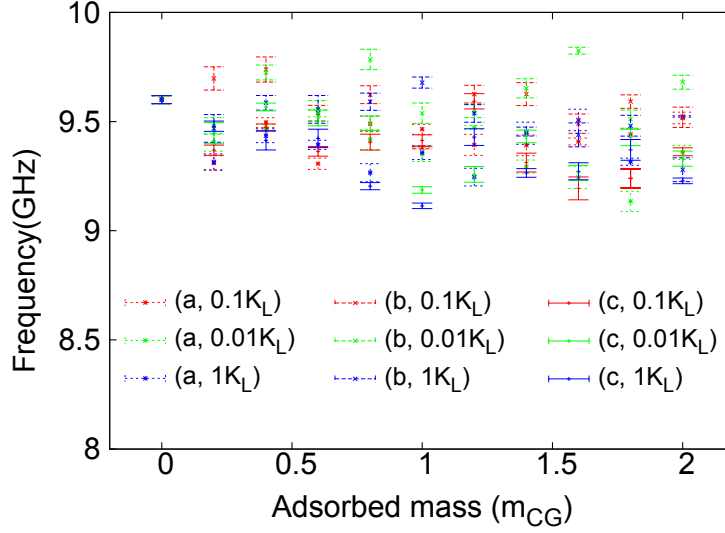


Figure 4.20: Adsorption effects on the resonant frequency.

and the MD result are close to the analytic curve from Eq. (4.44). We also perform MD simulates to examine the self-actuated breathing-like oscillation of the atomic folded SLMoS₂. The resonant frequency is about 9.32 GHz at 1.0 K from the MD simulation, which is very close to the CG simulation results. The agreement between the CG simulation and the MD simulation further establishes the accuracy of the 1D CG model proposed in the present work.

4.3.4 Conclusion

For this section, we have performed CG simulations to investigate the breathing-like oscillation of the folded SLMoS₂. The 1D CG potential parameters are determined analytically based on the SW atomic potential model for the SLMoS₂. Our CG simulations illustrate several advantages for the breathing-like oscillation of the folded SLMoS₂. First, this oscillation is self-actuated; i.e., it can be actuated by intrinsic thermal vibrations without any external actuation efforts. Second, we further demonstrate that the resonant frequency of the breathing-like oscillation is very stable, as it is almost unchanged by adsorption phenomenon.

4. SELF-ACTUATED BREATHING-LIKE OSCILLATION

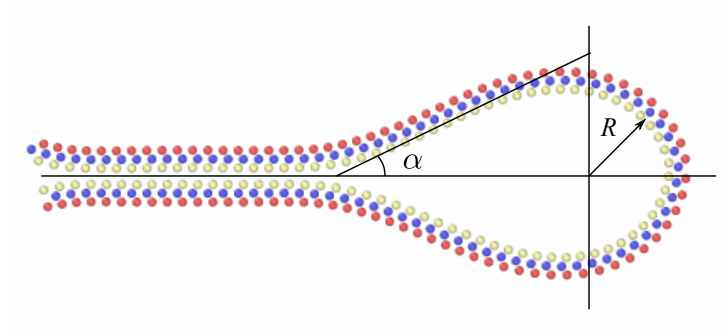


Figure 4.21: Relaxed atomic structure of the folded SLMoS₂, with $\alpha = 26.0^\circ$ and $R = 18.2 \text{ \AA}$.

4.4 Comparison

As the most important principle of CG method, on one hand, the CG model should be accurate enough to capture the fine features of different phenomena, and on the other hand, the CG model should reduce the computational cost effectively. Comparing with atomic SLMoS₂, both of 1D and 2D CG models can save the simulation cost, with 1D CG model more effective. Furthermore, 1D CG model is quite suitable for analytic derivations. However, 1D CG model is only applicable for physical phenomena where the Poisson's effect is not important like the folding of MoS₂, since the Poisson's effect is ignored in the other dimension. By contrast, 2D CG model has an advantage to resolve 2D problems, such as the fracture growth.

Chapter 5

Mechanical Engineering for Black Phosphorus Nanoresonators

5.1 Introduction

BP is a new 2D nanomaterial that is comprised of atomic layers of phosphorus stacked via van der Waals forces.²² BP brings a number of unique properties unavailable in other 2D crystal materials. For example, BP has anisotropic properties due to its puckered configuration.^{23,24,25,26}

While most existing experiments have been focused on potential electronic applications of BP,^{27,28,29} a recent experiment showed that the resonant vibration response of BPR can be achieved at a very high frequency.³⁰ However, there have been no theoretical studies on the intrinsic dissipation in BPRs to-date. In particular, it is interesting and important to characterize the effects of mechanical strain on the Q-factors of BPRs, and furthermore considering that mechanical strain can act as an efficient tool to manipulate various physical properties in the BP structure.^{31,32,33,34,35,36,37,38} For example, a large uniaxial strain in the direction normal to the SLBP plane can even induce a semiconductor-metal transition.^{39,40,41,42} We thus investigate the mechanical strain effect on the BPRs of armchair and zigzag directions, at different temperatures.

Furthermore, currently, SLBP, i.e. phosphorene,²⁴ can be fabricated by mechanical exfoliation from bulk BP and has immediately received considerable attention.^{44,45,46} Atomic vacancies have been demonstrated to exist in bulk BP.^{47,48} Recently, first-principles calculations have demonstrated that these defects can be generated quite easily in SLBP at much higher concentrations compared with silicene and graphene.

5. MECHANICAL ENGINEERING FOR BLACK PHOSPHORUS NANORESONATORS

^{49,50} Cai et al.⁵¹ suggested that intrinsic itinerant behavior of atomic vacancies may result in the low chemical stability of phosphorene. In addition, another invariable issue encountered in the manipulation of SLBP is the control of the oxidation. It has been established by both theoretical calculations and experiments that O_2 can easily dissociate on black phosphorene^{52,53} leading to the formation of the oxidized lattice.⁵⁴ The presence of oxygen is suggested to be the main cause of the degradation process^{52,55} and primarily responsible for changing properties of BP,⁵⁶ e.g., BP is turned progressively hydrophilic by oxidation. In particular, vacancies recently have been found to have significant effects on the oxidation of phosphorene with a 5000 faster oxidizing rate at the defect site than at the perfect site,²⁹¹ and a thickness-dependent photoassisted oxidation reaction with oxygen dissolved in adsorbed water was also reported recently.²⁹² Very recently, Feng's group has examined the BPR experimentally.⁴³ However, the experimental BPR samples should have some unavoidable vacancy defects or oxidation.⁴³ Furthermore, these defects can have strong effects on the performance of resonant oscillation of the nanomechanical resonators. For instance, it has been known that various defects can significantly affect the performance of graphene nanomechanical resonators.^{57,58,59} An important task is thus to examine the defect effects (including vacancy defects and oxidation) on the BPRs, which is another topic of this chapter.

In this chapter, we focused exclusively on two mechanism effects on SLBPR via classical MD simulations, i.e. mechanical strain effects and defect effects (including vacancy and oxidation). For mechanical strain effects, both uniaxial and biaxial tensions are found to increase the Q-factor of the SLBPR, as the resonant frequency is enhanced by the applied tension. However, the Q-factor decreases beyond a critical strain value due to the introduction of nonlinear energy dissipation, which becomes dominant at large tensile strains. As a result, there is a critical strain at which the Q-factor reaches the maximum value, which is about 4% and 8% at 50 K for mechanical tension along the zigzag and armchair directions, respectively. We find that the nonlinear dissipation is stronger if the BPR is stretched along the zigzag direction, which results in a smaller critical strain. For vacancy defect and oxidation, it is found that these defects can cause a considerable degradation of the Q-factors of the SLBPRs. More specifically, a 2% concentration of randomly distributed SV is able to reduce the Q-factor by around 80% and 40% at 4.2 K and 50 K, respectively. The DV defect has similar reduction as the SV in the Q-factors of the SLBPRs. We also find that the Q-factor is mainly dependent on the percentage of the defects, while it is not sensitive to the distribution pattern of the defects. Furthermore, it is found that oxidation has a weaker reduction in the Q-factors of the SLBPRs, as compared with the vacancy defects.

5.2 Structure and simulation details

5.2.1 Structure

Fig. 5.1 (a) shows the atomic structure of the SV, DV and oxidized defects in the SLBP, with a dimension of $50 * 50 \text{ \AA}$ that is used in our simulations. We have simultaneously considered the vacancy and oxidation effects in the present work, as density functional theory calculations have shown that these two defects usually occur together.²⁹¹ Vacancy defects are generated by removing atoms from the pristine SLBP. A SV defect is formed by removing one phosphorus atom, while a DV defect is formed by removing two nearest-neighbor phosphorus atoms in the same sub-layer, which has the lowest formation energy.^{49,294} For the oxidized defect, the oxygen atom is put on the dangling position, which is the most stable configuration according to the previous first-principles calculations.^{54,295,296,297} We note that the position of the oxygen is different from that of graphene oxide, where the bridge site is the preferred binding site for the oxygen atom.²⁹⁸ As shown in Fig. 5.1 (b), the oxygen atom bonds with one phosphorus atom, with a P-O bond (i.e., bond 1-7) length of 1.5 \AA , and the P-O bond is tilted by 44.5° away from the phosphorene surface.^{295,297} The phosphorus atom involved in the P-O bond gets dragged into the lattice structure by 0.11 \AA in the z direction; apart from that, the lattice deformation ignored in the present work is minimal.²⁹⁵ Correspondingly, three angles $\angle OPP$ are formed, i.e., $\angle 712 (118^\circ)$, $\angle 713 (118^\circ)$ and $\angle 714 (115^\circ)$. The defect concentration is the ratio of the number of atoms removed or adsorbed over the total number of phosphorus atoms in the pristine SLBP. The MD simulations are carried out using the publicly available simulations code LAMMPS,²³⁰ while the OVITO package was used for visualization.²⁹⁹

5.2.2 Interatomic potential

The atomic interactions among the phosphorus atoms in the structure are described by a recently-developed SW potential.²⁶³ In the development of the SW potential, all geometrical parameters in the SW potential are determined analytically according to the equilibrium condition for each individual potential term, while the energy parameters are derived from the VFF model. In doing so, the accuracy of the VFF model is transferred to the SW potential. This SW potential gives accurate linear properties, which have been shown to be comparable to the first-principles calculations. In particular, the phonon dispersion computed from the SW potential agrees quite well with the first-principles calculations. The resonant oscillation of the SLBP resonator follows the lowest-frequency phonon branch (flexural mode) in the SLBP. Hence, the linear

5. MECHANICAL ENGINEERING FOR BLACK PHOSPHORUS NANORESONATORS

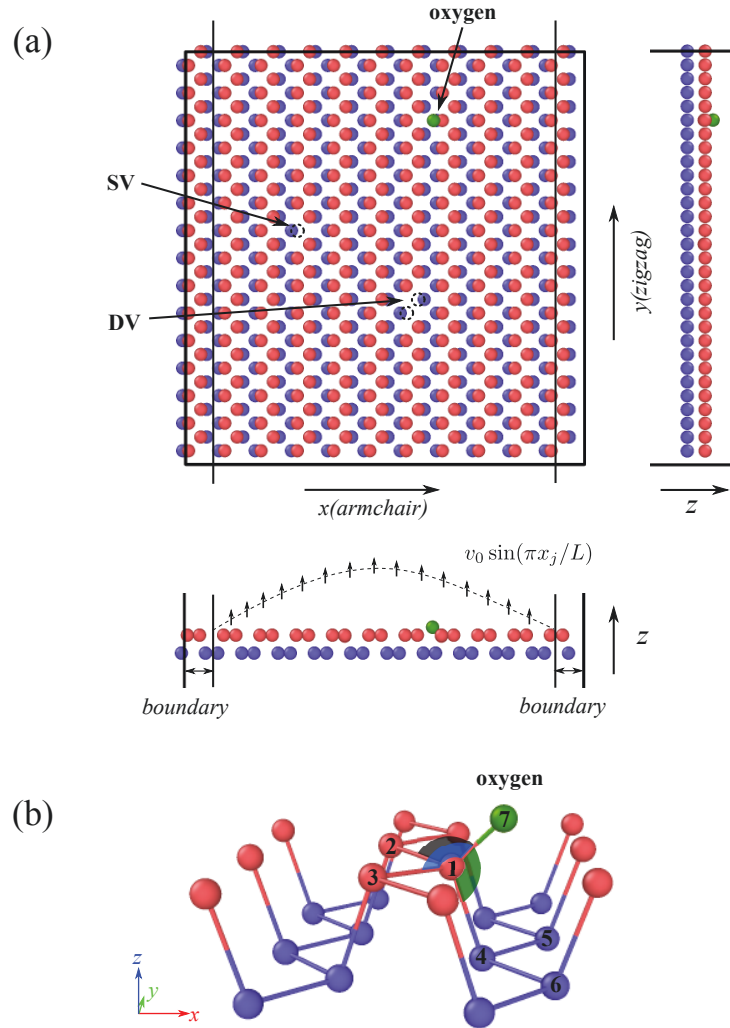


Figure 5.1: (a) Configuration of SLBP with dimensions $50 \times 50 \text{ \AA}$, containing a SV defect, a DV defect and an oxidized defect. Arrows in the bottom image indicate the direction of actuation. (b) Configuration of SLBP with an oxidized defect. There are two interaction terms associated with the oxygen atom, i.e., the bond-stretching term (bond 1-7) and the angle-bending term ($\angle 712$, $\angle 713$ and $\angle 714$). The x-axis is along the armchair direction, and the y-axis is along the zigzag direction.

5.2 Structure and simulation details

properties (such as frequency) predicted in the present work are accurate. This SW potential also yields accurate nonlinear properties. It has been shown in the original reference that the stress-strain relation for the uniaxial tension of SLBP is accurate in the nonlinear deformation regime. As a result, the nonlinear properties (like the Q-factor) predicted in the present topic should also be fairly accurate.

The interaction between the oxygen atom and the SLBP is described by the bond stretching and angle bending potentials. For the bond stretching interaction, the force constant is obtained from the optimized potentials for liquid simulations (OPLS) potential, i.e., 22.776 eV/\AA^2 .³⁰⁰ The OPLS potential is able to capture essential many-body terms in interatomic interactions, including bond stretching, bond angle bending, van der Waals and electrostatic interactions.³⁰¹ For the angle bending interaction, there is no available value for its force constant parameter K . We thus treat K as a simulation parameter in the following calculations; i.e., we will use different values for the force constant parameter K in the MD simulations. The standard Newton equations of motion are integrated in time using the velocity Verlet algorithm with a time step of 1 fs .

5.2.3 Simulation details

The BPR simulations are performed in the following manner. First, the entire system is thermalized to a constant temperature within the NPT (i.e., the particles number N , the pressure P and the temperature T of the system are constant) ensemble by the Nosé-Hoover^{284,285} thermostat, which is run for 200 ps. Second, the SLBP is stretched by uniaxial or biaxial strain along the armchair or zigzag directions. The mechanical strain is applied at a strain rate of $\dot{\epsilon} = 0.0001 \text{ ps}^{-1}$, which is a typical value in MD simulations. Third, the configuration is divided into two parts as shown in the bottom panel of Fig. 5.1 (a), i.e., the boundary part ($2 * 5 \text{ \AA}$) is fixed while the central part is actuated. The resonant oscillation of the SLBP is actuated by adding a sine-shaped velocity distribution, $v_0 \sin(\pi x_j/L)$, to the system. In all simulations, we apply the velocity amplitude $v_0 = 2.0 \text{ \AA/ps}$, which is small enough to keep the resonant oscillation in the linear region. Fourth, the resonant oscillation of the SLBP is simulated within the NVE (i.e., the particles number N , the volume V and the energy E of the system are constant) ensemble for 90 ns, and the oscillation energy is recorded to extract the Q-factor.

5.3 Results and discussion

In this section, intrinsic energy dissipation of the pristine SLBPRs is firstly studied. Next, effects of mechanical strain and defects (including vacancy and oxidation) on BP nanoresonators are investigated in turn.

5.3.1 Intrinsic energy dissipation of the pristine SLBPRs

We first examine the intrinsic energy dissipation of the pristine SLBPRs along the armchair and zigzag directions. The intrinsic energy dissipation is induced by thermal vibrations at finite temperatures. Fig. 5.2 shows the kinetic energy time history for armchair SLBPRs at 4.2 K, 30 K and 50 K. The oscillation amplitude of the kinetic energy decays gradually, which reflects the energy dissipation during the resonant oscillation of the SLBPR. As the temperature increases, energy dissipation becomes stronger, indicating a lower Q-factor at a higher temperature.

The frequency and the Q-factor of the resonant oscillation can be extracted from the kinetic energy time history by fitting to the function $E_k(t) = \bar{E}_k + E_k^0 \cos(2\pi 2ft) (1 - \frac{2\pi}{Q})^{ft}$. The first term \bar{E}_k represents the average kinetic energy after the resonant oscillation has completely decayed. The constant E_k^0 is the total kinetic energy at $t = 0$, i.e. at the moment when the resonant oscillation is actuated. The frequency of the resonant oscillation is f , so the frequency of the kinetic energy is $2f$. The kinetic energy time history is usually a very long data set, so it is almost impossible to fit it directly to the above function. The fitting procedure is thus done in the following two steps as shown in Fig. 5.3. First, Fig. 5.3 (a) shows that the energy time history is fitted to the function $E_k(t) = \bar{E}_k + E_k^0 \cos(2\pi 2ft)$ in a very small time region $t \in [0, 50]$ ps, where the approximation of $(1 - \frac{2\pi}{Q})^{ft} \rightarrow 1$ has been used for the Q-factor term as the energy dissipation is negligible in the small time range. The parameters E_k^0 and f are obtained from this step. Second, Fig. 5.3 (b) shows that the oscillation amplitude of the kinetic energy can be fitted to the function $E_k^{\text{amp}}(t) = E_k^0 (1 - \frac{2\pi}{Q})^{ft}$ in the whole simulation range $t \in [0, 90]$ ns, which determines the Q-factor and \bar{E}_k . Following these fitting procedures, the Q-factor is 63250 for the armchair SLBPR at 50 K.

Fig. 5.4 shows the temperature dependence for the Q-factor of the SLBPR along the armchair and zigzag directions. At most temperatures, the Q-factor is larger in the armchair direction. It means that the energy dissipation is weaker for the armchair SLBPR, considering that the frequency in the armchair SLBPR is only half of that in the zigzag SLBPR.²⁶³ The temperature dependence for the Q-factor can be fitted to the functions $Q = 1.9 * 10^7 T^{-1.4}$ and $Q = 3.0 * 10^6 T^{-1.0}$ for the armchair and zigzag

5.3 Results and discussion

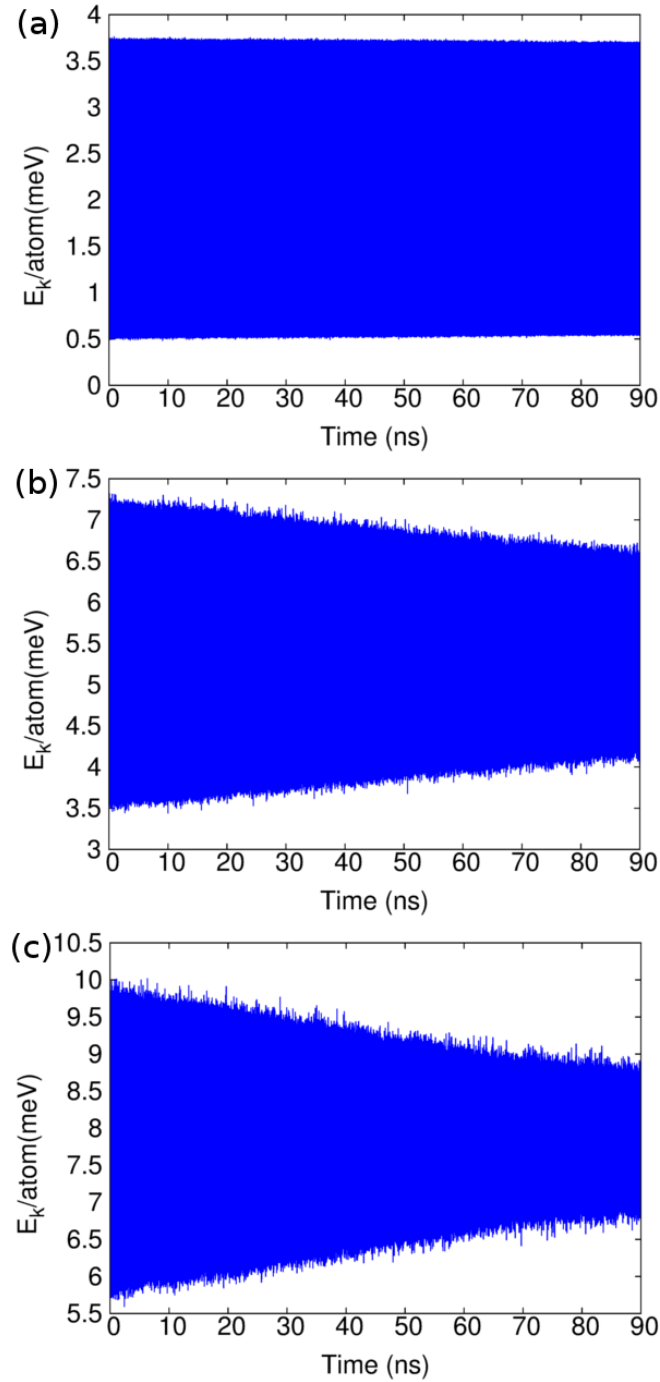


Figure 5.2: The kinetic energy per atom for armchair SLBPRs at 4.2 K, 30 K and 50 K from top to bottom. The Q-factors are 1621900, 110000 and 63250, respectively.

5. MECHANICAL ENGINEERING FOR BLACK PHOSPHORUS NANORESONATORS

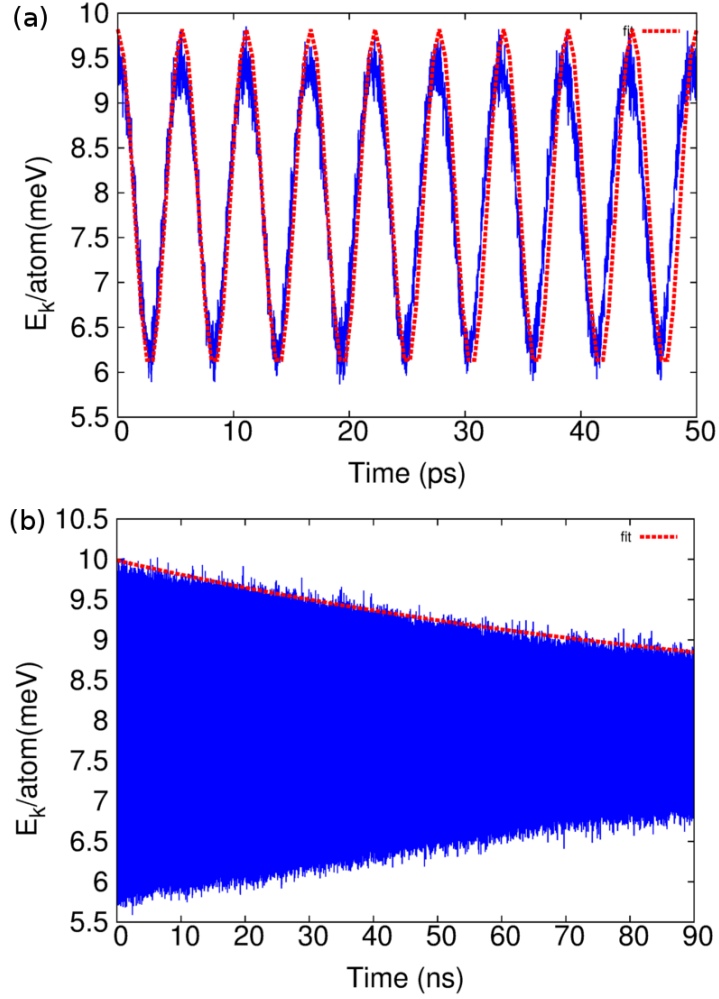


Figure 5.3: Two-step fitting procedure to extract the frequency and Q-factor from the kinetic energy time history for armchair SLBPR at 50 K. (a) The kinetic energy is fitted to the function $E_k(t) = \bar{E}_k + E_k^0 \cos(2\pi 2ft)$ in a small time range, giving a frequency of $f = 0.090874$ THz. (b) The kinetic energy is fitted to the function $E_k^{\text{amp}}(t) = E_k^0 (1 - \frac{2\pi}{Q})^{ft}$ in the whole time range, yielding the Q-factor value of 63250.

5.3 Results and discussion

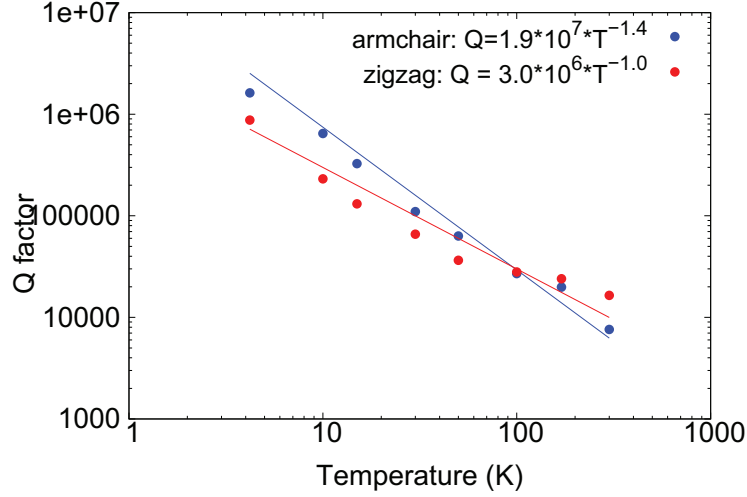


Figure 5.4: Temperature dependence for the Q-factors of the armchair and zigzag SLBPRs.

SLBPRs, respectively. We find that the Q-factor is in the order of 1000 at room temperature in our simulations, which is one order larger than the experimental value of 100.³⁰ In our numerical simulations, only the phonon-phonon scattering effect is included in determining the Q-factor of the BPR. In other words, we have investigated the intrinsic nonlinear effect as the energy dissipation mechanism for the resonator. However, there are many other energy dissipation mechanisms that could be introduced experimentally that are not accounted for in our simulations, i.e. ohmic losses, attachment losses, and two level systems.²⁸⁶ Furthermore, BP is not stable under ambient conditions and defects could be present in the system. All of these factors could contribute to lowering the Q-factors for the experimental studies as compared with the pristine, defect-free system we have considered in our simulations.

These Q-factors are higher than the Q-factors in graphene nanoresonators ($Q = 7.8 * 10^4 T^{-1.2}$).^{70,247} This is likely because there is also a large energy bandgap in the phonon dispersion of SLBP,²⁸⁷ which helps to preserve the resonant oscillation of the SLBPR.²⁴⁷ In contrast, there is no such energy bandgap in the phonon dispersion of graphene, so the SLBPR has a higher Q-factor than the graphene nanoresonator. The Q-factors of SLBPRs are also higher than those of MoS₂ nanoresonators ($Q = 5.7 * 10^5 T^{-1.3}$).²⁴⁷ Both SLBP and MoS₂ have energy bandgaps in their phonon dispersions. This is important as our simulation results imply that nonlinear phonon-phonon scattering is weaker in SLBP, i.e., the resonant energy dissipation is weaker in SLBP than MoS₂.

5. MECHANICAL ENGINEERING FOR BLACK PHOSPHORUS NANORESONATORS

It is interesting to speculate how the Q-factors of multilayer BP would be compared with monolayer phosphorene. For multilayer BP, there are weak van der Waals interactions between individual phosphorene layers. The van der Waals interactions can reduce the Q-factors because they act as a frictional force between the layers, which provides an additional channel for energy dissipation of the nanoresonators. Specifically, the strength of the interlayer van der waals forces is likely to be the dominant factor in controlling the amount of energy that is dissipated, as was demonstrated for the case of multilayer graphene resonators by Kim and Park⁶⁸.

5.3.2 Mechanical strain effects on SLBPRs

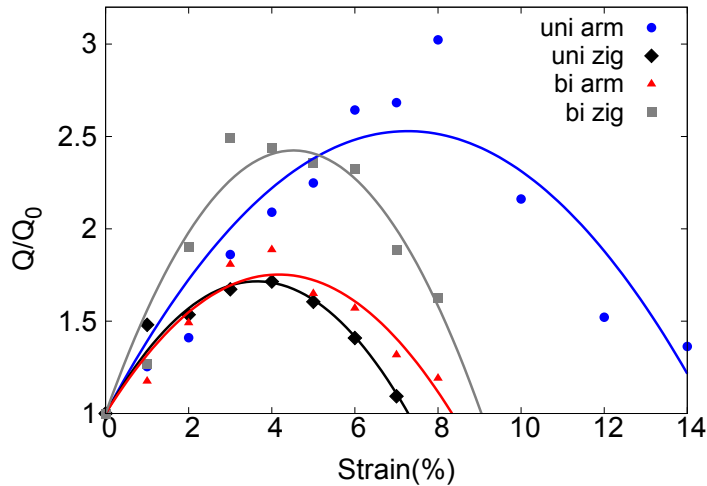


Figure 5.5: Strain dependence for the Q-factor of SLBPR in four cases at 50K. The Q-factor depends on the strain as the function $Q/Q_0 = a\epsilon^2 + b\epsilon + 1.0$, which gives a maximum Q-factor value at a critical strain.

We now report the effects of mechanical strain on both armchair and zigzag SLBPRs at 50 K. We consider four cases, i.e., (I) the effect of uniaxial strain on the armchair SLBPR, (II) the effect of uniaxial strain on the zigzag SLBPR, (III) the effect of biaxial strain on the armchair SLBPR, and (IV) the effect of biaxial strain on the zigzag SLBPR. Fig. 5.5 shows the strain dependence for the Q-factor (with reference to the value Q_0 without strain) of SLBPRs under uniaxial or biaxial mechanical tension. In case I, the mechanical strain is applied purely in the armchair direction, while the SLBP is stretched in the zigzag direction in the other three cases.

For all of the four cases, the Q-factor first increases and then decreases after a

5.3 Results and discussion

critical strain value. The Q-factor depends on the strain as the function $Q/Q_0 = a\varepsilon^2 + b\varepsilon + 1.0$, where the fitting parameters (a, b) are $(0.029, 0.42)$, $(0.055, 0.40)$, $(0.043, 0.36)$, and $(0.070, 0.63)$ for the four studied cases, respectively. The linear term $b\varepsilon$ represents the enhancement effect on the Q-factor by the mechanical tension, as the frequency of the resonator is increased by the tension in the small strain range. The quadratic term $a\varepsilon^2$ is because the Q-factor will be reduced by the nonlinear effect resulting from the mechanical tension in the large strain range. The interplay between these two competing effects results in a maximum value for the Q-factor at a critical strain ε_c . The critical strain value is about 8% for case I, in which the mechanical tension is applied only in the armchair direction. For all other three cases, the critical strain is around 4%, where the mechanical tension has a component in the zigzag direction. It is clear that the Q-factor reduction due to the increased dissipation at increased temperature dominates the enhancements in the Q-factor that are possible through mechanical strain. However, Fig. 5.5 shows that strain engineering can be utilized to further manipulate the Q-factor of the BPR at a given temperature.

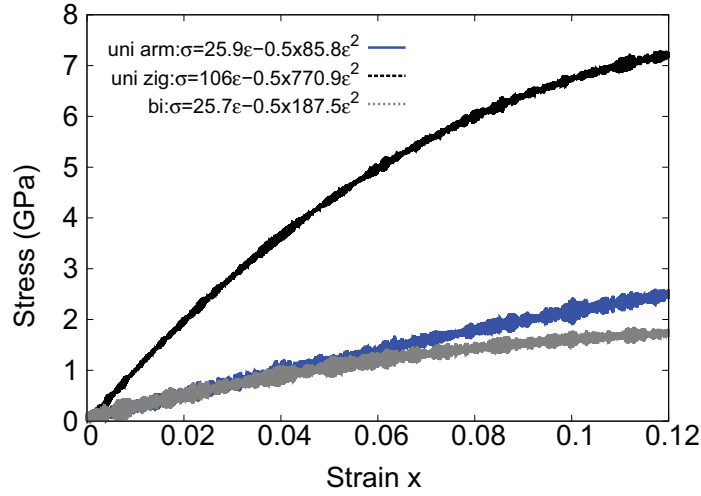


Figure 5.6: Stress-strain relation for SLBP under mechanical tension. The stress (σ) is fitted to a function of the strain (ε) as $\sigma = E\varepsilon + \frac{1}{2}D\varepsilon^2$, with E as the Young's modulus and D as the TOEC. The nonlinear effect is estimated by the ratio $\gamma = \frac{\frac{1}{2}D}{E}\varepsilon$.

The differences in the above critical strains can be understood from the different strain induced nonlinear properties in the SLBP. Fig. 5.6 shows the stress-strain curve for the SLBP stretched in the above four cases. The stress-strain curve is fitted to the function $\sigma = E\varepsilon + \frac{1}{2}D\varepsilon^2$, with E as the Young's modulus and D as the third-order elastic constant (TOEC).²⁶³ The nonlinear to linear ratio of $\gamma = \frac{\frac{1}{2}D}{E}\varepsilon$ gives an overall

5. MECHANICAL ENGINEERING FOR BLACK PHOSPHORUS NANORESONATORS

estimation of the strain induced nonlinear effect on the SLBP. The parameter γ is found to be -1.66 for case I, -3.64 for case II and -3.65 for the other two cases. This means that the nonlinear effect is the weakest in case I, where the SLBP is stretched purely in the armchair direction. As a result, the parameter a has the smallest value for case I, leading to the largest critical strain. This phenomenon (a maximum Q factor due to the strain effect) has also been obtained in nanowire resonators. For example, Kim and Park found that the maximum Q factor occurs at around 1.5% tensile strain in the metal nanowire resonators.¹⁶⁰ Very recently, several different possible stable 2D crystal structures were proposed for phosphorene.^{288,289,290} We believe that similar nonlinear mechanical properties will be found in all of these phosphorene allotropes.

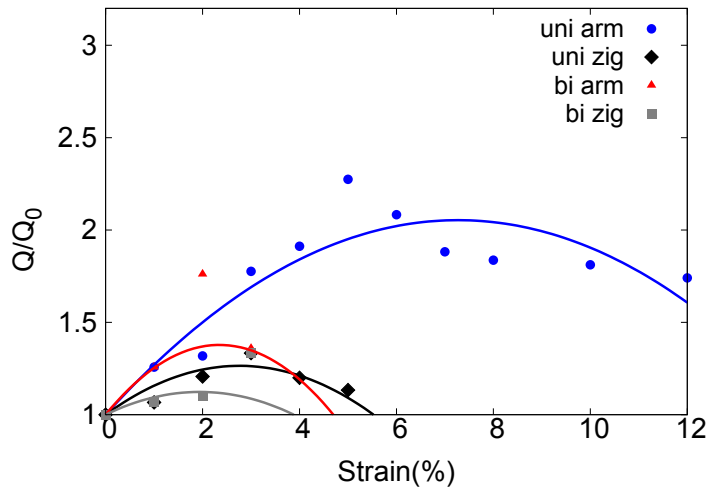


Figure 5.7: Strain dependence for the Q-factor of SLBPR in four cases at 170K.

Fig. 5.7 shows the strain effect on the Q-factor at 170 K for all four cases. The critical strain is also observed at this higher temperature, and the critical strain values for SLBPRs at 170K are about 5% for case I and around 2-3% for other three cases. However, the critical strain value is smaller as compared with the critical strain at 50 K in Fig. 5.5. This is because the nonlinear effect is stronger at higher temperature due to the thermally-induced random vibrations. The combination of the two nonlinear effects (induced by temperature and strain) leads to a smaller critical strain at higher temperature.

5.3 Results and discussion

5.3.3 Defect effects on SLBPRs

We have studied the mechanical strain effects on SLBPRs in the previous subsection, and will examine two defect effects on SLBPRs in the following, i.e. vacancy effects and oxidation effects. Vacancy defect is intrinsic damping factor, while oxidation is extrinsic damping factor.

5.3.3.1 Vacancy effects

Random distribution of SV and DV defects

We first study the energy dissipation of the SLBPRs with randomly distributed SV and DV defects along the armchair and zigzag directions. Fig. 5.8 shows the time history of the kinetic energy per atom for the zigzag SLBPRs at 4.2 K with different concentrations of SV defects. The oscillation amplitude of the kinetic energy decays gradually, which reflects the energy dissipation during the resonant oscillation of the SLBPR. As the defect concentration increases, the energy dissipation becomes stronger, indicating a lower Q-factor with a larger concentration. The frequency and Q-factor of the resonator oscillation can be extracted from the kinetic energy time history via two-step fitting procedure, as shown in Fig. 5.3.

Fig. 5.9 shows the SV and DV concentration dependence for the Q-factors of the armchair and zigzag SLBPRs at 4.2 K and 50 K, respectively. With the increase of the defect concentration, the Q-factors are reduced significantly in both armchair and zigzag directions. For all concentrations considered, the Q-factor is larger in the armchair direction, which shows the same characteristic as the defect free SLBPRs.²⁹³ The reduction of the Q-factor becomes weaker with the increase of the temperature. More specifically, for the SV defect with concentration of 2%, the Q-factor drops by 82.7% and 81.5% in the armchair and zigzag directions, respectively, at 4.2 K, while 40% and 38%, respectively, at 50 K. For the DV defect, the reduction in the Q-factors is similar as the SV defect. We find that the reduction of the Q-factor of the SLBPR does not increase with further increasing defect concentration. More specifically, we perform further calculations for the defect concentrations of 3%, 4% and 5% at 4.2 K, and the Q-factors are almost unchanged. It is interesting that the vacancy effects are isotropic, i.e., the vacancy defects induce almost the same amount of reduction in the Q-factors of the armchair and zigzag SLBPRs.

The intrinsic nonlinear effect on the energy dissipation mechanism for the SLBPRs has been investigated,²⁹³ in which only the phonon-phonon scattering effect is included in determining the Q-factor of the BPR. Comparing with the pristine SLBPR,

5. MECHANICAL ENGINEERING FOR BLACK PHOSPHORUS NANORESONATORS

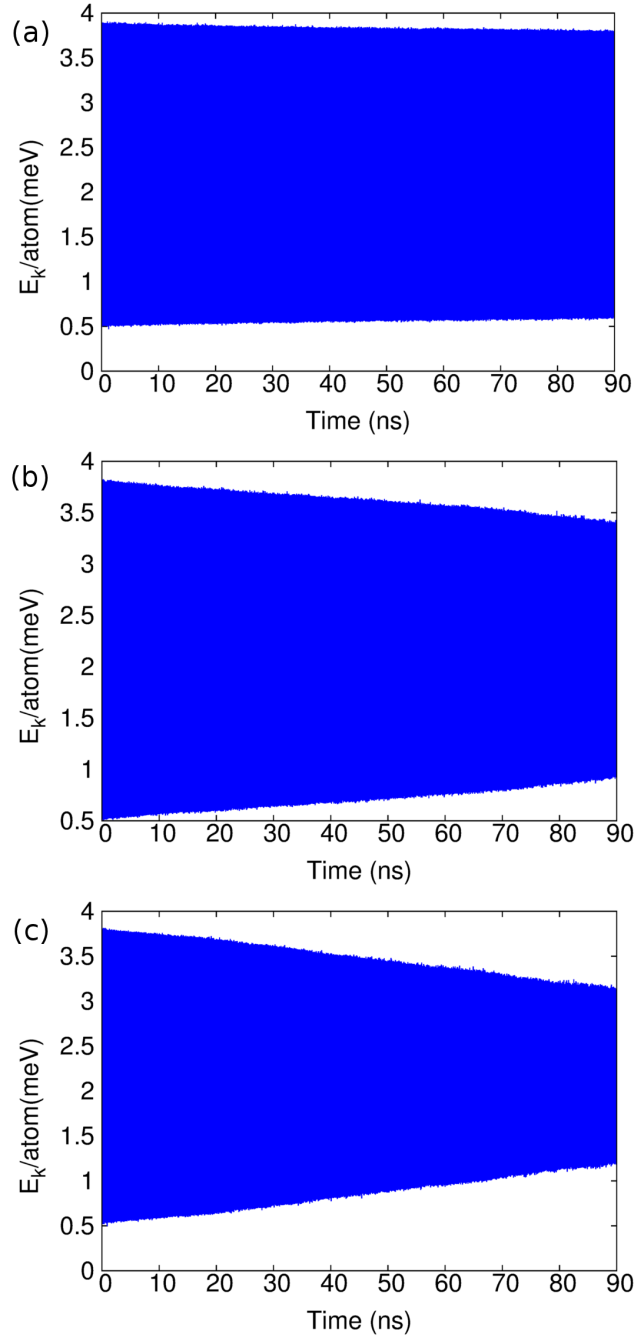


Figure 5.8: The kinetic energy per atom for zigzag SLBPRs at 4.2 K with different concentrations of SV defects: 0%, 1% and 2% from top to bottom. The Q-factors are 875950, 320000 and 162000, respectively.

5.3 Results and discussion

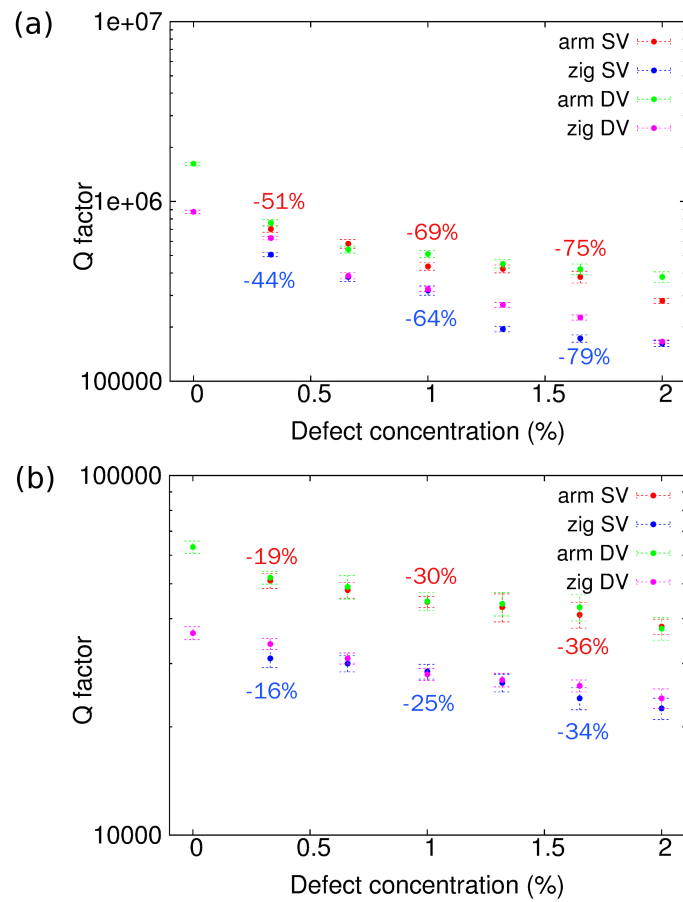


Figure 5.9: Defect (SV and DV) concentration dependence for the Q-factors of the SLBPRs along the armchair and zigzag directions at (a) 4.2 K and (b) 50 K. The percentage values show the reduction percentage.

5. MECHANICAL ENGINEERING FOR BLACK PHOSPHORUS NANORESONATORS

the considerable reduction of the Q-factor can be ascribed to the vacancy-induced asymmetry of the actuated oscillation, which has been found to strongly affect the Q-factors of the graphene nanomechanical resonators.⁵⁷ A small percentage of defects can cause strong asymmetry in the SLBPR, leading to the reduction of the Q-factor. The defect-induced asymmetry increases with the increasing defect concentration, so the reduction of the Q-factor is also increased. As shown in Fig. 5.9, the Q-factor is reduced by 82.7% in the armchair direction at 4.2 K with SV defect concentration of 2%.

Experiment studies have observed that long term exposure to ambient conditions results in a layer-by-layer etching process of BP flakes. Furthermore, it is possible for flakes to be etched down to a SLBP.³⁰² In this etching process, the atomic vacancy is one unavoidable etching manner, which shall be one possible reason for low Q-factors (around 100) measured for the phosphorene resonators in the recent experiment.³⁰

Line distribution of SV defects

Recently, it has been found that the distributed pattern of the atomic vacancies strongly affects the fracture strength and fracture strain.³⁰³ Thus, in addition to the randomly distributed SV defects, we have also investigated the effects of SV defects distributed in a line pattern on the SLBP. Fig. 5.10 (a) illustrates the uniformly line distribution of four SV defects, i.e. concentration of 0.65%, where the line pattern forms an angle α with respect to the oscillation direction. The Q-factors of the armchair and zigzag SLBPRs at 4.2 K with different tilt angles α are shown in Fig. 5.10 (b). It can be seen that the Q-factors of the SLBPRs show slight fluctuations with varying tilting angle α , which means that the distribution pattern of the vacancy defects is not important for the reduction of the Q-factor.

5.3.3.2 Oxidation effects

We now discuss the effects of oxidation on both armchair and zigzag SLBPRs. As we have noted above, the force constant parameter K for the angles $\angle 712$, $\angle 713$ and $\angle 714$, is treated as a simulation parameter here, because there is no available value. We have used $K = 15$ and 45 eV/rad^2 in the present work, as these values are on the same order as the force constant for the bond stretching.

Fig. 5.11 shows the defect concentration dependence for the Q-factors of the SLBPRs at 4.2 K and 50 K, respectively. It shows that the value of the parameter K for the angle bending is not important here. The Q-factor is reduced significantly with the increase of the percentage. For the concentration of 2%, the Q-factor is reduced by about 67.8%

5.3 Results and discussion

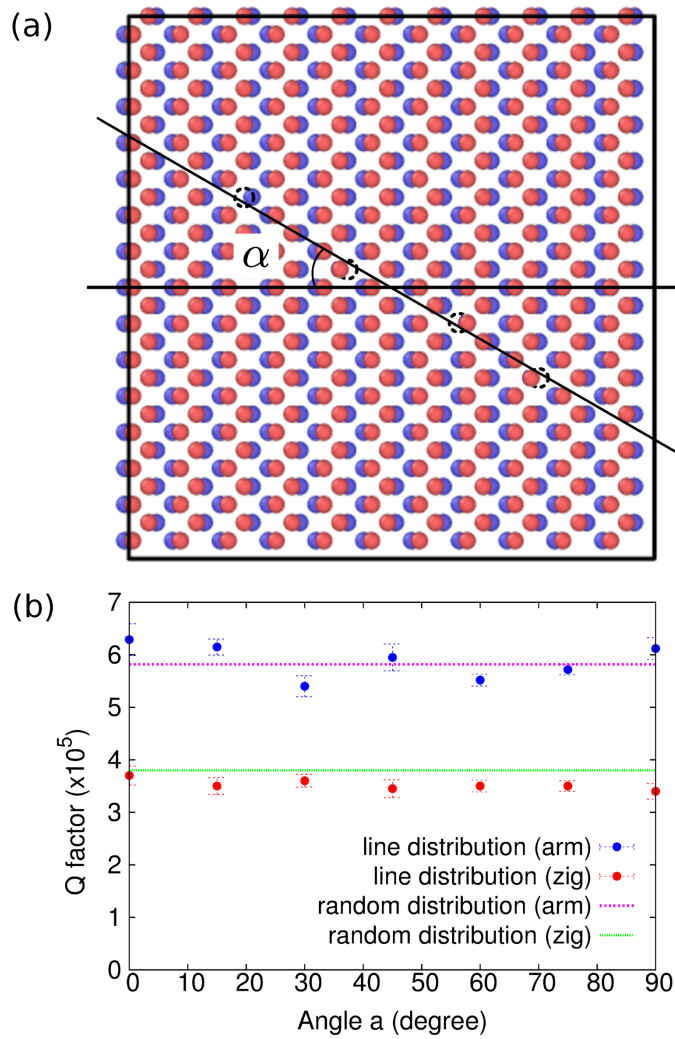


Figure 5.10: The dependence of the Q-factor on the pattern of the vacancy defect. (a) The SLBP containing four SV defects (dashed circle) patterned in a line with a tilt angle α with respect to the oscillation direction. (b) The Q-factors of the SLBPRs along the armchair and zigzag directions at 4.2 K with different α .

5. MECHANICAL ENGINEERING FOR BLACK PHOSPHORUS NANORESONATORS

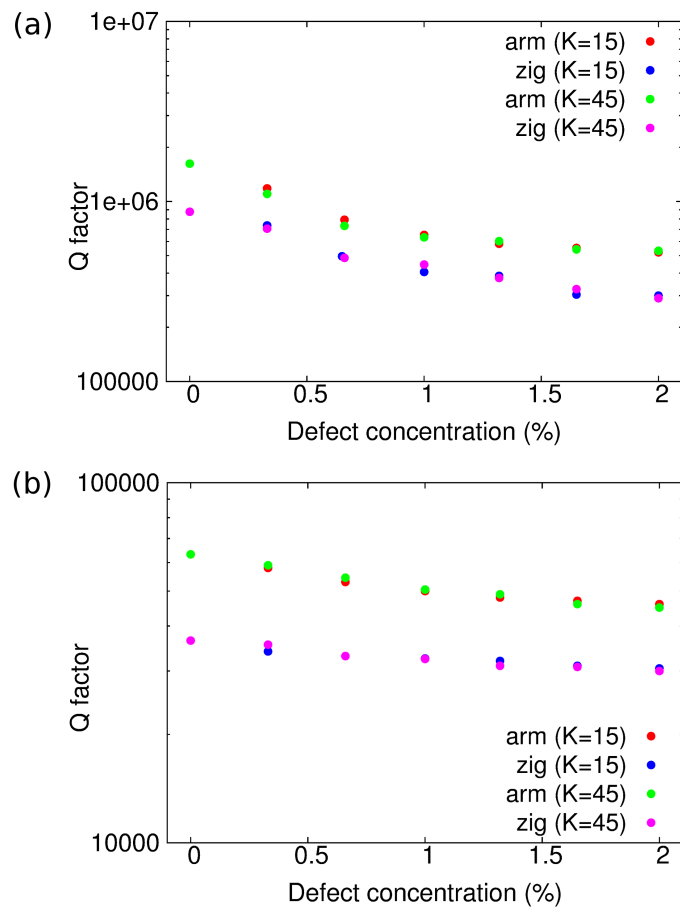


Figure 5.11: Oxidized defect concentration dependence for the Q-factors of the arm-chair and zigzag SLBPRs at (a) 4.2 K and (b) 50 K.

5.4 Conclusion

and 70% in the armchair and zigzag directions, respectively, at 4.2 K, while 27.3% and 16.3%, respectively, at 50 K. The oxidation effects become weaker at the higher temperature.

5.3.3.3 Comparison

Based on the above results, we can find that the oxidation effect is weaker than vacancy effect on the Q-factors of the SLBPRs. In addition, the vacancy defect-induced reduction for the Q-factor is almost isotropic, as shown in Figs. 5.9 and 5.10. The difference between the armchair and zigzag resonators is from the chirality effect, which exists even in the undefected system. Similarly, the oxidation effect does also not show obvious anisotropy.

The weaker reduction effect (of both of vacancy and oxidation) at higher temperature can be mainly attributed to the stronger thermal fluctuation of atoms at higher temperature. More specifically, at lower temperature, the reduction of the Q-factor is mainly due to the vacancy induced asymmetry of the actuated oscillation, which has been found to strongly affect the Q-factors of the graphene nanomechanical resonators.⁵⁷ However, at higher temperature, the reduction is mainly attributed to stronger thermal vibrations. Thus, the reduction effect is weaker at higher temperature as shown in Fig. 5.9 and Fig. 5.11.

Defects can cause some localized vibrations, which can reduce the Q factor. The mass of phosphorus atom is much larger than that of oxygen atom, so the localized vibrations induced by vacancy (formed by removing phosphorus atom) can localize more energy than the oxidation (formed by adding oxygen atom). The oxidation effect is thus weaker than the vacancy effect on the SLBPRs.

5.4 Conclusion

In conclusion, we have performed classical MD simulations to study the effects of mechanical tension, vacancy and oxidized defects on the SLBPR. We find that intrinsically the Q-factors for the armchair SLBPRs are generally higher than those for the zigzag SLBPRs, and are also larger than those found previously for graphene and MoS₂ nanoresonators. When the effects of mechanical strain are considered, our key finding is that there is a maximum point in the strain dependence of the Q-factor due to the competition between the enhancement at small strains and the reduction due to nonlinear effects at large strains. Furthermore, we find that defects can cause a sig-

5. MECHANICAL ENGINEERING FOR BLACK PHOSPHORUS NANORESONATORS

nificant degradation of the Q-factor of the SLBPR. In particular, a 2% concentration of randomly distributed SV defects is able to reduce the Q-factor by about 80% and 40% for the SLBPRs at 4.2 K and 50 K, respectively. The DV defects have the similar reduction as the SV in the Q-factors of the SLBPRs. We also find that the Q-factor is not sensitive to the distributed pattern of the vacancy defects. Finally, it is found that oxidation has a weaker reduction on the Q-factor of the SLBPR, as compared with the vacancy defects.

Chapter 6

Self-assembly of Water Molecules Using Graphene Nanoresonators

6.1 Introduction

Graphene is a monolayer of carbon atoms in the honeycomb lattice structure, and has attracted much attention since its discovery.^{60,61} It is an attractive platform for NEMS^{62,63} due to its atomic thickness, low mass density, high stiffness and high surface area.^{64,65} Several recent works have shown that GNMR is a promising candidate for ultrasensitive mass sensing and detection.^{62,66} The Q-factors, and thus sensitivity to external perturbations like mass and pressure, are limited by both extrinsic and intrinsic energy dissipation mechanisms, including attachment induced energy loss,^{67,68} nonlinear scattering mechanisms,⁶⁹ edge effects,⁷⁰ the effective strain mechanism⁷¹ and thermalization due to nonlinear mode coupling.⁷²

The interplay between graphene and adsorbates has been investigated in many works. It was experimentally shown that pristine graphene sheets are impermeable to standard gases, including helium.^{63,73} The adsorption of Helium atoms on graphene has also discussed,^{74,75,76} while Jiang et al. studied the adsorption effects of metal atoms on the Q-factors of graphene resonators.⁷¹ Very recently, an experiment showed that metal atoms can be used as molecular valves to control the gas flux through pores in monolayer graphene.⁷⁷ However, an important issue that has not been investigated is whether it is possible to self-assemble adsorbates on the graphene surface into different types of nanostructures.

In this chapter, we report classical MD simulations for the self-assembly of water

6. SELF-ASSEMBLY OF WATER MOLECULES USING GRAPHENE NANORESONATORS

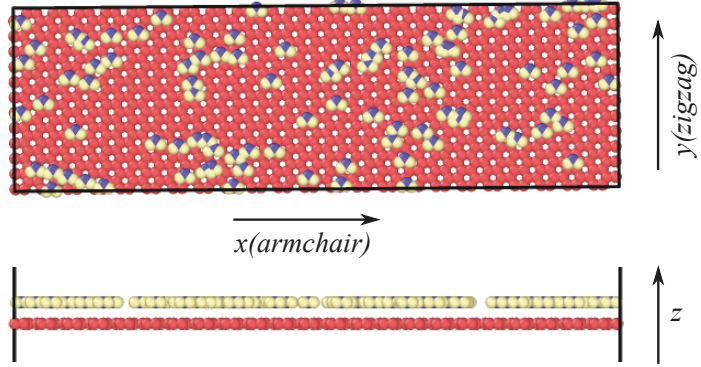


Figure 6.1: Configuration for the GNMR. Water molecules are randomly distributed on the graphene sheet (red atoms) of dimensions $100 * 30 \text{ \AA}$.

molecules on the surface of graphene nanoresonators. In doing so, we draw inspiration from the classical macroscale Chladni plate resonators, in which higher order resonant modes are used to self-assemble adsorbates on the plate surface into different configurations.^{304,305} We observe that the location for the self-assembly depends on the resonant frequency. Specifically, water molecules will assemble at the position with the maximum amplitude when the resonant frequency is lower than a critical frequency, which is determined by the interaction between graphene and water molecules. Otherwise, the assembly will take place at the position with minimum oscillation amplitude if the resonant frequency is higher than the critical frequency. We also analyze the hydrogen bonds for the water chains that are assembled by the graphene nanoresonators.

Our present work has revealed that it is possible for water molecules to assemble into water chains using graphene nanoresonators, which may have important implications for directed transport and ultra low friction-aided³⁰⁶ advanced nanoscale conductance systems.³⁰⁷ For example, Chen et al.³⁰⁷ reported a water bridge under electric field can serve as a transport system, with potential applications in drug delivery. Water chains have also been created through confinement in carbon nanotubes. However, the radial size of the nanotubes limits the chain size, while also inducing water layering effects due to nanoconfinement, which may impact the fluid transport. Thus, assembling water chains via oscillating graphene surfaces may help to realize structurally flexible water channels in nanofluidics.

6.2 Structure and simulation details

Fig. 6.1 shows the structure of the GNMR simulated in the present work, which is a monolayer and has dimensions $100 * 30 \text{ \AA}$. All MD simulations were performed using the publicly available simulation code LAMMPS²³⁰, while the OVITO package was used for visualization²⁹⁹. The interaction among carbon atoms is described by the second generation Brenner (REBO-II)³⁰⁸ potential, which is parameterized for carbon and/or hydrogen atoms. In the REBO-II force field, the total potential energy of a system is given by

$$E = \sum_i \sum_{j(>i)} [E_R(r_{ij}) - \bar{b}_{ij}E_A(r_{ij})], \quad (6.1)$$

where E_R and E_A are the repulsive and attractive interactions, respectively. r_{ij} is the distance between two adjacent atoms i and j , and \bar{b}_{ij} is a many-bond empirical bond-order term. The water molecules are described by the rigid SPC/E model.^{309,310} The SHAKE algorithm implemented in LAMMPS was applied to freeze the high-frequency vibrations between oxygen and hydrogen atoms. The coupling between water molecules and graphene is represented by the interaction between oxygen atoms and graphene, which is described by the following Lennard-Jones (LJ) potential

$$U(r) = 4\epsilon \left[\left(\frac{\sigma}{r} \right)^{12} - \left(\frac{\sigma}{r} \right)^6 \right], \quad (6.2)$$

with parameters $\sigma_{C-O} = 3.19 \text{ \AA}$ and $\epsilon_{C-O} = 4.063 \text{ meV}$.³¹¹ The interaction among water molecules is also described by the LJ potential with $\sigma_{O-O} = 3.166 \text{ \AA}$, $\epsilon_{O-O} = 6.737 \text{ meV}$.³¹² We find from the literature that the scanning electron microscope (SEM) is normally used to perform measurements on resonators,^{313,314,315} which may help to study how water interacts with graphene nanoresonators. For the OH stretching, the potential energy associating with the OH stretching is one order higher than the interaction between water and graphene. Hence, the OH stretching motion is much weaker than the motion of the whole water molecular, so the water molecular is regarded as a rigid molecular by ignoring the OH stretching (which is a usual technique for the simulation of water). The standard Newton equations of motion are integrated in time using the velocity Verlet algorithm with a time step of 1 fs.

6. SELF-ASSEMBLY OF WATER MOLECULES USING GRAPHENE NANORESONATORS

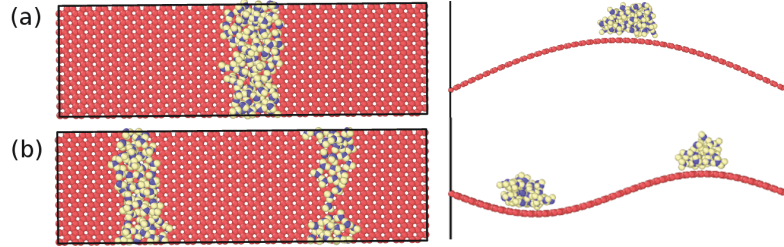


Figure 6.2: Self-assembly of water molecules by GNMRs. The resonant oscillations for mode indices $n = 1$ for panel (a) and $n = 2$ for panel (b). Water molecules are assembled at the positions with maximum amplitude.

6.3 Results and discussions

6.3.1 Assembly of water molecules

We first determine the resonant frequency for the GNMRs. Specifically, we actuate the resonant oscillation of the GNMR by adding a sine shaped velocity distribution to the z (out of plane) direction, i.e., $v_z = v_0 \sin(2\pi x/L)$, in which L is the length in the x -direction. A small value $v_0 = 0.2 \text{ \AA/ps}$ is used, so that nonlinear effects can be avoided. After the actuation, the GNMR is allowed to oscillate freely within the NVE (i.e., the particles number N , the volume V and the energy E of the system are constant) ensemble. The resonant frequency $f_2\pi = 0.065 \text{ THz}$ is extracted from the trajectory of the kinetic/potential energy per atom. From elasticity theory, the frequency of the vibrational mode $\sin(n \pm \pi x/L)$ with mode index n in the thin plate is proportional to n^2 . Our numerical results show that $f = 0.016 \pm n^2 \text{ THz}$.

We now discuss the assembly of water molecules by using the resonant oscillation of GNMRs. The enforced oscillation is generated in the GNMRs by driving displacement $A \pm \sin(\omega t) \sin(n \pm \pi x/L)$ for carbon atoms, with $A = 8 \text{ \AA}$ as the displacement amplitude. The angular frequency can be determined as $\omega = 2\pi f = 0.1 \pm n^2 \text{ THz}$. Water molecules are simulated within the NVT (i.e., the particles number N , the volume V and the temperature T of the system are constant) ensemble. At the beginning of the simulations, 100 and 120 water molecules are randomly distributed on the surfaces of the GNMRs for mode indices $n = 1$ and 2, respectively, as illustrated in Fig. 6.1. Fig. 6.2 shows the final stable structures at 300 K for mode indices $n = 1$ and 2, which shows obvious self-assembly of water molecules in both cases. As shown in Fig. 6.2, water molecules are assembled at $x = L/2$ for mode index $n = 1$, and at $x = L/4$ and $x = 3L/4$ for mode index $n = 2$, which indicates that water molecules are assembled at

6.3 Results and discussions

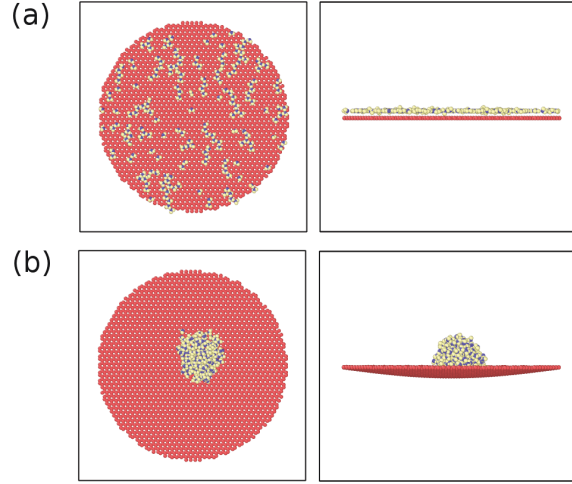


Figure 6.3: (a) Initial configuration for the circular GNMR, with radius 50 Å. (b) Water molecules are assembled at the center of the CGN.

the positions with maximum amplitude for mode indices $n = 1$ and 2.

The assembly of water molecules at positions with maximum oscillation amplitude can also be found in the graphene nanoresonator of circular (CGN) shape as shown in Fig. 6.3. For the CGN, the enforced oscillation is actuated in a similar way by pre-defining displacements $u_z = A \pm \sin(2\pi ft) \sin(0.5\pi(1 - (r/R)))$ for the carbon atoms, where R is the radius of the graphene resonator and r represents the distance away from the center of the resonator. Fig. 6.3 (a) shows the initial configuration of the CGN of $R = 50$ Å and 196 water molecules. Fig. 6.3 (b) shows that water molecules are assembled at the center of the CGN, where has the maximum oscillation amplitude.

6.3.2 Frequency effects on assembly

To examine possible frequency effects on the self-assembly phenomenon, we performed a set of simulations with different frequencies for the resonant oscillation mode index $n = 1$. More specifically, the intrinsic frequency for this mode is $f_\pi = 0.016$ THz. We simulated the self-assembly of water molecules using GNMRs with enforced frequencies of $3f_\pi$, $10f_\pi$, $30f_\pi$, $40f_\pi$, $50f_\pi$, $80f_\pi$ and $100f_\pi$. Fig. 6.4 shows the stable configurations of the systems corresponding to frequencies $10f_\pi$, $30f_\pi$, $80f_\pi$ and $100f_\pi$. While the self-assembly of water molecules can be found in all cases, it clearly shows that the locations of the water chains depend on the oscillation frequencies. The assembly happens at the positions with maximum oscillation amplitude for lower

6. SELF-ASSEMBLY OF WATER MOLECULES USING GRAPHENE NANORESONATORS

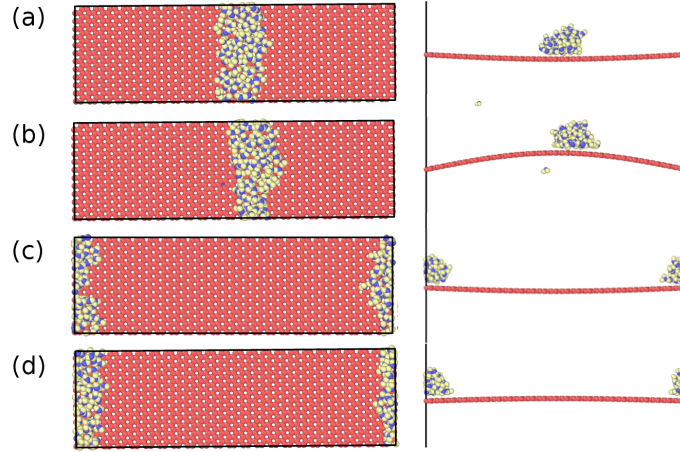


Figure 6.4: Frequency effects on the self-assembly of water molecules with mode index $n = 1$, with 4 different frequencies ($10f_\pi$, $30f_\pi$, $80f_\pi$ and $100f_\pi$ for panels from (a) to (d)).

oscillation frequencies $10f_\pi$ and $30f_\pi$, while the water chains are assembled at the two boundaries (with minimum oscillation amplitude) for higher oscillation frequencies $80f_\pi$ and $100f_\pi$. Fig. 6.5 summarizes the frequency dependence for the assembly position. There is a step-like jump at a critical frequency around $f_c = 35f_\pi$. Water molecules are assembled at the positions with the maximum (minimum) oscillation amplitude, corresponding to frequencies lower (higher) than the critical frequency.

To understand the frequency dependent self-assembly, we explore two characteristic frequencies for the resonant oscillation process. The first frequency (f_g) is the resonant oscillation frequency for the GNMR, which has already been discussed. The second frequency (f_{wg}) characterizes the oscillation between the water clusters and graphene. The value of f_{wg} is determined by the van der Waals interaction between water molecules and graphene. If the resonant frequency for graphene (f_g) is lower than the frequency f_{wg} , then water molecules are able to follow the resonant motion of the GNMR. As a result, water molecules are always connected to the GNMR through the van der Waals interactions during the oscillation process.

According to the previous reference,³⁰⁶ water molecules prefer to stay on surfaces with larger curvature. As a result, Fig. 6.6 shows that the water cluster slides down quickly to the position with maximum amplitude if the GNMR oscillation is below its equilibrium (flat) configuration. If the GNMR oscillation is above the flat configuration, the water cluster should move to the two ends, where the curvature is larger. It should be noted that the curvature is negative for the GNMR when it is above the

6.3 Results and discussions

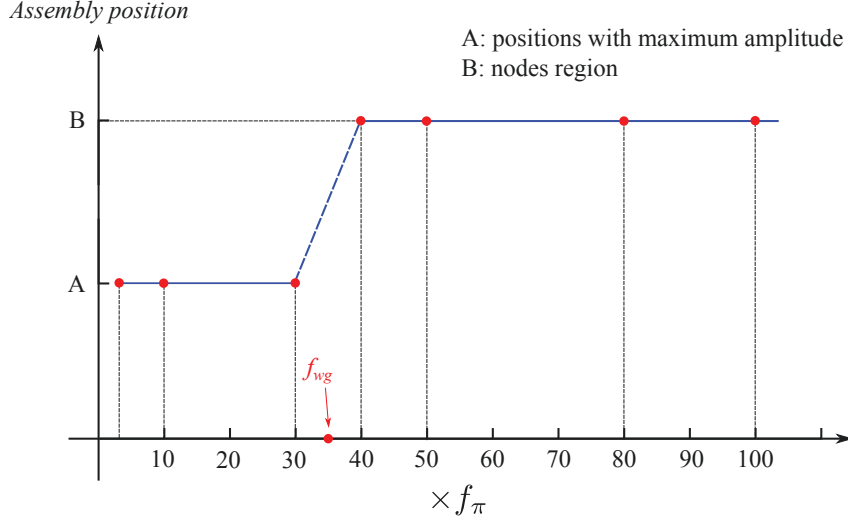


Figure 6.5: Assembly position versus frequency for mode index $n = 1$.

equilibrium (flat) configuration as shown on the right part of Fig. 6.6. However, the sliding velocity of the water cluster is fairly small when the GNMR oscillation is above its equilibrium (flat) configuration. As a result, the water cluster oscillates around the middle of the GNMR with the maximum oscillation amplitude. However, if the resonant frequency for the GNMR (f_g) is higher than the frequency f_{wg} , then water molecules can escape from the van der Waals interactions from graphene and search for the most stable positions of the GNMR, leading to possible self-assembly of water chains at the nodal positions of the GNMR.

We now derive the frequency f_{wg} corresponding to the van der Waals interaction between water molecules and graphene. Assuming a small variation dr in the distance r , the retracting force constant can be obtained by

$$K = \frac{\partial^2 U}{\partial r^2} = 0.023 \text{ eV}/\text{\AA}^2. \quad (6.3)$$

The frequency for water molecules is

$$f_{wg} = \frac{1}{2\pi} * \sqrt{\frac{K}{m}} \rightarrow 0.567 \text{ THz}. \quad (6.4)$$

This analytic value for the critical frequency agrees quite well with the numerical results shown in Fig. 6.5, in which the numerical value for the critical frequency is about $35f_\pi \rightarrow 0.56 \text{ THz}$.

It is expected that the graphene liquid cell electron microscopy or the cryo-TEM technique can be applied to directly visualize the assembled water pattern on graphene

6. SELF-ASSEMBLY OF WATER MOLECULES USING GRAPHENE NANORESONATORS

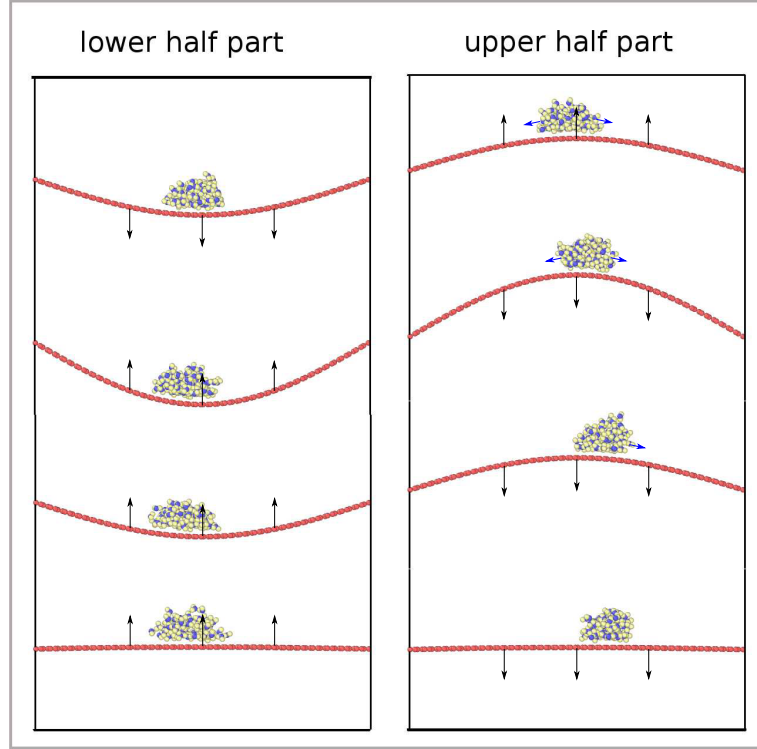


Figure 6.6: The motion of a self-assembled water cluster during one oscillation cycle, with $f_g < f_{wg}$.

film, which can provide direct experimental supports for our simulation results in the present work.

6.3.3 H-bonds

Quantifying the characteristics of the hydrogen (H)-bonding is useful for capturing important physical properties for water chains.^{316,317,318,319} Therefore, we calculate the average number of H-bonds per water molecule in the water chains that are assembled with different resonant frequencies. The H-bond is defined using the geometric criteria,³¹⁶ which states that a H-bond between two water molecules is formed if $r_{O-O} < 0.3$ nm and $\angle_{OOH} < 30^\circ$. Fig. 6.7 shows that the highest value of the H-bonds number is about 3.3 for $100f_\pi$, which indicates that the water chain is spatially stable. This number is slightly smaller than 3.7 for bulk water due to the presence of surface effects on the formed water chains. The small value of the H-bonds number at the

6.4 Conclusion

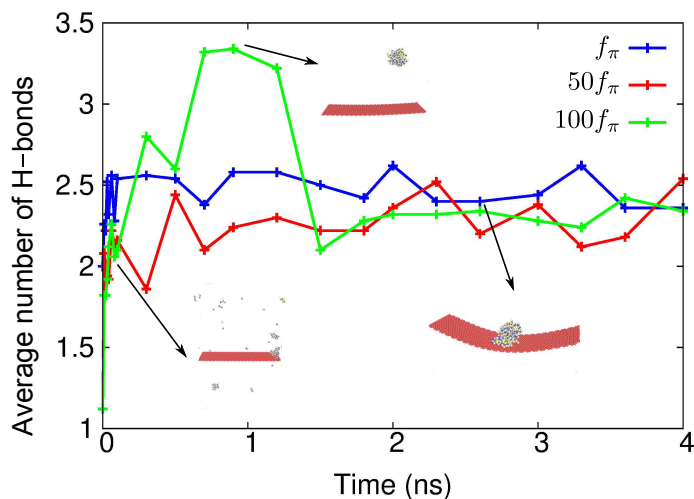


Figure 6.7: Frequency effects on H-bonds.

beginning of the assembly process is because many water molecules are spatially distributed at the beginning of the simulation. The number of the H-bonds increases and reaches a saturation value of 2.3, when a stable water chain is assembled. It is quite interesting that the saturation values for the number of the H-bonds are almost the same for all water chains, which are assembled using different oscillation frequencies for the GNMR. This result implies similar structural properties for these water chains.

6.4 Conclusion

In conclusion, we have demonstrated, using classical MD simulations, the possibility of creating self-assembled water nanostructures by using normal resonant mode shapes of graphene nanoresonators. In doing so, we have drawn inspiration from macroscale Chladni plate resonators, which are used to self-assemble shapes using higher order mode frequencies. We have uncovered that the location of the self-assembly can be controlled through the resonant frequency. Water molecules will assemble at the positions with maximum amplitude if the resonant frequency is lower than a critical value. Otherwise, the assembly occurs at the nodes of the resonator, when the resonant frequency is higher than the critical value. We provide an analytic formula for the critical resonant frequency based on the interaction between water molecules and graphene. Furthermore, we demonstrate that the water chains assembled by the graphene nanoresonators have some universal properties including a stable value for

6. SELF-ASSEMBLY OF WATER MOLECULES USING GRAPHENE NANORESONATORS

the number of H-bonds.

Chapter 7

Conclusions

7.1 Summary of achievements

This dissertation was devoted to the development of the CG models for SLMoS₂, mechanism understanding of BP nanomechanical resonators, and application of graphene nanoresonators. Considering to compare the theoretical studies with experimental researches with larger sizes, the CG model proposed in current work provides a valuable simulation approach for Q2D materials. As introduced in the first chapter, Q2D materials have attracted intensive research interest due to their novel properties during the past decades. However, the dynamic characteristics of these nanoresonators is still lacking. Therefore, the results about the dynamic characteristics of Q2D materials based nanoresonators in current work provide a useful reference. From the work that has been done, the achievements are summarized as follows:

1. Method development

- A 2D CG model of MoS₂ with SW potential is parametrized, in which all SW geometrical parameters are determined analytically from the equilibrium condition for each potential term, while the SW energy parameters are derived analytically based on the VFF model. This parametrization method transfers the accuracy of the VFF model to the SW potential. Owing to its simplicity, the 2D CG model is used to investigate the adsorption effects on the resonant frequency. The resonant frequency of the oscillation is found to be insensitive to the adsorbed mass.

7. CONCLUSIONS

- The folding of MoS₂ is investigated using 1D CG simulations, in which all the parameters are determined analytically from the SW atomic potential. Owing to its simplicity, the 1D CG model is used to derive analytic predictions for the relaxed configuration of the folded MoS₂ and the resonant frequency for the breathing-like oscillation. Two interesting phenomena for the breathing-like oscillation in the folded MoS₂ are disclosed. First, the breathing-like oscillation is self-actuated, since this oscillation can be actuated by intrinsic thermal vibrations without any external actuation force. Second, the resonant frequency of the breathing-like oscillation is insensitive to the adsorption effect. These two features enable practical applications of the folded MoS₂ based nanoresonators, where stable resonant oscillations are desirable.

2. Mechanism understanding

- The resonant frequency of BPRs is highly anisotropic in the BP due to its intrinsic puckered configuration, and the Q-factor in the armchair direction is higher than that in the zigzag direction at the room temperature. The Q-factors are also found to be intrinsically larger than those of graphene and MoS₂ nanoresonators.
- The Q-factors can be increased by more than a factor of two by applying tensile strain, with uniaxial strain in the armchair direction being most effective. However, there is an upper bound for the Q-factor increase due to nonlinear effects at large strains, after which the Q-factor decreases. The tension induced nonlinear effect is stronger along the zigzag direction, resulting in a smaller maximum strain for Q-factor enhancement.
- For the effects of vacancy and oxidation on the BPRs at different temperatures, the vacancy causes strong reduction in the Q-factors of the nanoresonators, while the oxidation has weaker effect. More specifically, a 2% concentration of randomly distributed SV defects is able to reduce the Q-factor by about 80% and 40% at 4.2K and 50K, respectively. The Q-factor of the nanoresonator is not sensitive to the distribution pattern of the vacancy defects.

3. Application

- By drawing inspiration from macroscale self-assembly using the higher order resonant modes of Chladni plates, using classical MD simulations, the possibility of creating self-assembled water nanostructures by using normal resonant mode shapes of graphene nanoresonators is demonstrated and thus a novel application for graphene resonators, to use them to self-assemble

7.2 Outlook

small nanostructures, is proposed. The location of the self-assembly can be controlled through the resonant frequency. Specifically, water molecules will assemble at the positions with maximum amplitude if the resonant frequency is lower than a critical value. Otherwise, the assembly occurs at the nodes of the resonator, when the resonant frequency is higher than the critical value. An analytic formula for the critical resonant frequency based on the interaction between water molecules and graphene is provided. Furthermore, the water chains assembled by the graphene nanoresonators have been demonstrated to exist some universal properties including a stable value for the number of H-bonds.

7.2 Outlook

The presented work mainly investigated the dynamic characteristics of Q2D materials based nanoresonators. A few possible extensions to the current work can be suggested as follows:

- ~ The factors that degrade the Q-factor can be categorized as extrinsic and intrinsic. Extrinsic damping mechanisms occur due to the interaction of the NEMS resonator with its surrounding environment, e.g. the substrate on which the NEMS lies, or the air or gas molecules surrounding the NEMS. Intrinsic damping mechanisms occur due to defects or flaws inherent in the NEMS, for instance, atomic vacancies, grain boundaries, impurities, etc. Thus, the investigation of such factor effects on energy dissipation is necessary to study the dynamic characterization of Q2D materials based nanoresonators.
- ~ The 2D CG model proposed in the current work is mainly used to examine the properties of MoS₂ nanoresonators. However, this 2D CG model is also able to be applied in the practical problems, such as fracture growth for the SLMoS₂, which would make a significant sense.

References

- [1] Harold G Craighead. Nanoelectromechanical systems. *Science*, 290(5496):1532–1535, 2000. [1](#), [2](#), [24](#)
- [2] Michael Roukes. Nanoelectromechanical systems face the future. *Physics World*, 14(2):25, 2001. [1](#), [14](#)
- [3] YT Yang, Carlo Callegari, XL Feng, KL Ekinici, and ML Roukes. Zeptogram-scale nanomechanical mass sensing. *Nano letters*, 6(4):583–586, 2006. [1](#), [2](#), [8](#)
- [4] Robert L Badzey and Pritiraj Mohanty. Coherent signal amplification in bistable nanomechanical oscillators by stochastic resonance. *Nature*, 437(7061):995–998, 2005. [1](#)
- [5] R Budakian, HJ Mamin, and D Rugar. Spin manipulation using fast cantilever phase reversals. *Applied physics letters*, 89(11):113113, 2006. [1](#), [2](#)
- [6] Aaron D OConnell, Max Hofheinz, Markus Ansmann, Radoslaw C Bialczak, Mike Lenander, Erik Lucero, Matthew Neeley, Daniel Sank, H Wang, M Weides, et al. Quantum ground state and single-phonon control of a mechanical resonator. *Nature*, 464(7289):697–703, 2010. [1](#), [2](#)
- [7] Thomas P Burg, Michel Godin, Scott M Knudsen, Wenjiang Shen, Greg Carlson, John S Foster, Ken Babcock, and Scott R Manalis. Weighing of biomolecules, single cells and single nanoparticles in fluid. *nature*, 446(7139):1066–1069, 2007. [1](#), [2](#)
- [8] Seung-Bo Shim, Matthias Imboden, and Pritiraj Mohanty. Synchronized oscillation in coupled nanomechanical oscillators. *Science*, 316(5821):95–99, 2007. [1](#)

REFERENCES

- [9] KL Ekinici. Electromechanical transducers at the nanoscale: actuation and sensing of motion in nanoelectromechanical systems (nems). *small*, 1(8-9):786–797, 2005. 1, 7
- [10] XMH Huang, XL Feng, CA Zorman, M Mehregany, and ML Roukes. Vhf, uhf and microwave frequency nanomechanical resonators some preliminary results to those described herein were presented at the transducers’ 03 conference. *New Journal of Physics*, 7(1):247, 2005. 1, 7
- [11] Thomas Braun, Viola Barwich, Murali Krishna Ghatkesar, Adriaan H Bredekamp, Christoph Gerber, Martin Hegner, and Hans Peter Lang. Micromechanical mass sensors for biomolecular detection in a physiological environment. *Physical Review E*, 72(3):031907, 2005. 1, 8
- [12] Mo Li, Hong X Tang, and Michael L Roukes. Ultra-sensitive nems-based cantilevers for sensing, scanned probe and very high-frequency applications. *Nature nanotechnology*, 2(2):114–120, 2007. 2, 7
- [13] P Alex Greaney and Jeffrey C Grossman. Nanomechanical resonance spectroscopy: a novel route to ultrasensitive label-free detection. *Nano letters*, 8(9):2648–2652, 2008. 2
- [14] AK Naik, MS Hanay, WK Hiebert, XL Feng, and ML Roukes. Towards single-molecule nanomechanical mass spectrometry. *Nature nanotechnology*, 4(7):445–450, 2009. 2
- [15] Tae Yun Kwon, Kilho Eom, Jae Hong Park, Dae Sung Yoon, Tae Song Kim, and Hong Lim Lee. In situ real-time monitoring of biomolecular interactions based on resonating microcantilevers immersed in a viscous fluid. *Applied Physics Letters*, 90(22):223903, 2007. 2
- [16] Philip S Waggoner and Harold G Craighead. Micro-and nanomechanical sensors for environmental, chemical, and biological detection. *Lab on a Chip*, 7(10):1238–1255, 2007. 2
- [17] Angelica P Davila, Jaesung Jang, Amit K Gupta, Tom Walter, Arthur Aronson, and Rashid Bashir. Microresonator mass sensors for detection of bacillus anthracis spores in air and water. *Biosensors and Bioelectronics*, 22(12):3028–3035, 2007. 2
- [18] James R Heath and Mark E Davis. Nanotechnology and cancer. *Annu. Rev. Med.*, 59:251–265, 2008. 2

REFERENCES

- [19] Guanghua Wu, Ram H Datar, Karolyn M Hansen, Thomas Thundat, Richard J Cote, and Arun Majumdar. Bioassay of prostate-specific antigen (psa) using microcantilevers. *Nature biotechnology*, 19(9):856–860, 2001. 2, 8
- [20] B Ilic, Y Yang, K Aubin, R Reichenbach, S Krylov, and HG Craighead. Enumeration of dna molecules bound to a nanomechanical oscillator. *Nano Letters*, 5(5):925–929, 2005. 2, 8
- [21] Jin-Wu Jiang. Graphene versus mos2: A short review. *Frontiers of Physics*, 10(3):287–302, 2015. 2, 19, 22, 25, 31, 32
- [22] Allan Brown and Stig Rundqvist. Refinement of the crystal structure of black phosphorus. *Acta Crystallographica*, 19(4):684–685, 1965. 3, 25, 69
- [23] Yanlan Du, Chuying Ouyang, Siqi Shi, and Minsheng Lei. Ab initio studies on atomic and electronic structures of black phosphorus. *Journal of Applied Physics*, 107(9):093718, 2010. 3, 20, 29, 69
- [24] AS Rodin, A Carvalho, and AH Castro Neto. Strain-induced gap modification in black phosphorus. *Physical review letters*, 112(17):176801, 2014. 3, 20, 29, 69
- [25] Tony Low, AS Rodin, A Carvalho, Yongjin Jiang, Han Wang, Fengnian Xia, and AH Castro Neto. Tunable optical properties of multilayers black phosphorus. arxiv preprint. *arXiv preprint arXiv:1404.4030*, 2014. 3, 20, 69
- [26] Michael Engel, Mathias Steiner, and Phaedon Avouris. Black phosphorus photodetector for multispectral, high-resolution imaging. *Nano letters*, 14(11):6414–6417, 2014. 3, 20, 69
- [27] Likai Li, Yijun Yu, Guo Jun Ye, Qingqin Ge, Xuedong Ou, Hua Wu, Donglai Feng, Xian Hui Chen, and Yuanbo Zhang. Black phosphorus field-effect transistors. 9(5):372–377, 2014. 3, 28, 69
- [28] Han Liu, Adam T. Neal, Zhen Zhu, David Tomnek, and Peide D. Ye. Phosphorene: A new 2d material with high carrier mobility. 8:4033–4041, 2014. 3, 28, 69
- [29] Michele Buscema, Dirk J. Groenendijk, Sofya I. Blanter, Gary A. Steele, Herre S.J. van der Zant, and Andres Castellanos-Gomez. Fast and broadband photoresponse of few-layer black phosphorus field-effect transistors. *Preprint at <http://arxiv.org/abs/1403.0565v1>*, 2014. 3, 28, 69

REFERENCES

- [30] Zenghui Wang, Hao Jia, Xuqian Zheng, Rui Yang, Zefang Wang, GJ Ye, XH Chen, Jie Shan, and Philip X-L Feng. Black phosphorus nanoelectromechanical resonators vibrating at very high frequencies. *Nanoscale*, 7(3):877–884, 2015. [3](#), [28](#), [69](#), [77](#), [84](#)
- [31] Qun Wei and Xihong Peng. Superior mechanical flexibility of phosphorene and few-layer black phosphorus. 104:251915, 2014. [3](#), [69](#)
- [32] Ruixiang Fei and Li Yang. Lattice vibrational modes and raman scattering spectra of strained phosphorene. 105(8):083120, 2014. [3](#), [69](#)
- [33] Zhun-Yong Ong, Yongqing Cai, Gang Zhang, and Yong-Wei Zhang. Strong thermal transport anisotropy and strain modulation in single-layer phosphorene. 118(43):25272–25277, 2014. [3](#), [69](#)
- [34] Baisheng Sa, Yan-Ling Li, Jingshan Qi, Rajeev Ahuja, and Zhimei Sun. Strain engineering for phosphorene: The potential application as a photocatalyst. 118(46):26560–26568, 2014. [3](#), [69](#)
- [35] Liangzhi Kou, Yandong Ma, Sean C. Smith, and Changfeng Chen. Anisotropic ripple deformation in phosphorene. *Preprint at <http://arxiv.org/abs/1412.7602v1>*. [3](#), [69](#)
- [36] H. Y. Lv, W. J. Lu, D. F. Shao, and Y. P. Sun. Enhanced thermoelectric performance of phosphorene by strain-induced band convergence. 90:085433, 2014. [3](#), [69](#)
- [37] Jin-Wu Jiang and Harold S Park. Negative poisson’s ratio in single-layer black phosphorus. 5:4727, 2014. [v](#), [3](#), [25](#), [26](#), [27](#), [28](#), [69](#)
- [38] Yongqing Cai, Qingqing Ke, Gang Zhang, Yuan Ping Feng, Vivek B Shenoy, and Yong-Wei Zhang. Giant phononic anisotropy and unusual anharmonicity of phosphorene: Interlayer coupling and strain engineering. *Preprint at <http://arxiv.org/abs/1502.00375>*, 2015. [3](#), [69](#)
- [39] A. S. Rodin, A. Carvalho, and A. H. Castro Neto. Strain-induced gap modification in black phosphorus. 112:176801, 2014. [3](#), [29](#), [69](#)
- [40] Xiaoyu Han, Henry Morgan Stewart, Stephen A. Shevlin, C. Richard A. Catlow, and Zheng Xiao Guo. Strain and orientation modulated bandgaps and effective masses of phosphorene nanoribbons. 14(8):4607–4614, 2014. [3](#), [69](#)
- [41] Guangzhao Qin, Zhenzhen Qin, Sheng-Ying Yue, Hui-Juan Cui, Qing-Rong Zheng, Qing-Bo Yan, and Gang Su. Strain modulated anisotropic geometric,

REFERENCES

- electronic and thermoelectric properties of black phosphorus. *arXiv:1406.0261*, 2014. 3, 69
- [42] G. Q. Huang and Z. W. Xing. Semiconductor to metal transition, dynamical stability and superconductivity of strained phosphorene. *Preprint at <http://arxiv.org/abs/1409.7284v1>*, 2014. 3, 69
- [43] Zenghui Wang, Hao Jia, Xu-Qian Zheng, Rui Yang, Guojun Ye, Xianhui Chen, and Philip X-L Feng. Resolving and tuning mechanical anisotropy in black phosphorus via nanomechanical multimode resonance spectromicroscopy. *Nano Letters*, 2016. 3, 4, 28, 70
- [44] Likai Li, Yijun Yu, Guo Jun Ye, Qingqin Ge, Xuedong Ou, Hua Wu, Donglai Feng, Xian Hui Chen, and Yuanbo Zhang. Black phosphorus field-effect transistors. *Nature nanotechnology*, 9(5):372–377, 2014. 4, 69
- [45] Han Liu, Adam T Neal, Zhen Zhu, David Tomanek, and Peide D Ye. Phosphorene: a new 2d material with high carrier mobility. *arXiv preprint [arXiv:1401.4133](http://arxiv.org/abs/1401.4133)*, 2014. 4, 29, 69
- [46] Fengnian Xia, Han Wang, and Yichen Jia. Rediscovering black phosphorus as an anisotropic layered material for optoelectronics and electronics. *Nature communications*, 5, 2014. 4, 69
- [47] CD Zhang, JC Lian, W Yi, YH Jiang, LW Liu, H Hu, WD Xiao, SX Du, LL Sun, and HJ Gao. Surface structures of black phosphorus investigated with scanning tunneling microscopy. *The Journal of Physical Chemistry C*, 113(43):18823–18826, 2009. 4, 69
- [48] Mamoru Baba, Fukunori Izumida, Yuji Takeda, and Akira Morita. Preparation of black phosphorus single crystals by a completely closed bismuth-flux method and their crystal morphology. *Japanese Journal of Applied Physics*, 28(6R):1019, 1989. 4, 69
- [49] Wei Hu and Jinlong Yang. Defects in phosphorene. *The Journal of Physical Chemistry C*, 119(35):20474–20480, 2015. 4, 70, 71
- [50] Junfeng Zhang and Jijun Zhao. Structures and electronic properties of symmetric and nonsymmetric graphene grain boundaries. *Carbon*, 55:151–159, 2013. 4, 70
- [51] Yongqing Cai, Qingqing Ke, Gang Zhang, Boris I Yakobson, and Yong-Wei Zhang. Highly itinerant atomic vacancies in phosphorene. *Journal of the American Chemical Society*, 138(32):10199–10206, 2016. 4, 70

REFERENCES

- [52] Angelo Ziletti, A Carvalho, David K Campbell, David F Coker, and AH Castro Neto. Oxygen defects in phosphorene. *Physical review letters*, 114(4):046801, 2015. [4](#), [70](#)
- [53] Jooheon Kang, Joshua D Wood, Spencer A Wells, Jae-Hyeok Lee, Xiaolong Liu, Kan-Sheng Chen, and Mark C Hersam. Solvent exfoliation of electronic-grade, two-dimensional black phosphorus. *ACS nano*, 9(4):3596–3604, 2015. [4](#), [70](#)
- [54] Gaoxue Wang, Ravindra Pandey, and Shashi P Karna. Phosphorene oxide: stability and electronic properties of a novel two-dimensional material. *Nanoscale*, 7(2):524–531, 2015. [4](#), [70](#), [71](#)
- [55] Shueh-Lin Yau, Thomas P Moffat, Allen J Bard, Zhengwei Zhang, and Michael M Lerner. Stm of the (010) surface of orthorhombic phosphorus. *Chemical physics letters*, 198(3-4):383–388, 1992. [4](#), [70](#)
- [56] Yuan Huang, Jingsi Qiao, Kai He, Stoyan Bliznakov, Eli Sutter, Xianjue Chen, Da Luo, Fanke Meng, Dong Su, Jeremy Decker, et al. Interaction of black phosphorus with oxygen and water. *Chemistry of Materials*, 2016. [4](#), [70](#)
- [57] Zenan Qi and Harold S Park. Intrinsic energy dissipation in cvd-grown graphene nanoresonators. *Nanoscale*, 4(11):3460–3465, 2012. [4](#), [8](#), [48](#), [70](#), [84](#), [87](#)
- [58] Y Zhang and YP Zhao. Detecting the mass and position of an adsorbate on a drum resonator. In *Proc. R. Soc. A*, volume 470, page 20140418. The Royal Society, 2014. [4](#), [70](#)
- [59] Jeremy T Robinson, Maxim Zalalutdinov, Jeffrey W Baldwin, Eric S Snow, Zhongqing Wei, Paul Sheehan, and Brian H Houston. Wafer-scale reduced graphene oxide films for nanomechanical devices. *Nano letters*, 8(10):3441–3445, 2008. [4](#), [70](#)
- [60] K. S. Novoselov, A. K. Geim, S. V. Morozov, D. Jiang, Y. Zhang S. V. Dubonos, I. V. Grigorieva, and A. A. Firsov. Electric field effect in atomically thin carbon films. 306(5696):666–669, 2004. [4](#), [89](#)
- [61] Claire Berger, Zhimin Song, Tianbo Li, Xuebin Li, Asmerom Y. Ogbazghi, Rui Feng, Zhenting Dai, Alexei N. Marchenkov, Edward H. Conrad, Phillip N. First, and Walt A. de Heer. Ultrathin epitaxial graphite: 2d electron gas properties and a route toward graphene-based nanoelectronics. 108(52):19912–19916, 2004. [4](#), [89](#)

REFERENCES

- [62] J. Scott Bunch, Arend M. van der Zande, Scott S. Verbridge, Ian W. Frank, David M. Tanenbaum, Jeevak M. Parpia, Harold G. Craighead, and Paul L. McEuen. Electromechanical resonators from graphene sheets. 315:490, 2007. [4](#), [89](#)
- [63] J Scott Bunch, Scott S Verbridge, Jonathan S Alden, Arend M van der Zande, Jeevak M Parpia, Harold G Craighead, and Paul L McEuen. Impermeable atomic membranes from graphene sheets. *Nano letters*, 8(8):2458–2462, 2008. [4](#), [89](#)
- [64] Changgu Lee, Xiaoding Wei, Jeffrey W. Kysar, and James Hone. Measurement of the elastic properties and intrinsic strength of monolayer graphene. 321:385, 2008. [4](#), [89](#)
- [65] Jin-Wu Jiang, Jian-Sheng Wang, and Baowen Li. Youngs modulus of graphene: a molecular dynamics study. *Physical Review B*, 80(11):113405, 2009. [4](#), [27](#), [89](#)
- [66] B. Lassagne, D. Garcia-Sanchez, A. Aguasca, and A. Bachtold. Ultrasensitive mass sensing with a nanotube electromechanical resonator. 8(11):3735–3738, 2008. [4](#), [89](#)
- [67] C. Seoáñez, F. Guinea, and A. H. Castro Neto. Dissipation in graphene and nanotube resonators. 76:125427, 2007. [4](#), [89](#)
- [68] Sung Youb Kim and Harold S Park. Multilayer friction and attachment effects on energy dissipation in graphene nanoresonators. *Applied Physics Letters*, 94(10):101918, 2009. [4](#), [8](#), [18](#), [78](#), [89](#)
- [69] Juan Atalaya, Andreas Isacsson, and Jari M Kinaret. Continuum elastic modeling of graphene resonators. *Nano letters*, 8(12):4196–4200, 2008. [4](#), [8](#), [89](#)
- [70] Sung Youb Kim and Harold S Park. The importance of edge effects on the intrinsic loss mechanisms of graphene nanoresonators. *Nano letters*, 9(3):969–974, 2009. [4](#), [8](#), [17](#), [18](#), [77](#), [89](#)
- [71] Jin-Wu Jiang, Harold S Park, and Timon Rabczuk. Enhancing the mass sensitivity of graphene nanoresonators via nonlinear oscillations: the effective strain mechanism. *Nanotechnology*, 23(47):475501, 2012. [4](#), [8](#), [47](#), [89](#)
- [72] Daniel Midtvedt, Alexander Croy, Andreas Isacsson, Zenan Qi, and Harold S Park. Fermi-pasta-ulam physics with nanomechanical graphene resonators: Intrinsic relaxation and thermalization from flexural mode coupling. *Physical review letters*, 112(14):145503, 2014. [4](#), [89](#)

REFERENCES

- [73] O Leenaerts, B Partoens, and FM Peeters. Graphene: A perfect nanoballoon. *Applied Physics Letters*, 93(19):193107, 2008. [4](#), [89](#)
- [74] Marlon Pierce and Efstratios Manousakis. Phase diagram of second layer of h 4 e adsorbed on graphite. *Physical review letters*, 81(1):156, 1998. [4](#), [89](#)
- [75] Yongkyung Kwon and David M Ceperley. 4 he adsorption on a single graphene sheet: Path-integral monte carlo study. *Physical Review B*, 85(22):224501, 2012. [4](#), [89](#)
- [76] G Derry, D Wesner, W Carlos, and DR Frankl. Selective adsorption of 3 he and 4 he on the basal plane surface of graphite. *Surface Science*, 87(2):629–642, 1979. [4](#), [89](#)
- [77] Luda Wang, Lee W Drahushuk, Lauren Cantley, Steven P Koenig, Xinghui Liu, John Pellegrino, Michael S Strano, and J Scott Bunch. Molecular valves for controlling gas phase transport made from discrete ångström-sized pores in graphene. *Nature nanotechnology*, 10(9):785–790, 2015. [4](#), [89](#)
- [78] N. Wakabayashi, H. G. Smith, and R. M. Nicklow. Lattice dynamics of hexagonal mos₂ studied by neutron scattering. 12(2):659–663, 1975. [3](#), [34](#)
- [79] T. Liang, S. R. Phillpot, and S. B. Sinnott. Parametrization of a reactive many-body potential for mo-s systems. 79(24):245110, 2009. [3](#), [22](#), [34](#)
- [80] Jin-Wu Jiang, Harold S Park, and Timon Rabczuk. Molecular dynamics simulations of single-layer molybdenum disulphide (mos₂): Stillinger-weber parametrization, mechanical properties, and thermal conductivity. 114:064307, 2013. [3](#), [33](#), [34](#), [46](#), [50](#), [52](#), [66](#)
- [81] Markus J. Buehler. Mesoscale modeling of mechanics of carbon nanotubes: Self-assembly, self-folding, and fracture. *ournal of Materials Ressearch*, 21(11):2855–2869, 2006. [3](#), [34](#), [60](#)
- [82] J.-H. Zhao, J.-W. Jiang, W.-L. Guo, and T. Rabczuk. Coarse-grained potentials of single-walled carbon nanotubes. 71:197–218, 2014. [3](#), [34](#)
- [83] X.-P. Liu, Y. Ni, and L.-H. He. A coarse-grained simulation for tensile behavior of 2d au nanocrystal superlattices. 25(47):475705, 2014. [3](#), [34](#)
- [84] Siewert J. Marrink, Alex H. de Vries, and Alan E. Mark. oarse grained model for semiquantitative lipid simulations. 108(2):750–760, 2004. [3](#), [34](#)

REFERENCES

- [85] Siewert J. Marrink, H. Jelger Risselada, Serge Yefimov, D. Peter Tieleman, and Alex H. de Vries. The martini force field: Coarse grained model for biomolecular simulations. 111(27):7812–7824, 2007. [3](#), [34](#)
- [86] Jeroen WG Wilder, Liesbeth C Venema, Andrew G Rinzler, Richard E Smalley, and Cees Dekker. Electronic structure of atomically resolved carbon nanotubes. *Nature*, 391(6662):59–62, 1998. [7](#)
- [87] Sumio Iijima et al. Helical microtubules of graphitic carbon. *nature*, 354(6348):56–58, 1991. [7](#)
- [88] Michael H Huang, Yiying Wu, Henning Feick, Ngan Tran, Eicke Weber, and Peidong Yang. Catalytic growth of zinc oxide nanowires by vapor transport. *Advanced Materials*, 13(2):113–116, 2001. [7](#)
- [89] K Jensen, Kwanpyo Kim, and A Zettl. An atomic-resolution nanomechanical mass sensor. *Nature nanotechnology*, 3(9):533–537, 2008. [7](#)
- [90] Quan Wang. Atomic transportation via carbon nanotubes. *Nano letters*, 9(1):245–249, 2008. [7](#)
- [91] Q Wang. Separation of atoms with carbon nanotubes. *Carbon*, 47(11):2754–2757, 2009. [7](#)
- [92] Nickolay V Lavrik and Panos G Datskos. Femtogram mass detection using photothermally actuated nanomechanical resonators. *Applied Physics Letters*, 82(16):2697–2699, 2003. [7](#)
- [93] KL Ekinci, YT Yang, and ML Roukes. Ultimate limits to inertial mass sensing based upon nanoelectromechanical systems. *Journal of applied physics*, 95(5):2682–2689, 2004. [7](#), [8](#)
- [94] Ashish Modi, Nikhil Koratkar, Eric Lass, Bingqing Wei, and Pulickel M Ajayan. Miniaturized gas ionization sensors using carbon nanotubes. *Nature*, 424(6945):171–174, 2003. [7](#)
- [95] B Arash, Q Wang, and N Wu. Gene detection with carbon nanotubes. *Journal of Nanotechnology in Engineering and Medicine*, 3(2):020902, 2012. [7](#), [8](#)
- [96] Behrouz Arash, Jin-Wu Jiang, and Timon Rabczuk. A review on nanomechanical resonators and their applications in sensors and molecular transportation. *Applied physics reviews*, 2(2):021301, 2015. [7](#), [12](#), [13](#)

REFERENCES

- [97] Quan Wang and Behrouz Arash. A review on applications of carbon nanotubes and graphenes as nano-resonator sensors. *Computational Materials Science*, 82:350–360, 2014. 7
- [98] Behrouz Arash, Quan Wang, and Wen Hui Duan. Detection of gas atoms via vibration of graphenes. *Physics Letters A*, 375(24):2411–2415, 2011. 8
- [99] Behrouz Arash, Quan Wang, and Vijay K Varadan. Carbon nanotube-based sensors for detection of gas atoms. *Journal of Nanotechnology in Engineering and Medicine*, 2(2):021010, 2011. 8
- [100] Julien Chaste, A Eichler, J Moser, G Ceballos, R Rurali, and A Bachtold. A nanomechanical mass sensor with yoctogram resolution. *Nature nanotechnology*, 7(5):301–304, 2012. 8
- [101] Kilho Eom, Jaemoon Yang, Jinsung Park, Gwonchan Yoon, Young Soo Sohn, Shinsuk Park, Dae Sung Yoon, Sungsoo Na, and Taeyun Kwon. Experimental and computational characterization of biological liquid crystals: A review of single-molecule bioassays. *International journal of molecular sciences*, 10(9):4009–4032, 2009. 8
- [102] Behrouz Arash and Quan Wang. Detection of gas atoms with graphene sheets. *Computational Materials Science*, 60:245–249, 2012. 8
- [103] B Arash, Q Wang, and Kim Meow Liew. Wave propagation in graphene sheets with nonlocal elastic theory via finite element formulation. *Computer Methods in Applied Mechanics and Engineering*, 223:1–9, 2012. 8
- [104] B Arash and Q Wang. Detection of gas atoms with carbon nanotubes. *Scientific reports*, 3, 2013. 8
- [105] Wen Hui Duan and Quan Wang. Water transport with a carbon nanotube pump. *ACS nano*, 4(4):2338–2344, 2010. 8
- [106] A Khosrozadeh, Q Wang, and VK Varadan. Molecular simulations on separation of atoms with carbon nanotubes in torsion. *Computational Materials Science*, 81:280–283, 2014. 8
- [107] P Bernardo, E Drioli, and G Golemme. Membrane gas separation: a review/state of the art. *Industrial & Engineering Chemistry Research*, 48(10):4638–4663, 2009. 8
- [108] Mathias Ulbricht. Advanced functional polymer membranes. *Polymer*, 47(7):2217–2262, 2006. 8

REFERENCES

- [109] Jin-Wu Jiang, Bing-Shen Wang, Harold S Park, and Timon Rabczuk. Adsorbate migration effects on continuous and discontinuous temperature-dependent transitions in the quality factors of graphene nanoresonators. *Nanotechnology*, 25(2):025501, 2013. [8](#)
- [110] Robert C Cammarata. Surface and interface stress effects in thin films. *Progress in surface science*, 46(1):1–38, 1994. [8](#)
- [111] Wuwei Liang, Min Zhou, and Fujiu Ke. Shape memory effect in cu nanowires. *Nano Letters*, 5(10):2039–2043, 2005. [8](#)
- [112] LD Landau and EM Lifshitz. Theory of elasticity, butterworthheinemann, 1986. [9](#)
- [113] Leonard Meirovitch. *Analytical methods in vibration*, volume 16. Macmillan, New York, 1967. [9](#)
- [114] Kilho Eom, Harold S Park, Dae Sung Yoon, and Taeyun Kwon. Nanomechanical resonators and their applications in biological/chemical detection: nanomechanics principles. *Physics Reports*, 503(4):115–163, 2011. [v](#), [9](#), [11](#), [14](#), [15](#)
- [115] Benoit Witkamp, Menno Poot, and Herre SJ van der Zant. Bending-mode vibration of a suspended nanotube resonator. *Nano letters*, 6(12):2904–2908, 2006. [9](#)
- [116] Vera Sazonova, Yuval Yaish, Hande Üstünel, David Roundy, Tomás A Arias, and Paul L McEuen. A tunable carbon nanotube electromechanical oscillator. *Nature*, 431(7006):284–287, 2004. [9](#), [16](#)
- [117] M Poot, B Witkamp, MA Otte, and HSJ Van der Zant. Modelling suspended carbon nanotube resonators. *physica status solidi (b)*, 244(11):4252–4256, 2007. [9](#), [16](#)
- [118] XL Feng, Rongrui He, Peidong Yang, and ML Roukes. Very high frequency silicon nanowire electromechanical resonators. *Nano Letters*, 7(7):1953–1959, 2007. [9](#)
- [119] Scott S Verbridge, Leon M Bellan, Jeevak M Parpia, and HG Craighead. Optically driven resonance of nanoscale flexural oscillators in liquid. *Nano letters*, 6(9):2109–2114, 2006. [9](#)
- [120] Arvind Raman, John Melcher, and Ryan Tung. Cantilever dynamics in atomic force microscopy. *Nano Today*, 3(1):20–27, 2008. [10](#)

REFERENCES

- [121] Bo-Yi Chen, Meng-Kao Yeh, and Nyan-Hwa Tai. Accuracy of the spring constant of atomic force microscopy cantilevers by finite element method. *Analytical chemistry*, 79(4):1333–1338, 2007. [10](#)
- [122] Ozgur Sahin, Sergei Magonov, Chanmin Su, Calvin F Quate, and Olav Solgaard. An atomic force microscope tip designed to measure time-varying nanomechanical forces. *Nature nanotechnology*, 2(8):507–514, 2007. [10](#)
- [123] Sudhir Husale, Henrik HJ Persson, and Ozgur Sahin. Dna nanomechanics allows direct digital detection of complementary dna and microrna targets. *Nature*, 462(7276):1075–1078, 2009. [10](#)
- [124] Mingdong Dong, Sudhir Husale, and Ozgur Sahin. Determination of protein structural flexibility by microsecond force spectroscopy. *Nature nanotechnology*, 4(8):514–517, 2009. [10](#)
- [125] Mike P Allen and Dominic J Tildesley. *Computer simulation of liquids*. Oxford university press, 1989. [11](#)
- [126] Daan Frenkel and Berend Smit. Understanding molecular simulation: from algorithms to applications. *Computational sciences series*, 1:1–638, 2002. [11](#)
- [127] Donald W Brenner, Olga A Shenderova, Judith A Harrison, Steven J Stuart, Boris Ni, and Susan B Sinnott. A second-generation reactive empirical bond order (rebo) potential energy expression for hydrocarbons. *Journal of Physics: Condensed Matter*, 14(4):783, 2002. [12](#), [22](#), [30](#)
- [128] CoRoAo Catlow. Point defect and electronic properties of uranium dioxide. In *Proceedings of the Royal Society of London A: Mathematical, Physical and Engineering Sciences*, volume 353, pages 533–561. The Royal Society, 1977. [12](#)
- [129] GV Lewis and CRA Catlow. Potential models for ionic oxides. *Journal of Physics C: Solid State Physics*, 18(6):1149, 1985. [12](#)
- [130] Shuichi Nos et al. A unified formulation of the constant temperature molecular dynamics methods. *J. Chem. Phys.*, 81:511–519, 1984. [12](#), [13](#)
- [131] William G Hoover. Canonical dynamics: equilibrium phase-space distributions. *Physical review A*, 31(3):1695, 1985. [12](#), [13](#)
- [132] Hans C Andersen. Molecular dynamics simulations at constant pressure and/or temperature. *The Journal of chemical physics*, 72(4):2384–2393, 1980. [12](#)

REFERENCES

- [133] Herman JC Berendsen, JPM van Postma, Wilfred F van Gunsteren, ARHJ Di-Nola, and JR Haak. Molecular dynamics with coupling to an external bath. *The Journal of chemical physics*, 81(8):3684–3690, 1984. [12](#)
- [134] Jin-Wu Jiang, Harold S Park, and Timon Rabczuk. Preserving the q-factors of zno nanoresonators via polar surface reconstruction. *Nanotechnology*, 24(40):405705, 2013. [12](#), [13](#)
- [135] K Kunal and NR Aluru. Intrinsic dissipation in a nano-mechanical resonator. *Journal of Applied Physics*, 116(9):094304, 2014. [13](#)
- [136] Hanqing Jiang, M-F Yu, B Liu, and Y Huang. Intrinsic energy loss mechanisms in a cantilevered carbon nanotube beam oscillator. *Physical Review Letters*, 93(18):185501, 2004. [13](#), [17](#), [18](#)
- [137] ST Purcell, P Vincent, C Journet, and Vu Thien Binh. Tuning of nanotube mechanical resonances by electric field pulling. *Physical Review Letters*, 89(27):276103, 2002. [13](#)
- [138] Scott S Verbridge, Rob Ilic, HG Craighead, and Jeevak M Parpia. Size and frequency dependent gas damping of nanomechanical resonators. *Applied Physics Letters*, 93(1):013101, 2008. [13](#)
- [139] K. L. Ekinici and M. L. Roukes. Nanoelectromechanical systems. 76:061101, 2005. [13](#)
- [140] KL Ekinici and ML Roukes. Nanoelectromechanical systems. *Review of scientific instruments*, 76(6):061101, 2005. [14](#)
- [141] TD Stowe, K Yasumura, TW Kenny, D Botkin, K Wago, and D Rugar. Attonewton force detection using ultrathin silicon cantilevers. *Applied Physics Letters*, 71:288–290, 1997. [14](#)
- [142] Dustin W Carr, Stephane Evoy, Lidija Sekaric, Harold G Craighead, and Jeevak M Parpia. Measurement of mechanical resonance and losses in nanometer scale silicon wires. *Applied Physics Letters*, 75(7):920–922, 1999. [14](#)
- [143] Kevin Y Yasumura, Timothy D Stowe, Eugene M Chow, Timothy Pfafman, Thomas W Kenny, Barry C Stipe, and Daniel Rugar. Quality factors in micron- and submicron-thick cantilevers. *Journal of microelectromechanical systems*, 9(1):117–125, 2000. [14](#)

REFERENCES

- [144] Stephane Evoy, Anatoli Olkhovets, L Sekaric, Jeevak M Parpia, Harold G Craighead, and DW Carr. Temperature-dependent internal friction in silicon nanoelectromechanical systems. *Applied Physics Letters*, 77(15):2397–2399, 2000. [14](#)
- [145] AN Cleland and ML Roukes. Noise processes in nanomechanical resonators. *Journal of Applied Physics*, 92(5):2758–2769, 2002. [14](#)
- [146] BH Houston, DM Photiadis, MH Marcus, JA Bucaro, Xiao Liu, and JF Vignola. Thermoelastic loss in microscale oscillators. *Applied Physics Letters*, 80(7):1300–1302, 2002. [14](#)
- [147] Ron Lifshitz and Michael L Roukes. Thermoelastic damping in micro- and nanomechanical systems. *Physical review B*, 61(8):5600, 2000. [14](#)
- [148] John A Judge, Douglas M Photiadis, Joseph F Vignola, Brian H Houston, and Jacek Jarzynski. Attachment loss of micromechanical and nanomechanical resonators in the limits of thick and thin support structures. *Journal of Applied Physics*, 101(1):013521, 2007. [14](#)
- [149] Ignacio Wilson-Rae. Intrinsic dissipation in nanomechanical resonators due to phonon tunneling. *Physical Review B*, 77(24):245418, 2008. [14](#), [15](#)
- [150] MC Cross and Ron Lifshitz. Elastic wave transmission at an abrupt junction in a thin plate with application to heat transport and vibrations in mesoscopic systems. *Physical Review B*, 64(8):085324, 2001. [14](#), [15](#)
- [151] Christopher P Green and John E Sader. Torsional frequency response of cantilever beams immersed in viscous fluids with applications to the atomic force microscope. *Journal of applied physics*, 92(10):6262–6274, 2002. [14](#)
- [152] Jinling Yang, Takahito Ono, and Masayoshi Esashi. Energy dissipation in sub-micrometer thick single-crystal silicon cantilevers. *Journal of Microelectromechanical systems*, 11(6):775–783, 2002. [14](#)
- [153] Joshua A Henry, Yu Wang, and Melissa A Hines. Controlling energy dissipation and stability of micromechanical silicon resonators with self-assembled monolayers. *Applied physics letters*, 84(10):1765–1767, 2004. [14](#)
- [154] Geng Yun and Harold S Park. A multiscale, finite deformation formulation for surface stress effects on the coupled thermomechanical behavior of nanomaterials. *Computer Methods in Applied Mechanics and Engineering*, 197(41):3337–3350, 2008. [15](#)

REFERENCES

- [155] Sotiris C Masmanidis, Rassul B Karabalin, Iwijn De Vlaminck, Gustaaf Borghs, Mark R Freeman, and Michael L Roukes. Multifunctional nanomechanical systems via tunably coupled piezoelectric actuation. *Science*, 317(5839):780–783, 2007. [16](#)
- [156] Scott S Verbridge, Daniel Finkelstein Shapiro, Harold G Craighead, and Jeevak M Parpia. Macroscopic tuning of nanomechanics: substrate bending for reversible control of frequency and quality factor of nanostring resonators. *Nano Letters*, 7(6):1728–1735, 2007. [16](#)
- [157] DR Southworth, RA Barton, SS Verbridge, B Ilic, AD Fefferman, HG Craighead, and JM Parpia. Stress and silicon nitride: A crack in the universal dissipation of glasses. *Physical review letters*, 102(22):225503, 2009. [16](#)
- [158] Scott S Verbridge, Jeevak M Parpia, Robert B Reichenbach, Leon M Bellan, and HG Craighead. High quality factor resonance at room temperature with nanostrings under high tensile stress. *Journal of Applied Physics*, 99(12):124304, 2006. [16](#)
- [159] V Cimalla, Ch Foerster, F Will, K Tonisch, K Brueckner, R Stephan, ME Hein, O Ambacher, and E Aperathitis. Pulsed mode operation of strained microelectromechanical resonators in air. *Applied physics letters*, 88(25):253501, 2006. [17](#)
- [160] Sung Youb Kim and Harold S Park. Utilizing mechanical strain to mitigate the intrinsic loss mechanisms in oscillating metal nanowires. *Physical review letters*, 101(21):215502, 2008. [17](#), [80](#)
- [161] Markus Buehler. *Atomistic modeling of materials failure*. Springer Science & Business Media, 2008. [17](#)
- [162] J Andrew McCammon and Stephen C Harvey. *Dynamics of proteins and nucleic acids*. Cambridge University Press, 1988. [17](#)
- [163] Martin Karplus, Gregory A Petsko, et al. Molecular dynamics simulations in biology. *Nature*, 347(6294):631–639, 1990. [17](#)
- [164] Wanlin Guo, Yufeng Guo, Huajian Gao, Quanshui Zheng, and Wenyu Zhong. Energy dissipation in gigahertz oscillators from multiwalled carbon nanotubes. *Physical review letters*, 91(12):125501, 2003. [17](#), [18](#)
- [165] Yang Zhao, Chi-Chiu Ma, GuanHua Chen, and Qing Jiang. Energy dissipation mechanisms in carbon nanotube oscillators. *Physical review letters*, 91(17):175504, 2003. [17](#), [18](#)

REFERENCES

- [166] Andreas K Huttel, Gary A Steele, Benoit Witkamp, Menno Poot, Leo P Kouwenhoven, and Herre SJ van der Zant. Carbon nanotubes as ultrahigh quality factor mechanical resonators. *Nano letters*, 9(7):2547–2552, 2009. [18](#)
- [167] Seung Bo Shim, June Sang Chun, Seok Won Kang, Sung Wan Cho, Sung Woon Cho, Yun Daniel Park, Pritiraj Mohanty, Nam Kim, and Jinhee Kim. Micro-mechanical resonators fabricated from lattice-matched and etch-selective GaAs/InGaP/GaAs heterostructures. *Applied Physics Letters*, 91(13):133505–133505, 2007. [18](#)
- [168] Guiti Zolfagharkhani, Alexei Gaidarzhy, Seung-Bo Shim, Robert L Badzey, and Pritiraj Mohanty. Quantum friction in nanomechanical oscillators at millikelvin temperatures. *Physical Review B*, 72(22):224101, 2005. [18](#)
- [169] Sukky Jun. Density-functional study of edge stress in graphene. *Physical Review B*, 78(7):073405, 2008. [18](#)
- [170] VB Shenoy, CD Reddy, A Ramasubramaniam, and YW Zhang. Edge-stress-induced warping of graphene sheets and nanoribbons. *Physical review letters*, 101(24):245501, 2008. [18](#)
- [171] A. K. Geim and K. S. Novoselov. The rise of graphene. 6(3):183–191, 2007. [19](#), [20](#)
- [172] A H Castro Neto and K Novoselov. New directions in science and technology: two-dimensional crystals. *Rep. Prog. Phys.*, 74(8):082501, 2011. [19](#)
- [173] Changgu Lee, Xiaoding Wei, Jeffrey W Kysar, and James Hone. Measurement of the elastic properties and intrinsic strength of monolayer graphene. *science*, 321(5887):385–388, 2008. [19](#), [27](#), [30](#), [33](#)
- [174] Zhan-Chun Tu and Zhong-Can Ou-Yang. Single-walled and multiwalled carbon nanotubes viewed as elastic tubes with the effective young's moduli dependent on layer number. 65:233407, 2002. [19](#), [31](#)
- [175] Marino Arroyo and Ted Belytschko. An atomistic-based finite deformation membrane for single layer crystalline films. 50:1941–1977, 2001. [19](#), [31](#)
- [176] Qiang Lu, Marino Arroyo, and Rui Huang. Elastic bending modulus of monolayer graphene. 42:102002, 2009. [19](#), [31](#)
- [177] Jin-Wu Jiang and Harold S Park. Negative Poisson's ratio in single-layer black phosphorus. *Nature communications*, 5, 2014. [20](#), [27](#), [28](#)

REFERENCES

- [178] Andrea C. Ferrari. Raman spectroscopy of graphene and graphite: Disorder, electron-phonon coupling, doping and nonadiabatic effects. 143:47–57, 2007. [20](#)
- [179] C. N. R. Rao, A. K. Sood, K. S. Subrahmanyam, and A. Govindaraj. Graphene: The new two-dimensional nanomaterial. *Angewandte Chemie - International Edition*, 48(42):7752–7777, 2009. [20](#)
- [180] Matthew J. Allen, Vincent C. Tung, and Richard B. Kaner. Honeycomb carbon: A review of graphene. *CHEMICAL REVIEWS*, 10(1):132–145, 2010. [20](#)
- [181] F. Bonaccorso, Z. Sun, T. Hasan, and A. C. Ferrari. Graphene photonics and optoelectronics. 4(9):611–622, 2010. [20](#)
- [182] Frank Schwierz. Graphene transistors. 5(7):487–496, 2010. [20](#)
- [183] S.Z. Butler, S.M. Hollen, L. Cao, Y. Cui, J.A. Gupta, H.R. Gutierrez, T.F. Heinz, S.S. Hong, J. Huang, A.F. Ismach, E. Johnston-Halperin, M. Kuno, V.V. Plashnitsa, R.D. Robinson, R.S. Ruoff, S. Salahuddin, J. Shan, L. Shi, M.G. Spencer, M. Terrones, W. Windl, and J.E. Goldberger. Progress, challenges, and opportunities in two-dimensional materials beyond graphene. 7(4):2898–2926, 2013. [20](#)
- [184] Xiao Huang, Zhiyuan Zeng, and Hua Zhang. Metal dichalcogenide nanosheets: preparation, properties and applications. *CHEMICAL SOCIETY REVIEWS*, 42(5):1934–1946, 2013. [20](#)
- [185] M. Xu, T. Liang, M. Shi, and H. Chen. Graphene-like two-dimensional materials. *Chemical Reviews*, 113(5):3766–3798, 2013. [20](#)
- [186] R. Saito, G. Dresselhaus, and M. S. Dresselhaus. *Physical Properties of Carbon Nanotubes*. Imperial College, London, 1998. [29](#)
- [187] José M Soler, Emilio Artacho, Julian D Gale, Alberto García, Javier Junquera, Pablo Ordejón, and Daniel Sánchez-Portal. The siesta method for ab initio order-n materials simulation. *Journal of Physics: Condensed Matter*, 14(11):2745, 2002. [29](#)
- [188] G. Kresse and J. Furthmüller. Efficient iterative schemes for ab initio total-energy calculations using a plane-wave basis set. 54:11169, 1996. [29](#)
- [189] J. Tersoff. Empirical interatomic potential for carbon, with applications to amorphous carbon. 61(25):2879–2882, 1988. [30](#)

REFERENCES

- [190] Frank H. Stillinger and Thomas A. Weber. Computer simulation of local order in condensed phases of silicon. 31(8):5262, 1985. [30](#)
- [191] F. F. Abraham and I. P. Batra. Theoretical interpretation of atomic-force-microscope images of graphite. 209(1-2):L125–L132, 1989. [30](#)
- [192] T Aizawa, R Souda, S Otani, Y Ishizawa, and C Oshima. Bond softening in monolayer graphite formed on transition-metal carbide surfaces. *Physical Review B*, 42(18):11469, 1990. [21](#), [30](#)
- [193] Fang Liu, Pingbing Ming, and Ju Li. Ab initio calculation of ideal strength and phonon instability of graphene under tension. 76:064120, 2007. [30](#)
- [194] Feng Hao, Daining Fang, and Zhiping Xu. Mechanical and thermal transport properties of graphene with defects. 99(4):041901, 2011. [30](#)
- [195] Zhonghua Ni, Hao Bua, Min Zoub, Hong Yia, Kedong Bia, and Yunfei Chen. Anisotropic mechanical properties of graphene sheets from molecular dynamics. 405(5):1301–1306, 2009. [30](#)
- [196] Jin-Wu Jiang, Jian-Sheng Wang, and Baowen Li. Elastic and nonlinear stiffness of graphene: A simple approach. *Physical Review B*, 81(7):073405, 2010. [27](#), [30](#)
- [197] C D Reddy, S Rajendran, and K M Liew. Equilibrium configuration and continuum elastic properties of finite sized graphene. 17(3):864, 2006. [30](#)
- [198] Emiliano Cadelano, Pier Luca Palla, Stefano Giordano, and Luciano Colombo. Nonlinear elasticity of monolayer graphene. *Physical review letters*, 102(23):235502, 2009. [30](#)
- [199] H. Zhao, K. Min, and N. R. Aluru. Size and chirality dependent elastic properties of graphene nanoribbons under uniaxial tension. 9(8):3012–3015, 2009. [30](#)
- [200] Z Xin, Z Jianjun, and Z-C Ou-Yang. Strain energy and young’s modulus of single-wall carbon nanotubes calculated from electronic energy-band theory. 62(20):13692–13696, 2000. [30](#)
- [201] Tinghua Ma, Bin Li, and Tienchong Chang. Chirality- and curvature-dependent bending stiffness of single layer graphene. 99:201901, 2011. [30](#)
- [202] YongKuan Shen and HengAn Wu. Interlayer shear effect on multilayer graphene subjected to bending. 100(10):101909, 2012. [30](#)

REFERENCES

- [203] Xinghua Shi, Bo Peng, Nicola M. Pugno, and Huajian Gao. Stretch-induced softening of bending rigidity in graphene. 100:191913, 2012. [30](#)
- [204] Yi Wang, Rong Yang, Zhiwen Shi, Lianchang Zhang, Dongxia Shi, Enge Wang, and Guangyu Zhang. Super-elastic graphene ripples for flexible strain sensors. *ACS nano*, 5(5):3645–3650, 2011. [23](#)
- [205] Jin-Xing Shi, Qing-Qing Ni, Xiao-Wen Lei, and Toshiaki Natsuki. Nonlocal elasticity theory for the buckling of double-layer graphene nanoribbons based on a continuum model. 50(11):3085–3090, 2011. [23](#)
- [206] Changguo Wang, Lan Lan, and Huifeng Tan. The physics of wrinkling in graphene membranes under local tension. 15(8):2764–2773, 2013. [23](#)
- [207] Yuehang Xu, Changyao Chen, Vikram V. Deshpande, Frank A. DiRenno, Alexander Gondarenko, David B. Heinz, Shuaimin Liu, Philip Kim, and James Hone. Radio frequency electrical transduction of graphene mechanical resonators. 97:243111, 2010. [24](#)
- [208] X Q He, S Kitipornchai, and K M Liew. Resonance analysis of multi-layered graphene sheets used as nanoscale resonators. 16:2086–2091, 2005. [24](#)
- [209] Yilun Liu, Zhiping Xu, and Quanshui Zheng. The interlayer shear effect on graphene multilayer resonators. 59(8):1613–1622, 2011. [24](#)
- [210] Jinbao Wang, Xiaoqiao He, S. Kitipornchai, and Hongwu Zhang. Geometrical nonlinear free vibration of multi-layered graphene sheets. 44(13):135401, 2011. [24](#)
- [211] Arend M van der Zande, Robert A Barton, Jonathan S Alden, Carlos S Ruiz-Vargas, William S Whitney, Phi HQ Pham, Jiwoong Park, Jeevak M Parpia, Harold G Craighead, and Paul L McEuen. Large-scale arrays of single-layer graphene resonators. *Nano letters*, 10(12):4869–4873, 2010. [31](#)
- [212] Changyao Chen, Sami Rosenblatt, Kirill I Bolotin, William Kalb, Philip Kim, Ioannis Kymissis, Horst L Stormer, Tony F Heinz, and James Hone. Performance of monolayer graphene nanomechanical resonators with electrical read-out. *Nature nanotechnology*, 4(12):861–867, 2009. [31](#)
- [213] Jin-Wu Jiang, Bin-Sheng Wang, Harold S Park, and Timon Rabczuk. Adsorbate migration effects on continuous and discontinuous temperature-dependent transitions in the quality factors of graphene nanoresonators. 25(2):025501, 2014. [31](#)

REFERENCES

- [214] Christin Edblom and Andreas Isacsson. Diffusion-induced dissipation and mode coupling in nanomechanical resonators. *Physical Review B*, 90(15):155425, 2014. [31](#)
- [215] A Eichler, Joel Moser, J Chaste, M Zdrojek, I Wilson-Rae, and Adrian Bachtold. Nonlinear damping in mechanical resonators made from carbon nanotubes and graphene. *Nature nanotechnology*, 6(6):339–342, 2011. [31](#)
- [216] Yan Wang, Zhiqiang Shi, Yi Huang, Yanfeng Ma, Chengyang Wang, Mingming Chen, and Yongsheng Chen. Supercapacitor devices based on graphene materials. *The Journal of Physical Chemistry C*, 113(30):13103–13107, 2009. [32](#)
- [217] KSA Novoselov, Andre K Geim, SVb Morozov, Da Jiang, Mlc Katsnelson, IVa Grigorieva, SVb Dubonos, and AAb Firsov. Two-dimensional gas of massless dirac fermions in graphene. *nature*, 438(7065):197–200, 2005. [32](#), [33](#)
- [218] S. Y. Zhou, G.-H. Gweon, J. Graf, A. V. Fedorov, C. D. Spataru, R. D. Diehl, Y. Kopelevich, D.-H. Lee, Steven G. Louie, and A. Lanzara. First direct observation of dirac fermions in graphite. *2*:595–599, 2006. [32](#)
- [219] B. Partoens and F. M. Peeters. Normal and dirac fermions in graphene multilayers: Tight-binding description of the electronic structure. *75*:193402, 2007. [32](#)
- [220] Joanna Hass, François Varchon, Jorge-Enrique Millan-Otoya, Michael Sprinkle, Nikhil Sharma, Walt A de Heer, Claire Berger, Phillip N First, Laurance Magaud, and Edawrd H Conrad. Why multilayer graphene on 4 h- sic (000 1) behaves like a single sheet of graphene. *Physical Review Letters*, 100(12):125504, 2008. [32](#)
- [221] S. Reich, J. Maultzsch, C. Thomsen, and P. Ordejon. Tight-binding description of graphene. *66*:035412, 2002. [32](#)
- [222] Vitor M. Pereira, A. H. Castro Neto, and N. M. R. Peres. Tight-binding approach to uniaxial strain in graphene. *80*:045401, 2009. [32](#)
- [223] F. Guinea, M. I. Katsnelson, and A. K. Geim. Energy gaps and a zero-field quantum hall effect in graphene by strain engineering. *6*(1):30–33, 2010. [32](#)
- [224] Kyoko Nakada, Mitsutaka Fujita, Gene Dresselhaus, and Mildred S. Dresselhaus. Edge state in graphene ribbons: Nanometer size effect and edge shape dependence. *54*:17954, 1996. [32](#)

REFERENCES

- [225] Jin-Wu Jiang, Harold S Park, and Timon Rabczuk. Molecular dynamics simulations of single-layer molybdenum disulphide (mos₂): Stillinger-weber parametrization, mechanical properties, and thermal conductivity. *Journal of Applied Physics*, 114(6):064307, 2013. ix, 20, 22, 23, 26, 27, 38
- [226] Alejandro Molina-Sanchez and Ludger Wirtz. Phonons in single-layer and few-layer mos₂ and ws₂. *Physical Review B*, 84(15):155413, 2011. 20
- [227] N Wakabayashi, HG Smith, and RM Nicklow. Lattice dynamics of hexagonal mos₂ studied by neutron scattering. *Physical Review B*, 12(2):659, 1975. ix, 20, 21, 22, 40, 41
- [228] J A Stewart and D E Spearot. Atomistic simulations of nanoindentation on the basal plane of crystalline molybdenum disulfide (mos₂). 21:045003, 2013. 22
- [229] Julian D Gale. Gulp: A computer program for the symmetry-adapted simulation of solids. *J. Chem. Soc., Faraday Trans.*, 93(4):629–637. Code available from <https://projects.ivec.org/gulp/>, 1997. 22
- [230] Lammmps. <http://www.cs.sandia.gov/~sjplimp/lammps.html>, 2012. ix, 22, 45, 46, 51, 71, 91
- [231] E. Dobardzic, I. Milosevic, B. Dakic, and M. Damnjanovic. Raman and infrared-active modes in ms₂ nanotubes (m=mo,w). 74(3):033403, 2006. 22
- [232] M. Damnjanovic, E. Dobardzic, I. Miloevic, M. Virsek, and M. Remskar. Phonons in mos₂ and ws₂ nanotubes. *Materials and Manufacturing Processes*, 23:579–582, 2008. 22
- [233] Qu Yue, Jun Kang, Zhengzheng Shao, Xueao Zhang, Shengli Chang, Guang Wang, Shiqiao Qin, and Jingbo Li. Mechanical and electronic properties of monolayer mos₂ under elastic strain. 376:1166–1170, 2012. 22
- [234] Ryan C Cooper, Changgu Lee, Chris A Marianetti, Xiaoding Wei, James Hone, and Jeffrey W Kysar. Nonlinear elastic behavior of two-dimensional molybdenum disulfide. *Physical Review B*, 87(3):035423, 2013. 23, 27, 33
- [235] Simone Bertolazzi, Jacopo Brivio, and Andras Kis. Stretching and breaking of ultrathin mos₂. *ACS nano*, 5(12):9703–9709, 2011. 23, 27, 33
- [236] Kai Liu, Qimin Yan, Michelle Chen, Wen Fan, Yinghui Sun, Joonki Suh, Deyi Fu, Sangwook Lee, Jian Zhou, Sefaattin Tongay, et al. Elastic properties of chemical-vapor-deposited monolayer mos₂, ws₂, and their bilayer heterostructures. *Nano letters*, 14(9):5097–5103, 2014. 23

REFERENCES

- [237] A Castellanos-Gomez, M Poot, G A Steele, H S J van der Zant, N Agrait, and G Rubio-Bollinger. Elastic properties of freely suspended mos₂ nano sheets. *24:772–775*, 2012. [23](#)
- [238] Peng Tao, Huaihong Guo, Teng Yang, and Zhidong Zhang. Strain-induced magnetism in mos₂ monolayer with defects. *115:054305*, 2014. [23](#)
- [239] Yung-Chang Lin, Dumitru O. Dumcenco, Ying-Sheng Huang, and Kazu Suenaga. Atomic mechanism of phase transition between metallic and semiconducting mos₂ single-layers. *9:391–396*, 2014. [23](#)
- [240] Khanh Q. Dang, Joseph P. Simpsona, and Douglas E. Spearot. Phase transformation in monolayer molybdenum disulphide (mos₂) under tension predicted by molecular dynamics simulations. *Scripta Materialia*, *76:41–44*, 2014. [23](#)
- [241] Jin-Wu Jiang, Zenan Qi, Harold S Park, and Timon Rabczuk. Elastic bending modulus of single-layer molybdenum disulfide (mos₂): finite thickness effect. *Nanotechnology*, *24(43):435705*, 2013. [23](#), [57](#)
- [242] Marino Arroyo and Ted Belytschko. Finite crystal elasticity of carbon nanotubes based on the exponential cauchy-born rule. *69:115415*, 2004. [23](#)
- [243] Jin-Wu Jiang. Phonon bandgap engineering of strained monolayer mos₂. *Nanoscale*, *6(14):8326–8333*, 2014. [31](#)
- [244] Jin Wu Jiang. The buckling of single-layer mos₂ under uniaxial compression. *Nanotechnology*, *25(35):355402*, 2014. [31](#)
- [245] Andres Castellanos-Gomez, Ronald van Leeuwen, Michele Buscema, Herre SJ van der Zant, Gary A Steele, and Warner J Venstra. Single-layer mos₂ mechanical resonators. *Advanced Materials*, *25(46):6719–6723*, 2013. [24](#)
- [246] Jaesung Lee, Zenghui Wang, Keliang He, Jie Shan, and Philip X-L Feng. High frequency mos₂ nanomechanical resonators. *ACS nano*, *7(7):6086–6091*, 2013. [24](#)
- [247] Jin-Wu Jiang, Harold S Park, and Timon Rabczuk. Mos₂ nanoresonators: intrinsically better than graphene? *Nanoscale*, *6(7):3618–3625*, 2014. [24](#), [77](#)
- [248] A. A. Balandin. Low-frequency 1/f noise in graphene devices. *8:549*, 2013. [24](#)
- [249] Y. M. Lin and P. Avouris. Strong suppression of electrical noise in bilayer graphene nanodevices. *8:2119–2125*, 2008. [24](#)

REFERENCES

- [250] A. N. Pal and A. Ghosh. Resistance noise in electrically biased bilayer graphene. 102:126805, 2009. [24](#)
- [251] S. Rumyantsev, G. Liu, W. Stillman, M. Shur, and A. A. Balandin. Electrical and noise characteristics of graphene field-effect transistors: ambient effects, noise sources and physical mechanisms. 22:395302, 2010. [24](#)
- [252] G. Liu, S. Rumyantsev, M. Shur, and A. A. Balandin. Graphene thickness-graded transistors with reduced electronic noise. 100:033103, 2012. [24](#)
- [253] Md. Z. Hossain, S. L. Roumiantsev, M. Shur, and A. A. Balandin. Reduction of $1/f$ noise in graphene after electron-beam irradiation. 102:153512, 2013. [24](#)
- [254] T Eknapakul, PDC King, M Asakawa, P Buaphet, R-H He, S-K Mo, H Takagi, KM Shen, Félix Baumberger, T Sasagawa, et al. Electronic structure of a quasi-freestanding mos2 monolayer. *Nano letters*, 14(3):1312–1316, 2014. [25](#)
- [255] Yafei Li, Zhen Zhou, Shengbai Zhang, and Zhongfang Chen. Mos2 nanoribbons: high stability and unusual electronic and magnetic properties. *Journal of the American Chemical Society*, 130(49):16739–16744, 2008. [25](#)
- [256] Peng Lu, Xiaojun Wu, Wanlin Guo, and Xiao Cheng Zeng. Strain-dependent electronic and magnetic properties of mos 2 monolayer, bilayer, nanoribbons and nanotubes. *Physical Chemistry Chemical Physics*, 14(37):13035–13040, 2012. [25](#)
- [257] Vinod K Sangwan, Heather N Arnold, Deep Jariwala, Tobin J Marks, Lincoln J Lauhon, and Mark C Hersam. Low-frequency electronic noise in single-layer mos2 transistors. *Nano letters*, 13(9):4351–4355, 2013. [25](#)
- [258] Emilio Scalise, Michel Houssa, Geoffrey Pourtois, Valery Afanasev, and Andre Stesmans. Strain-induced semiconductor to metal transition in the two-dimensional honeycomb structure of mos₂. 5(1):43–48, 2012. [25](#)
- [259] Hiram J Conley, Bin Wang, Jed I Ziegler, Richard F Haglund Jr, Sokrates T Pantelides, and Kirill I Bolotin. Bandgap engineering of strained monolayer and bilayer mos2. *Nano letters*, 13(8):3626–3630, 2013. [25](#)
- [260] Kin Fai Mak, Changgu Lee, James Hone, Jie Shan, and Tony F Heinz. Atomically thin mos 2: a new direct-gap semiconductor. *Physical Review Letters*, 105(13):136805, 2010. [25](#)
- [261] Anton Kokalj. Computer graphics and graphical user interfaces as tools in simulations of matter at the atomic scale. 28(2):155–168, 2003. [25](#)

REFERENCES

- [262] A. Brown and S. Rundqvist. Refinement of the crystal structure of black phosphorus. 19:684–685, 1965. [25](#)
- [263] Jin-Wu Jiang. Parametrization of stillingerweber potential based on valence force field model: application to single-layer mos 2 and black phosphorus. *Nanotechnology*, 26(31):315706, 2015. [21](#), [44](#), [45](#), [46](#), [71](#), [74](#), [79](#)
- [264] C Kaneta, H Katayama-Yoshida, and A Morita. Lattice dynamics of black phosphorus. *Solid State Communications*, 44(5):613–617, 1982. [21](#)
- [265] J Tersoff. New empirical model for the structural properties of silicon. *Physical review letters*, 56(6):632, 1986. [22](#)
- [266] Jerry Tersoff. New empirical approach for the structure and energy of covalent systems. *Physical Review B*, 37(12):6991, 1988. [22](#)
- [267] J Tersoff. Empirical interatomic potential for carbon, with applications to amorphous carbon. *Physical Review Letters*, 61(25):2879, 1988. [22](#)
- [268] J Tersoff. Modeling solid-state chemistry: Interatomic potentials for multicomponent systems. *Physical Review B*, 39(8):5566, 1989. [22](#)
- [269] Jin-Wu Jiang and Jian-Sheng Wang. Manipulation of heat current by the interface between graphene and white graphene. *EPL (Europhysics Letters)*, 96(1):16003, 2011. [22](#)
- [270] Jin-Wu Jiang and Jian-Sheng Wang. Theoretical study of thermal conductivity in single-walled boron nitride nanotubes. *Physical Review B*, 84(8):085439, 2011. [22](#)
- [271] Frank H Stillinger and Thomas A Weber. Computer simulation of local order in condensed phases of silicon. *Physical review B*, 31(8):5262, 1985. [22](#), [26](#)
- [272] Jin-Wu Jiang, Timon Rabczuk, and Harold S Park. A stillinger–weber potential for single-layered black phosphorus, and the importance of cross-pucker interactions for a negative poisson’s ratio and edge stress-induced bending. *Nanoscale*, 7(14):6059–6068, 2015. [22](#), [26](#), [27](#)
- [273] L Lindsay and DA Broido. Optimized tersoff and brenner empirical potential parameters for lattice dynamics and phonon thermal transport in carbon nanotubes and graphene. *Physical Review B*, 81(20):205441, 2010. [22](#)
- [274] Jingsi Qiao, Xianghua Kong, Zhi-Xin Hu, Feng Yang, and Wei Ji. High-mobility transport anisotropy and linear dichroism in few-layer black phosphorus. *Nature communications*, 5, 2014. [27](#)

REFERENCES

- [275] Jin-Wu Jiang. The third principal direction besides armchair and zigzag in single-layer black phosphorus. *Nanotechnology*, 26(36):365702, 2015. [27](#)
- [276] Jerome Harris Weiner. *Statistical mechanics of elasticity*. Courier Corporation, 2012. [27](#)
- [277] Jin-Wu Jiang, Sung Youb Kim, and Harold S Park. Auxetic nanomaterials: Recent progress and future development. *Applied Physics Reviews*, 3(4):041101, 2016. [27](#)
- [278] Mohammad Elahi, Kaveh Khaliji, Seyed Mohammad Tabatabaei, Mahdi Pourfath, and Reza Asgari. Modulation of electronic and mechanical properties of phosphorene through strain. *Physical Review B*, 91(11):115412, 2015. [28](#)
- [279] Guangzhao Qin, Qing-Bo Yan, Zhenzhen Qin, Sheng-Ying Yue, Hui-Juan Cui, Qing-Rong Zheng, and Gang Su. Corrigendum: Hinge-like structure induced unusual properties of black phosphorus and new strategies to improve the thermoelectric performance. *Scientific reports*, 6, 2016. [28](#)
- [280] Likai Li, Yijun Yu, Guo Jun Ye, Qingqin Ge, Xuedong Ou, Hua Wu, Donglai Feng, Xian Hui Chen, and Yuanbo Zhang. Black phosphorus field-effect transistors. *Nature nanotechnology*, 9(5):372–377, 2014. [29](#)
- [281] Michele Buscema, Dirk J Groenendijk, Sofya I Blanter, Gary A Steele, Herre SJ van der Zant, and Andres Castellanos-Gomez. Fast and broadband photoreponse of few-layer black phosphorus field-effect transistors. *Nano letters*, 14(6):3347–3352, 2014. [29](#)
- [282] Yanlan Du, Chuying Ouyang, Siqi Shi, and Minsheng Lei. Ab initio studies on atomic and electronic structures of black phosphorus. 107:093718, 2010. [29](#)
- [283] Andres Castellanos-Gomez, Leonardo Vicarelli, Elsa Prada, Joshua O. Island, K. L. Narasimha-Acharya, Sofya I. Blanter, Dirk J. Groenendijk, Michele Buscema, Gary A. Steele, J. V. Alvarez, Henny W. Zandbergen, J. J. Palacios, and Herre S.J. van der Zant. Isolation and characterization of few-layer black phosphorus. *Preprint at <http://arxiv.org/abs/1403.0499>*, 2014. [29](#)
- [284] Shuichi Nose. A unified formulation of the constant temperature molecular dynamics methods. 81(1):511, 1984. [47](#), [63](#), [73](#)
- [285] William G. Hoover. Canonical dynamics: Equilibrium phase-space distributions. 31(3):1695, 1985. [47](#), [63](#), [73](#)
- [286] C Seoanez, F Guinea, and AH Castro Neto. Dissipation in graphene and nanotube resonators. *Physical Review B*, 76(12):125427, 2007. [77](#)

REFERENCES

- [287] Jin-Wu Jiang. Thermal conduction in single-layer black phosphorus: highly anisotropic? 26:055701, 2015. [77](#)
- [288] Zhen Zhu and David Tománek. Semiconducting layered blue phosphorus: A computational study. *Physical review letters*, 112(17):176802, 2014. [80](#)
- [289] Jie Guan, Zhen Zhu, and David Tománek. Phase coexistence and metal-insulator transition in few-layer phosphorene: A computational study. *Physical review letters*, 113(4):046804, 2014. [80](#)
- [290] Menghao Wu, Huahua Fu, Ling Zhou, Kailun Yao, and Xiao Cheng Zeng. Nine new phosphorene polymorphs with non-honeycomb structures: A much extended family. *Nano letters*, 15(5):3557–3562, 2015. [80](#)
- [291] Andrey A Kistanov, Yongqing Cai, Kun Zhou, Sergey V Dmitriev, and Yong-Wei Zhang. The role of h₂o and o₂ molecules and phosphorus vacancies in the structure instability of phosphorene. *arXiv preprint arXiv:1610.07512*, 2016. [70](#), [71](#)
- [292] Alexandre Favron, Etienne Gaufrès, Frédéric Fossard, Anne-Laurence Phaneuf-LHeureux, Nathalie YW Tang, Pierre L Lévesque, Annick Loiseau, Richard Leonelli, Sébastien Francoeur, and Richard Martel. ck phosphorus photooxidation and quantum confinement effects in exfoliated black phosphorus. *Nature materials*, 14(8):826–832, 2015. [70](#)
- [293] Cui-Xia Wang, Chao Zhang, Jin-Wu Jiang, Harold S Park, and Timon Rabczuk. Mechanical strain effects on black phosphorus nanoresonators. *Nanoscale*, 8(2):901–905, 2016. [81](#)
- [294] Ting Hu and Jinming Dong. Geometric and electronic structures of mono- and di-vacancies in phosphorene. *Nanotechnology*, 26(6):065705, 2015. [71](#)
- [295] Angelo Ziletti, A Carvalho, David K Campbell, David F Coker, and AH Castro Neto. Oxygen defects in phosphorene. *Physical review letters*, 114(4):046801, 2015. [71](#)
- [296] Gaoxue Wang, Ravindra Pandey, and Shashi P Karna. Effects of extrinsic point defects in phosphorene: B, c, n, o, and f adatoms. *Applied Physics Letters*, 106(17):173104, 2015. [71](#)
- [297] Gaoxue Wang, William J Slough, Ravindra Pandey, and Shashi P Karna. Degradation of phosphorene in air: understanding at atomic level. *2D Materials*, 3(2):025011, 2016. [71](#)

REFERENCES

- [298] Bing Huang, Hongjun Xiang, Qiang Xu, and Su-Huai Wei. Overcoming the phase inhomogeneity in chemically functionalized graphene: the case of graphene oxides. *Physical review letters*, 110(8):085501, 2013. 71
- [299] A Stukowski. Visualization and analysis of atomistic simulation data with ovito - the open visualization tool. 18:015012, 2010. 71, 91
- [300] <http://dasher.wustl.edu/ffe/distribution/params/oplsaa.prm>, 2016. 73
- [301] William L Jorgensen, David S Maxwell, and Julian Tirado-Rives. Development and testing of the opls all-atom force field on conformational energetics and properties of organic liquids. *Journal of the American Chemical Society*, 118(45):11225–11236, 1996. 73
- [302] Joshua O Island, Gary A Steele, Herre SJ van der Zant, and Andres Castellanos-Gomez. Environmental instability of few-layer black phosphorus. *2D Materials*, 2(1):011002, 2015. 84
- [303] Zhen-Dong Sha, Qing-Xiang Pei, Ying-Yan Zhang, and Yong-Wei Zhang. Atomic vacancies significantly degrade the mechanical properties of phosphorene. *Nanotechnology*, 27(31):315704, 2016. 84
- [304] Ernst Florens Friedrich Chladni. *Entdeckungen über die Theorie des Klanges*. Zentralantiquariat der DDR, 1787. 90
- [305] Thomas D Rossing. Chladni law for vibrating plates. *American Journal of Physics*, 50(3):271–274, 1982. 90
- [306] Ning Wei, Cunjing Lv, and Zhiping Xu. Wetting of graphene oxide: A molecular dynamics study. *Langmuir*, 30(12):3572–3578, 2014. 90, 94
- [307] Jige Chen, Chunlei Wang, Ning Wei, Rongzheng Wan, and Yi Gao. 3d flexible water channel: stretchability of nanoscale water bridge. *Nanoscale*, 8(10):5676–5681, 2016. 90
- [308] D W Brenner, O A Shenderova, J A Harrison, S J Stuart, B Ni, and S B Sinnott. A second-generation reactive empirical bond order (REBO) potential energy expression for hydrocarbons. 14:783–802, 2002. 91
- [309] Kerstin Falk, Felix Sedlmeier, Laurent Joly, Roland R Netz, and Lydéric Bocquet. Molecular origin of fast water transport in carbon nanotube membranes: superlubricity versus curvature dependent friction. *Nano letters*, 10(10):4067–4073, 2010. 91

REFERENCES

- [310] Wei Xiong, Jefferson Zhe Liu, Ming Ma, Zhiping Xu, John Sheridan, and Quanshui Zheng. Strain engineering water transport in graphene nanochannels. *Physical Review E*, 84(5):056329, 2011. [91](#)
- [311] T Werder, JH Walther, RL Jaffe, T Halicioglu, and P Koumoutsakos. On the water-carbon interaction for use in molecular dynamics simulations of graphite and carbon nanotubes. *The Journal of Physical Chemistry B*, 107(6):1345–1352, 2003. [91](#)
- [312] Peter G Kusalik, Igor M Svishchev, et al. The spatial structure in liquid water. *Science(Washington)*, 265(5176):1219–1221, 1994. [91](#)
- [313] J Scott Bunch, Arend M Van Der Zande, Scott S Verbridge, Ian W Frank, David M Tanenbaum, Jeevak M Parpia, Harold G Craighead, and Paul L McEuen. Electromechanical resonators from graphene sheets. *Science*, 315(5811):490–493, 2007. [91](#)
- [314] Daniel Garcia-Sanchez, Arend M van der Zande, A San Paulo, Benjamin Lassaragne, Paul L McEuen, and Adrian Bachtold. Imaging mechanical vibrations in suspended graphene sheets. *Nano letters*, 8(5):1399–1403, 2008. [91](#)
- [315] Daniel Garcia-Sanchez, Alvaro San Paulo, María J Esplandiu, Francesc Perez-Murano, László Forró, A Aguasca, and Adrian Bachtold. Mechanical detection of carbon nanotube resonator vibrations. *Physical review letters*, 99(8):085501, 2007. [91](#)
- [316] Sony Joseph and NR Aluru. Why are carbon nanotubes fast transporters of water? *Nano letters*, 8(2):452–458, 2008. [96](#)
- [317] Alenka Luzar, David Chandler, et al. Hydrogen-bond kinetics in liquid water. *Nature*, 379(6560):55–57, 1996. [96](#)
- [318] Gerhard Hummer, Jayendran C Rasaiah, and Jerzy P Noworyta. Water conduction through the hydrophobic channel of a carbon nanotube. *Nature*, 414(6860):188–190, 2001. [96](#)
- [319] Neil Stahl and William P Jencks. Hydrogen bonding between solutes in aqueous solution. *Journal of the American Chemical Society*, 108(14):4196–4205, 1986. [96](#)
- [320] K. K. Kam and B. A. Parkinson. Detailed photocurrent spectroscopy of the semiconducting group vi transition metal dichalcogenides. 86(4):463–467, 1982. [33](#)

REFERENCES

- [321] Kin Fai Mak, Changgu Lee, James Hone, Jie Shan, and Tony F. Heinz. Atomically thin MoS₂: A new direct-gap semiconductor. 105(13):136805, 2010. [33](#)
- [322] K. S. Novoselov, A. K. Geim, S. V. Morozov, D. Jiang, M. I. Katsnelson, I. V. Grigorieva, S. V. Dubonos, and A. A. Firsov. Two-dimensional gas of massless dirac fermions in graphene. 438(7065):197–200, 2005. [33](#)
- [323] Q. H. Wang, K. Kalantar-Zadeh, A. Kis, J. N. Coleman, and M. S. Strano. Electronics and optoelectronics of two-dimensional transition metal dichalcogenides. 7(11):699–712, 2012. [33](#)
- [324] M. Chhowalla, H. S. Shin, G. Eda, L. . Li, K. P. Loh, and H. Zhang. The chemistry of two-dimensional layered transition metal dichalcogenide nanosheets. 5(4):263–275, 2013. [33](#)
- [325] B. Radisavljevic, A. Radenovic, J. Brivio, V. Giacometti, and A. Kis. Single-layer moS₂ transistors. 6:147, 2011. [33](#)
- [326] Wen Huang, Haixia Da, and Gengchiao Liang. Thermoelectric performance of mx₂ (m=mo, w; x=s, se) monolayers. 113:104304, 2013. [33](#)
- [327] Jin-Wu Jiang, Xiao-Ying Zhuang, and Timon Rabczuk. Orientation dependent thermal conductance in single-layer mos₂. 3:2209, 2013. [33](#)
- [328] V. Varshney, S. S. Patnaik, C. Muratore, A. K. Roy, A. A. Voevodin, and B. L. Farmer. Md simulations of molybdenum disulphide (mos₂): Force-field parameterization and thermal transport behavior. 48(1):101–108, 2010. [33](#)
- [329] S. Bertolazzi, J. Brivio, and A. Kis. Stretching and breaking of ultrathin mos₂. 5(12):9703–9709, 2011. [52](#)
- [330] R. C. Cooper, C. Lee, C. A. Marianetti, X. Wei, J. Hone, and J. W. Kysar. Non-linear elastic behavior of two-dimensional molybdenum disulfide. 87:035423, 2013. [52](#)
- [331] R. C. Cooper, C. Lee, C. A. Marianetti, X. Wei, J. Hone, and J. W. Kysar. Erratum: Nonlinear elastic behavior of two-dimensional molybdenum disulfide (physical review b - condensed matter and materials physics(2013) 87 (035423)). 87(7):079901, 2013. [52](#)
- [332] Andres Castellanos-Gomez, Ronald van Leeuwen, Michele Buscema, Herre S. J. van der Zant, Gary A. Steele, and Warner J. Venstra. Single-layer mos₂ mechanical resonators. 25(46):6719–6723, 2013. [34](#)

REFERENCES

- [333] Jaesung Lee, Zenghui Wang, Keliang He, Jie Shan, and Philip X.-L. Feng. High frequency mos₂ nanomechanical resonators. 7(7):6086–6091, 2013. 34
- [334] Jin-Wu Jiang, Harold S Park, and Timon Rabczuk. Mos₂ nanoresonators: Intrinsically better than graphene? 6:3618, 2013. 34
- [335] Tao Liang, Simon R Phillpot, and Susan B Sinnott. Parametrization of a reactive many-body potential for mo–s systems. *Physical Review B*, 79(24):245110, 2009. 50
- [336] Stephen P Timoshenko and JN Goodier. Theory of elasticity. *International Journal of Bulk Solids Storage in Silos*, 1(4), 2014. 57
- [337] Junhua Zhao, Jin-Wu Jiang, Lifeng Wang, Wanlin Guo, and Timon Rabczuk. Coarse-grained potentials of single-walled carbon nanotubes. *Journal of the Mechanics and Physics of Solids*, 71:197–218, 2014. 60
- [338] Jin-Wu Jiang, Jian-Sheng Wang, and Baowen Li. Youngs modulus of graphene: a molecular dynamics study. 80(11):113405, 2009. 65
- [339] Jin-Wu Jiang, Harold S Park, and Timon Rabczuk. Enhancing the mass sensitivity of graphene nanoresonators via nonlinear oscillations: the effective strain mechanism. 23:475501, 2012. 65
- [340] Claire Berger, Zhimin Song, Tianbo Li, Xuebin Li, Asmerom Y Ogbazghi, Rui Feng, Zhenting Dai, Alexei N Marchenkov, Edward H Conrad, Phillip N First, et al. Ultrathin epitaxial graphite: 2d electron gas properties and a route toward graphene-based nanoelectronics. *The Journal of Physical Chemistry B*, 108(52):19912–19916, 2004. 33
- [341] Andre K Geim and Konstantin S Novoselov. The rise of graphene. *Nature materials*, 6(3):183–191, 2007. 33
- [342] Nikolai N Klimov, Suyong Jung, Shuze Zhu, Teng Li, C Alan Wright, Santiago D Solares, David B Newell, Nikolai B Zhitenev, and Joseph A Stroscio. Electromechanical properties of graphene drumheads. *Science*, 336(6088):1557–1561, 2012. 33
- [343] Francis J Clauss. *Solid lubricants and self-lubricating solids*. Elsevier, 2012.
- [344] Qing Hua Wang, Kouros Kalantar-Zadeh, Andras Kis, Jonathan N Coleman, and Michael S Strano. Electronics and optoelectronics of two-dimensional transition metal dichalcogenides. *Nature nanotechnology*, 7(11):699–712, 2012.

REFERENCES

- [345] Manish Chhowalla, Hyeon Suk Shin, Goki Eda, Lain-Jong Li, Kian Ping Loh, and Hua Zhang. The chemistry of two-dimensional layered transition metal dichalcogenide nanosheets. *Nature chemistry*, 5(4):263–275, 2013.
- [346] Rusen Yan, Jeffrey R Simpson, Simone Bertolazzi, Jacopo Brivio, Michael Watson, Xufei Wu, Andras Kis, Tengfei Luo, Angela R Hight Walker, and Huili Grace Xing. Thermal conductivity of monolayer molybdenum disulfide obtained from temperature-dependent raman spectroscopy. *ACS nano*, 8(1):986–993, 2014.
- [347] Jin-Wu Jiang, Xiaoying Zhuang, and Timon Rabczuk. Orientation dependent thermal conductance in single-layer mos₂. *Scientific reports*, 3, 2013. [33](#)
- [348] Wen Huang, Haixia Da, and Gengchiao Liang. Thermoelectric performance of mx₂ (m= mo, w; x= s, se) monolayers. *Journal of Applied Physics*, 113(10):104304, 2013.
- [349] Vikas Varshney, Soumya S Patnaik, Chris Muratore, Ajit K Roy, Andrey A Voevodin, and Barry L Farmer. Md simulations of molybdenum disulphide (mos₂): force-field parameterization and thermal transport behavior. *Computational Materials Science*, 48(1):101–108, 2010.
- [350] Andres Castellanos-Gomez, Menno Poot, Gary A Steele, Herre SJ van der Zant, Nicolás Agrait, and Gabino Rubio-Bollinger. Elastic properties of freely suspended mos₂ nanosheets. *Advanced Materials*, 24(6):772–775, 2012. [33](#)
- [351] Markus J Buehler. Mesoscale modeling of mechanics of carbon nanotubes: self-assembly, self-folding, and fracture. *Journal of materials research*, 21(11):2855–2869, 2006.
- [352] XP Liu, Y Ni, and LH He. A coarse-grained simulation for tensile behavior of 2d au nanocrystal superlattices. *Nanotechnology*, 25(47):475704, 2014.
- [353] Cui-Xia Wang, Chao Zhang, Jin-Wu Jiang, and Timon Rabczuk. A coarse-grained simulation for the folding of molybdenum disulphide. *Journal of Physics D: Applied Physics*, 49(2):025302, 2015. [35](#), [42](#), [46](#)
- [354] Siewert J Marrink, H Jelger Risselada, Serge Yefimov, D Peter Tieleman, and Alex H De Vries. The martini force field: coarse grained model for biomolecular simulations. *The Journal of Physical Chemistry B*, 111(27):7812–7824, 2007.
- [355] Siewert J Marrink, Alex H De Vries, and Alan E Mark. Coarse grained model for semiquantitative lipid simulations. *The Journal of Physical Chemistry B*, 108(2):750–760, 2004.

Academic Curriculum Vitae

Cuixia Wang

Institute of Structural Mechanics
Bauhaus-University Weimar
Marienstrasse 15, 99423 Weimar, Germany
Email: cuixia.wang@uni-weimar.de
cuixia.wang.weimar@gmail.com

Education

- ~ Ph.D student: Institute of Structural Mechanics, Bauhaus-University Weimar, Germany, 2012- present.
- ~ M.Eng.: Structural Engineering, Northwest A&F University, China, 2008-2011
- ~ B.Eng.: Urban Planning, Northwest A&F University, China, 2004-2008

Publications

1. CX Wang, C. Zhang, JW Jiang, and T. Rabczuk. *A Coarse-Grained Simulation for the Folding of Molybdenum Disulphide*. Journal of Physics D: Applied Physics, 49 (2): 025302, 2015.
2. CX Wang, C. Zhang, JW Jiang, H. Park, and T. Rabczuk. *Mechanical Strain Effects on Black Phosphorus Nanoresonators*. Nanoscale, 8(2): 901-905, 2016.

3. CX Wang, C. Zhang, JW Jiang, N. Wei, H. Park and T. Rabczuk. *Self-Assembly of Water Molecules Using Graphene Nanoresonators*. RSC Advances, 6 (112): 110466-110470, 2016.
4. CX Wang, C. Zhang, JW Jiang, and T. Rabczuk. *The Effects of Vacancy and Oxidation on Black Phosphorus Nanoresonators*. Nanotechnology, 28 (13): 135202, 2017.
5. CX Wang, C. Zhang, and T. Rabczuk. *A Two-Dimensional Coarse-Grained Model for Molybdenum Disulphide*. (Accept by Journal of Modeling in Mechanics and Materials).